UNIVERSITÀ DEGLI STUDI DI TRIESTE
FACOLTÀ DI SCIENZE MATEMATICHE, FISICHE E NATURALI

UNIVERSITÉ DE SAVOIE

XVII CICLO DEL
DOTTORATO DI RICERCA IN FISICA

HADRONIC *B* DECAYS TO DOUBLE CHARM FINAL STATES

DOTTORANDO
SERGIO GRANCAGNOLO

COORDINATORE DEL COLLEGIO DEI DOCENTI
CHIAR.MO PROF. GAETANO SENATORE

RELATORE
CHIAR.MO DOTT. JEAN-PIERRE LEES

RELATORE
CHIAR.MO PROF. LIVIO LANCERI

Contents

Introduction

Since the beginning of the XX century particle physics achieved great progress. The theoretical picture of the behavior of nature in this field, called Standard Model of elementary particles, is very successful in describing the experimental results. In this model, the fundamental particles are quarks and leptons and the carriers of the interactions between them are called vector bosons. Several fundamental questions remain however open: the unobserved Higgs boson, necessary to explain the particles masses; the incorporation of the observed non-zero masses for neutrinos; the possible existence of supersymmetries, that predict a new "superpartner" for each known elementary particle. Future experiments like those at the Large Hadron Collider, in construction at CERN, will hopefully answer these questions, while already now current experiments may give a hint of the presence of new physics, beyond this model.

Some of the present open questions are motivated by cosmology; for instance understanding why the universe is made of matter instead of anti-matter requires a better knowledge of the discrete symmetries of nature, that turn out to be deeply connected with the so called "flavors" of fundamental fermions. Until 1964, all interaction were believed to be symmetric for the combination of charge conjugation (C) and space reflection (P), the CP transformation. Cronin & Fitch [1] discovered that CP invariance is violated in K meson decays. As a consequence, Kobayashi and Maskawa [2] suggested the existence of a third generation of quarks, discovered several years later [3] when the Υ (Upsilon) resonance was observed and interpreted as a bound state of b and $\bar{b}$ (bottom) quarks. An excitation of this $b\bar{b}$ bound state, the $\Upsilon(4S)$ is over the threshold for the production of a pair of particles containing a b or $\bar{b}$ quark, the B mesons. Each $\Upsilon(4S)$ decays to B^+B^- pair (containing up and bottom quarks) or a $B^0\bar{B}^0$ pair (containing down and bottom quarks).

Producing large samples of $\Upsilon(4S) \to B\bar{B}$ decays in electron-positron annihilations has now become a routine tool to study the dynamics of heavy quarks in B mesons and the role of discrete symmetries in their decays and mixing. A B-factory is an accelerator where electron and positron high intensity beams collide at the $\Upsilon(4S)$ energy, producing a large quantity of B meson pairs in a *coherent* initial state. The knowledge of the 4-momentum of the two B meson system and also the knowledge of the momentum magnitudes of the two B mesons individually in the center of mass frame are kinematic constraints that help considerably in suppressing backgrounds.

The first experiment running at the Cornell Electron Storage Ring (CESR) CESR B-factory was CLEO [4], where the $\Upsilon(4S)$ was produced at rest. The small phase space of the $\Upsilon(4S) \to B\bar{B}$ decay results in B mesons almost at rest in the center of mass frame. As a consequence, the vertexes of the B decays are so close to each other to be indistinguishable within the detector resolution. Now two experiments are taking data at B-factories: *BABAR* at the Stanford Linear Accelerator Center (SLAC) and Belle at KEK in Japan. The main improvements with respect to CLEO are a large increase in luminosity, and the asymmetric configuration of the two beam energies, implying that the B mesons are boosted in the laboratory, with well separated decay vertexes. This feature allow to observe time dependent CP violation effects in B decays.

The *BABAR* experiment was designed with the main goal of discovering CP violation in B meson decays. After this discovery [5], *BABAR* continues to produce important physics results, also in different areas of particle physics; in particular the production of b-quarks, at the PEP-II B-factory, is accompanied by a huge production of "off-resonance" $c\bar{c}$ quark pairs, allowing the study of charmed mesons with unprecedented statistical power.

Meson spectroscopy is usually considered as "understood" in terms of strong interactions binding quark-antiquark pairs, and is not listed among the important open questions briefly discussed above. However, experimental observations in this field can still reserve surprises: the work described in this thesis is motivated by and deals with a very recent one. An unexpected narrow $D_s\pi^0$ resonance at the mass of $2317\ \mathrm{MeV}/c^2$, labelled $D^*_{sJ}(2317)$, was observed by the *BABAR* collaboration [6], later confirmed by the CLEO experiment [7]. Subsequently also a second narrow state was observed by CLEO, *BABAR* and Belle, with mass close to $2460\ \mathrm{MeV}/c^2$ and labelled $D_{sJ}(2460)$. The observed isospin violating decays of these states stimulated many theoretical papers. The small widths, consistent with experimental resolution, and low mass values suggested exotic origins, like $D_s\pi$ atoms or DK molecules, or 4-quarks states [8, 9, 10, 11]. Other authors attempted revisions of standard ($c\bar{s}$) models, including chiral symmetry, revising the potential, etc. [12, 13, 14, 15, 16].

A study of the properties of these particles (we will use the symbol $D^{(*)+}_{sJ}$ or simply D_{sJ} to indicate both of them) is necessary to sort out the correct theoretical explanation. In this thesis we consider the exclusive D_{sJ} production in charged and neutral B decays, with several subsequent decay modes. The B decays can be used to study properties of these new particles: we aim to observe previously unseen decay chains, measure branching fractions for all channels, and determine the $D^{(*)+}_{sJ}$ spin by means of an angular analysis of decay products.

The first chapter gives an overview of the physics addressed by the *BABAR* experiment in general and related to the D_{sJ} states in particular; it introduces heavy and light quark spectroscopy, describes the experimental observation of the new resonances and illustrates the interest and excitement that followed their discovery trough the theoretical papers that appeared soon after.

The second chapter describes the PEP-II B-factory and the *BABAR* detector. Emphasis is given to the subdetectors particularly relevant for this analysis, like the Silicon Vertex Tracker for the "soft" pion identification from the decay of D^* mesons; however each part is described explaining its role in the overall event reconstruction.

The third chapter gives a detailed description of the method of data analysis and of the simulations used to understand the expected signal, the detector efficiency and the background model. The selection of the final candidates is performed in steps: after a pre–selection of B candidates, selection criteria are optimized and final selection is applied. We use the $B \to D^{(*)}_s D^{(*)}$ decays as a control sample and we reject events compatible with this kind of background. Finally we consider the contamination between different signal modes, due to imperfect reconstruction, and determine the corresponding correction factors.

The fourth chapter summarizes the branching fraction results, computed from the yields after subtracting the background, and discusses the systematic uncertainties and the angular analysis performed to extract informations on the spin of the $D_{sJ}(2460)$.

Chapter 1

Hadronic Decays of B mesons

1.1 Physics at a B-factory

The "*B*-factory" experimental facilities [17, 18] were designed and built with the main goal of discovering *CP* violation in *B* meson decays. Their large luminosity allows a broader program in heavy quarks, τ and two photon physics to be carried out.

In this chapter, after introducing a classification of *B* meson decays (Section 1.1.1), we concentrate on hadronic decays (Section 1.1.2) and in particular on those double-charm decays (Section 1.1.3) that give useful informations (Section 1.3) on the recently discovered D_{sJ} states (Section 1.2).

1.1.1 Classification of *B* decays

A possible classification of *B* decays is based on the nature of the final particles produced. *Leptonic* decays have final states which contains no hadrons but only leptons, e.g. $B^0 \to l^+l^-$ or $B^+ \to l^+\nu_l$ ($l = e, \mu, \tau$); *semi–leptonic* decays have final states with both leptons and hadrons, as $B^0 \to D^{*-}l^+\nu_l$ or $B^+ \to \pi^0 l^+\nu_l$; *hadronic* decays do not have leptons but only hadrons in the final states; *rare* decays do not happen through the dominant $b \to c$ quark transition, e.g. $B^0 \to K^{*0}\gamma$ where $b \to s$ at quark level. Processes such as $b \to s$ or $b \to d$ are called *flavor changing neutral current* (FCNC). Sample Feynman diagrams for these decays are reported in Figure 1.1- 1.4.

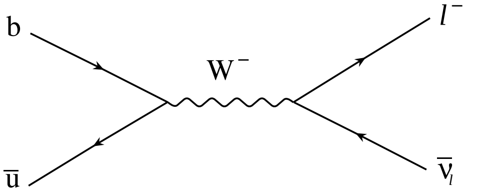

Figure 1.1: Sample Feynman diagram for leptonic $B \to l\bar{\nu}_l$ decays ($l = e, \mu, \tau$).

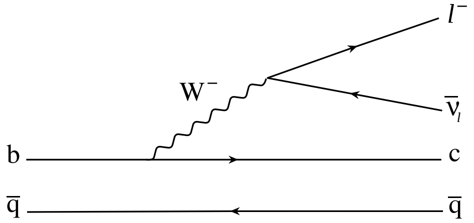

Figure 1.2: Sample Feynman diagram for semi–leptonic $B \to Dl\bar{\nu}_l$ decays ($l = e, \mu, \tau$).

The transition between qq' quarks is regulated by the Cabibbo-Kobayashi-Maskawa (CKM) matrix elements $V_{qq'}$ [2]. Looking at these matrix elements, there are transitions favored with respect to others. As an example, since $\sim |V_{ub}|^2/|V_{cb}|^2 \approx 1\%$ a decay that happen through a transition $b \to c$ is *CKM-enhanced* while a decay with $b \to u$ is *CKM-suppressed.*

If one of the two quark enters in the final state without interacting, it is called *spectator quark.* Most hadronic decays of *B* mesons can be described by external (Figure 1.5) and internal spectator decay diagrams (Figure 1.6) that can interfere. For decays with internal spectator process the

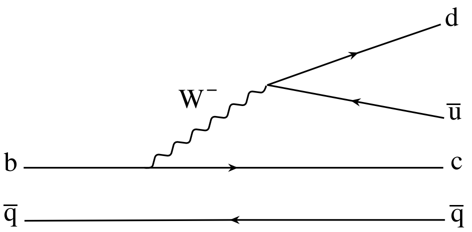

Figure 1.3: Sample Feynman diagram for hadronic transitions.

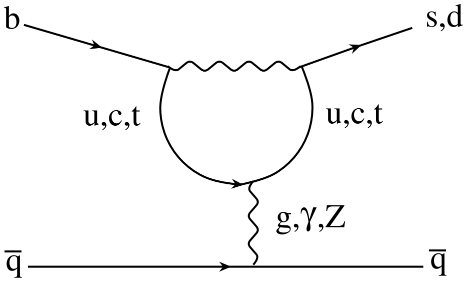

Figure 1.4: Sample Feynman "penguin" diagram for $b \to s,d$ rare FCNC transitions.

quarks from the virtual W decay must match the color of the quarks in the decaying hadron. The amplitude for this process is therefore *color suppressed*. Again, *Final State Interactions* (FSI) and non-factorisable contributions, could mask this suppression.

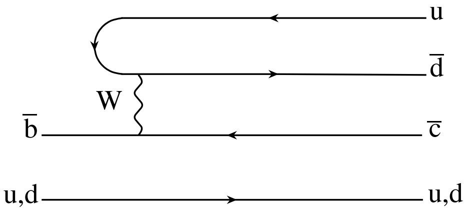

Figure 1.5: The color favored hadronic decay diagram.

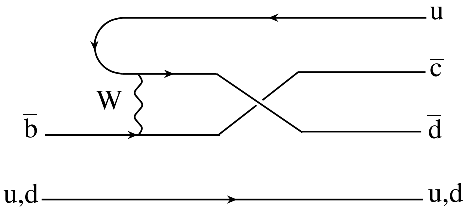

Figure 1.6: The color suppressed hadronic decay diagram.

We are interested to observe D_{sJ} particles in B decays. The $B \to D_{sJ}D^{(*)}$ decays are two–body hadronic decays and they are expected to be the largest contribution to the D_{sJ} production, since they are both CKM- and color enhanced (see Figure 1.16).

1.1.2 Hadronic B decays to open charm

The b quark in the B meson is surrounded by a cloud of light quarks and gluons. Strong interaction effects can interfere with the weak transition of the b quark: as a consequence the hadronic decays of the B are an interesting laboratory to study hadronization, perturbative and non-perturbative QCD effects and final state interaction effects (FSI).

Strong and electroweak forces are characterized by several energy scales of very different magnitude, the W mass, the various quark masses and the QCD scale: m_t, $M_W \gg m_b$, $m_c \gg \Lambda_{QCD} \gg m_u$, m_d, m_s. While it is usually sufficient to treat electroweak interactions to lowest non-vanishing order in perturbation theory, it is necessary to consider all orders in QCD. Asymptotic freedom still allows us to compute the effect of strong interactions at short distances perturbatively. However, since the participating hadrons are bound states with light quarks, confined inside the hadron by long-distance dynamics, it is clear that also non-perturbative QCD interactions enter the decay process in an essential way.

A basic tool to disentangle long- and short-distance contributions to the decay amplitudes is provided by the operator product expansion (OPE). Consider the weak decay $b \to c\bar{u}d$. We can expand the full amplitude A as follows [19]:

$$A = C\left(\frac{M_W}{\mu}, \alpha_s\right) \cdot \langle Q \rangle + O\left(\frac{p^2}{M_W^2}\right) \tag{1.1}$$

Up to a negligible power correction of $O(\frac{p^2}{M_W^2})$, the full amplitude is written as the matrix element of a local four-quark operator Q, multiplied by a *Wilson coefficient* C; μ is the energy scale, that cancels between Wilson coefficient and hadronic matrix element, to a given order in α_s, to yield a scale independent decay amplitude. This expansion in $1/M_W$ is called a (short-distance) operator product expansion because the nonlocal product of two bilinear quark-current operators ($\bar{c}b$) and ($\bar{u}d$) that interact via W exchange, is expanded into a series of local operators. In other terms OPE can be interpreted as a four-quark interaction vertex where the Wilson coefficient is the corresponding coupling constant.

The effective Hamiltonian $\mathcal{H}_{eff} = C \cdot Q$ describes the weak interactions of light quarks at low energies. Ignoring QCD interactions:

$$\mathcal{H}_{eff} = \frac{G_F}{\sqrt{2}} V_{ud}^* V_{cb} \bar{c}\gamma^\mu(1-\gamma^5) b \bar{d}\gamma_\mu(1-\gamma^5) u \tag{1.2}$$

assuming $C = 1$ and $Q = \bar{c}\gamma^\mu(1-\gamma^5) b \bar{d}\gamma_\mu(1-\gamma^5) u$. When QCD is included the quarks exchange gluons and more terms such as C and Q appear, and they receive radiative correction of order $\alpha_s^n(\mu)\ln^n(M_W/m_b)$. These corrections need to be renormalized and subtracted. The technique for performing such a re-summation is based on the *renormalization group*.

A decisive advantage of heavy hadrons is the fact that the heavy-quark mass itself is still large in comparison to Λ_{QCD}. The limit $\Lambda_{QCD}/m_b \ll 1$ (*heavy quark limit*) can then be exploited using *heavy quark expansion* (HQE) [19].

The decays which are observed involve physical hadrons, not asymptotic quark states. The computation of partial decay rates for such processes requires the analysis of hadronic matrix elements such as:

$$\langle D\pi | \bar{c}\gamma^\mu(1-\gamma^5) b \bar{u}\gamma_\mu(1-\gamma^5) d | \bar{B} \rangle \tag{1.3}$$

for the decay example $B \to D\pi$. Such matrix elements involve non-perturbative QCD and are extremely difficult to compute from first principles. However, they have no intrinsic dependence on large mass scales such as M_W. Because of this they should naturally be evaluated at a renormalization scale $\mu \ll M_W$, in which case large logarithms $\ln(M_W/m_b)$ will not arise in the matrix elements. By choosing a low scale in the effective theory, all such terms are re-summed into the Wilson coefficient functions $C_i(m_b)$.

One hypothesis that is often used is *factorization*. In factorization two-body hadronic decays can be expressed as the product of two independent hadronic currents, one describing the formation of a charm meson, and the other the hadronization of the remaining $u\bar{d}$ (or $c\bar{s}$) system from the virtual W. In other words the formation of the hadron with the charm and the spectator quarks is not influenced by the other hadron. The validity of this hypothesis needs to be tested depending on the decay mode under study.

In fact, a re-scattering can occur both at quark and at hadron level between particles produced after the weak b quark decay (FSI). FSI could modify the decay amplitudes and be important in final states such as $B \to D^* D^*$ [20].

1.1.3 The double charm decays

In Section 1.3 we will relate measurable physical quantities, such as branching ratios, to the decay constants that we define below, starting from the matrix elements.

In the Standard Model (SM) the amplitudes for $B \to D_{sJ} D^{(*)}$, are generated by the following effective Hamiltonian [21]:

$$H_{eff}^q = \frac{G_F}{\sqrt{2}} [V_{fb} V_{fq}^* (C_1 Q_{1f}^q + C_2 Q_{2f}^q) - \sum_{i=3}^{10} (V_{ub} V_{uq}^* C_i^u + V_{cb} V_{cq}^* C_i^c + V_{tb} V_{tq}^* C_i^t) Q_i^q] + H.C., \tag{1.4}$$

where the superscripts u, c, t indicate the internal quarks, f can be the u or c quark, q can be either a d or a s quark depending on whether the decay is a $\Delta S = 0$ or $\Delta S = -1$ process. The operators $Q_{1f,2f}$ are the current-current operators that represent tree level processes. Q_{3-6} are the strong gluon induced "penguin" [22] operators, and operators Q_{7-10} are due to γ and Z exchange (electroweak penguins), and "box" diagrams at loop level.

In the factorization assumption the amplitude for $B \to D_{sJ}D^{(*)}$, can be written as [21]:

$$M = M_1 + M_2 \tag{1.5}$$

To simplify we will neglect M_2 that collects the small penguin contributions, therefore:

$$M \approx M_1 = \frac{G_F}{\sqrt{2}} X_1 \langle D^*_{s0}(D_{s1})|\bar{s}\gamma_\mu(1-\gamma^5)c|0\rangle\langle D^{(*)}|\bar{c}\gamma^\mu(1-\gamma^5)b|B\rangle \tag{1.6}$$

where X_1 is a combination of CKM matrix elements and Wilson coefficients (for a computation of C_i see [23]). The currents involving the heavy b and c quarks, $J^\mu_D = \langle D|\bar{c}\gamma^\mu(1-\gamma^5)b|B(p)\rangle$ and $J^\mu_{D^*} = \langle D^*(\varepsilon_1)|\bar{c}\gamma^\mu(1-\gamma^5)b|B(p)\rangle$ can be expressed in terms of form factors. The matrix elements $\langle D^*_{s0}(P)|\bar{s}\gamma_\mu(1-\gamma^5)c|0\rangle$ and $\langle D_{s1}(P)|\bar{s}\gamma_\mu(1-\gamma^5)c|0\rangle$ are written in terms of the decay constants ($f_{D_{s0}}$, $f_{D_{s1}}$) that are defined as

$$\begin{aligned}\langle D^*_{s0}(P)|\bar{s}\gamma_\mu(1-\gamma^5)c|0\rangle &= i f_{D_{s0}} P_\mu \\ \langle D_{s1}(P,\varepsilon_2)|\bar{s}\gamma_\mu(1-\gamma^5)c|0\rangle &= M_{D_{s1}} f_{D_{s1}} \varepsilon^*_{2\mu}\end{aligned} \tag{1.7}$$

where P is the D_{sJ} momentum and ε and $M_{D_{s1}}$ are the polarization vector and the mass of the $D_{sJ}(2460)$. We will use these decay constants in Section 1.3.

1.2 The D_{sJ} discoveries

We will give now a summary of the discovery of the $D^*_{sJ}(2317)$ and $D_{sJ}(2460)$ states from the B-factories *BABAR*, Belle and CLEO (section 1.2.2) and review in section 1.2.3 the subsequent theoretical papers that try to explain the new states as ($c\bar{s}$) or more exotic states.

Before giving details about the new particles, let us introduce (section 1.2.1) some useful elements about the spectroscopy of mesons made of a heavy and a light quark, applied to the ($c\bar{s}$) case.

1.2.1 Heavy and light quark spectroscopy

In a $Q\bar{q}$ system [14], there is a large separation in energy or mass scales, since the light and heavy quark masses m_q and m_Q are related to the Quantum Chromodynamics (QCD) strong interaction scale parameter $\Lambda_{QCD} \approx 200\,\text{MeV}$ by $m_q << \Lambda_{QCD} << m_Q$. In the limit of infinitely large mass of the heavy quark Q ($m_Q \to \infty$), the heavy-quark spin s_Q and the total angular momentum j of the light quark q, are separately conserved. The quantum number j is defined as the sum $j = l + s_q$ of the orbital angular momentum l and the spin s_q of the light quark q. In this case it provides a "good" quantum number for classification. The light quark angular momentum j and the spin s_Q of the heavy quark combine to the total angular momentum $J = j + s_Q$ of the ($Q\bar{q}$) bound state. The corresponding quantum number J fixes the spin of the resulting meson. The parity P of this meson is related to the quantum number ℓ of the orbital angular momentum l by $P = (-1)^{\ell+1}$. Thus, in the heavy quark limit the heavy-light bound states ($Q\bar{q}$) may conveniently be classified in terms of J^P or, alternatively, defining $L = l$ (in the infinite heavy-quark mass limit) and $S = s_Q + s_q$

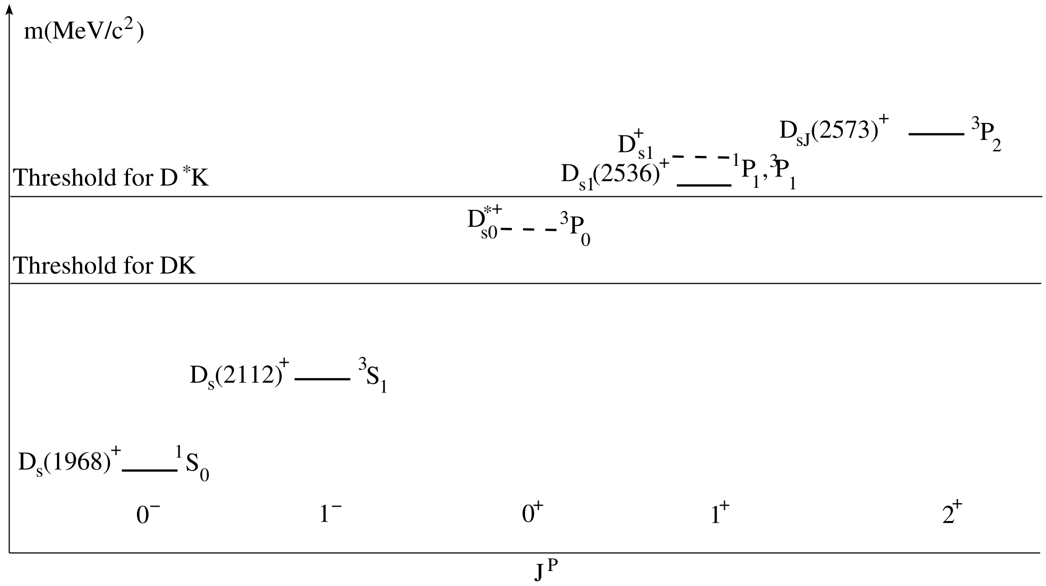

Figure 1.7: Classification of $c\bar{s}$ states, including the expected D_{sJ} states, based on theoretical models [25, 26, 27]. The spectroscopic notations J^P and $^{2S+1}L_J$ are defined in the text. Established states are indicated by solid lines. Predicted but unobserved states are indicated by dashed lines. Threshold energy for the $D^{(*)}K$ decays are also indicated.

in terms of $^{2S+1}L_J$ (see Figure 1.7).

S-wave states have orbital angular momentum $\ell = 0$ and, therefore, negative parity, $P = -1$. To obtain this parity, in this case spin and orbital angular momentum of the light quark q can couple only to $j^P = \frac{1}{2}^-$. Combining the light quark total angular momentum $j = s_q$ with the spin of the heavy quark Q yields a spin-singlet state ($^1S_0$) with spin-parity assignment $J^P = 0^-$ and a spin-triplet state ($^3S_1$) with spin-parity assignment $J^P = 1^-$.

P-wave states have orbital angular momentum $\ell = 1$ and, therefore, positive parity, $P = +1$. Spin and orbital angular momentum of the light quark can add either to $j^P = \frac{1}{2}^+$ or to $j^P = \frac{3}{2}^+$. Combination with the spin of the heavy quark yields, for $j^P = \frac{1}{2}^+$, two states with spin-parity assignment $J^P = 0^+$ ($^3P_0$) and $J^P = 1^+$, and, for $j^P = \frac{3}{2}^+$, two states with spin-parity assignment $J^P = 1^+$ and $J^P = 2^+$ ($^3P_2$). The two $J^P = 1^+$ states ($^1P_1$ and $^3P_1$) do not have definite charge-conjugation properties; therefore, they can undergo mixing. The $j^P = \frac{1}{2}^+$doublet can proceed by emitting light pseudo-scalar mesons in S-wave, while this is not the case for the $j^P = \frac{3}{2}^+$ doublet. Thus $j^P = \frac{3}{2}^+$ mesons are expected to be narrower than $j^P = \frac{1}{2}^+$ ones, simply due to the different dependence of the two-body decay rates on the three-momentum of the emitted meson.

Now, let us apply this classification in the case of the mesons formed by a $c\bar{s}$ pair: the pseudo-scalar $J^P = 0^-$ state has been identified with the isosinglet $D_s^{\pm}$ meson, with a mass of (1968.3 ± 0.5) MeV and a well established spin-parity assignment $J^P = 0^-$ [24]. The vector $J^P = 1^-$ state is assumed to be identical to the isosinglet $D_s^{*\pm}$ meson, with a mass of (2112.1 ± 0.7) MeV, natural spin-parity, and width and decay modes consistent with the assignment $J^P = 1^-$ [24].

The vector $J^P = 1^+$ state belonging to the $j^P = \frac{3}{2}^+$ doublet (with possibly small admixtures of its vector $J^P = 1^+$ counterpart belonging to the $j^P = \frac{1}{2}^+$ doublet) is in general assumed to be identical to the isosinglet $D_{s1}(2536)^{\pm}$ meson, with a mass of $(2535.35 \pm 0.34 \pm 0.5)$ MeV and a spin-parity assignment $J^P = 1^+$ that is strongly favored but still needs confirmation [24].

The spin-triplet tensor $J^P = 2^+$ state is identified with the isosinglet $D_{sJ}(2573)^{\pm}$ meson, with a mass of (2572.4 ± 1.5) MeV, natural spin-parity, and width and decay modes consistent with the assignment $J^P = 2^+$ [24].

Theoretical models typically predict masses between 2.4 and 2.6 GeV/c^2 for the remaining two states [25, 26, 27]: the scalar state $J^P = 0^+$ and the vector $J^P = 1^+$ state belonging to the $j^P = \frac{1}{2}^+$; both of which should decay by kaon emission (isospin-conserving DK and D^*K final states, respectively). They would be expected to have large widths [25, 27] and hence should be difficult to detect. In conclusion we can summarize theoretical expectations as follows:

- all four P-wave states with $L = 1$ ($^1P_1$, $^3P_0$, $^3P_1$, $^3P_2$) are massive enough that their dominant strong decays would be to the isospin conserving DK and/or D^*K final states;
- the singlet and triplet $J^P = 1^+$ states ($^1P_1$, $^3P_1$) could mix;
- in the heavy quark limit, the two states 1^+ and 2^+ with $j = \frac{3}{2}$ would be narrow while the two states 0^+ and 1^+ with $j = \frac{1}{2}$ would be broad (as in the $c\bar{q}$ system with $q = u, d$).

1.2.2 The observation of D_{sJ}

In the Spring of 2003 the *BABAR* collaboration observed an unexpected narrow state near 2.32 GeV/c^2 in the inclusive $D_s\pi^0$ invariant mass distribution [6]. The data sample analyzed corresponds to an integrated luminosity of 91 fb^{-1}, recorded both on and off the $\Upsilon(4S)$ resonance by the *BABAR* detector at the PEP-II asymmetric-energy e^+e^- storage ring. A D_s^+ meson, reconstructed in the two modes $D_s^+ \to K^+K^-\pi^+$and $D_s^+ \to K^+K^-\pi^+\pi^0$, is combined with a π^0 reconstructed from a pair of photons. The fit of the $m(D_s^+\pi^0)$ invariant mass distribution (Figure 1.8) yields 1267 ± 53 candidates in the signal Gaussian function, with mass (2316.8 ± 0.4) MeV/c^2 and width (8.6 ± 0.4) MeV/c^2 for $D_s^+ \to K^+K^-\pi^+$and 273 ± 33 candidates with mass (2317.6 ± 1.3) MeV/c^2 and width (8.8 ± 1.1) MeV/c^2 in the other D_s^+ decay mode, giving consistent results. The observed small width is consistent with the experimental resolution. The signal peak, labeled $D_{sJ}^*(2317)^+$, is not present in a simulation that includes $c\bar{c}$ events and all known charm states and decays, ruling out the possibility that it could be due to a reflection from other charmed states. The signal disappears also if the events are selected using a region outside the D_s^+ mass window or exchanging the $K^{\pm}$ and $\pi^{\pm}$ identities.

To extract the quantum numbers, the helicity angular distribution was investigated. After correcting for the efficiency, the distribution is consistent with being flat, as expected for a spin-zero particle or for a particle of higher spin that is produced unpolarized. The low mass compared to those of the $D_{s1}(2536)^+$ and $D_{sJ}(2573)^+$ favors the $J^P = 0^+$ assignment (see Figure 1.7).

No evidence of the electromagnetic decay $D_{sJ}^*(2317)^+ \to D_s^+\gamma$ was found; no signal was found in the final states $D_s^+\gamma\gamma$ and $D_s^+\pi^0\gamma$. Investigating these modes, a small peak at a mass near 2.46 GeV/c^2 was found in $D_s^+\pi^0\gamma$ (see Figure 1.9)

A more detailed study was needed at this point to exclude a kinematic reflection of the $D_{sJ}^*(2317)^+$.

The observation of this state by *BABAR* is surprising for several reasons:

- its mass is smaller than most theoretically predicted values for a $0^+c\bar{s}$ state;
- it is narrow (with intrinsic width $\Gamma < 10$ MeV);
- the decay of any $c\bar{s}$ state ($I_{c\bar{s}} = 0$) to $D_s\pi^0$ ($I_{D_s} = 0, I_{\pi^0} = 1$) violates isospin conservation.

Isospin symmetry is respected in good approximation in the limit that the masses of the u and d quarks are equal. The two quarks have not exactly the same masses and isospin violation is already observed in the decay $D_s^* \to D_s\pi^0$ [28]. Similarly, since the $D_{sJ}^*(2317)^+$ mass is below

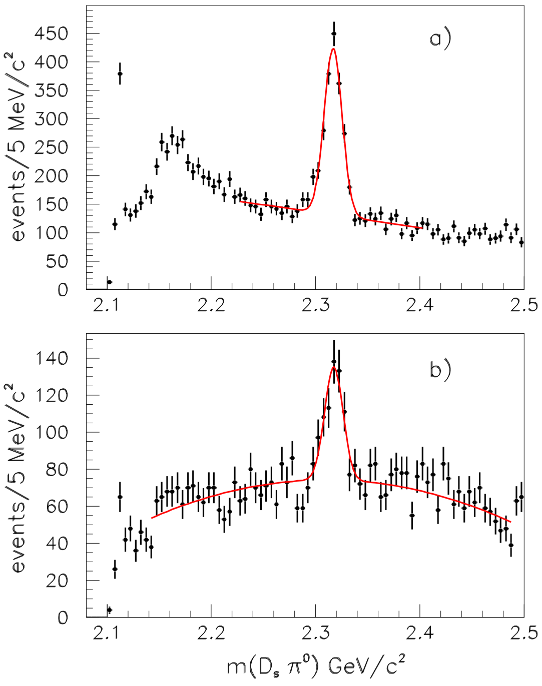

Figure 1.8: $m(D_s^+\pi^0)$ invariant mass distribution. D_s^+ candidates are reconstructed in the $D_s^+ \to K^+K^-\pi^+$(top) and $D_s^+ \to K^+K^-\pi^+\pi^0$(bottom) decay modes. The very narrow peak at $m(D_s^+\pi^0) \approx 2.1\,\mathrm{GeV}/c^2$ is associated to the $D_s^* \to D_s^+\pi^0$ decay.

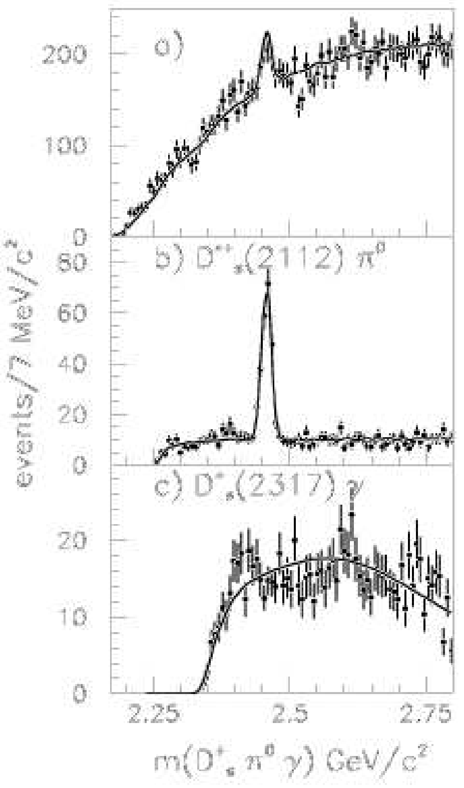

Figure 1.9: The $m(D_s^+\pi^0\gamma)$ invariant mass distribution from BABAR experiment (a). The other two plots are produced applying weights corresponding to the decay $D_s^*\pi^0$ (b) and the decay $D_{sJ}^*(2317)\gamma$ (c).

the kinematical threshold of 2.367 GeV for the isospin-conserving strong decay to DK ($I_D = \frac{1}{2}$, $I_K = \frac{1}{2}$), it is possible that the decay to $D_s\pi^0$ proceeds via $\eta - \pi^0$ mixing.

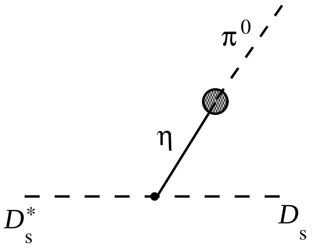

Figure 1.10: The isospin violating $D_s^* \to D_s^+\pi^0$ process could proceed via virtual η emission [28].

The transition with neutral pion emission proceeds at tree level via virtual η emission (Figure 1.10). The intermediate η converts into a π^0 through the mixing term in the Lagrangian [28]:

$$\mathcal{L}_{mixing} \propto \frac{(m_d - m_u)}{\sqrt{3}}\pi^0\eta$$

that vanishes in the limit of equal up and down quark masses m_d and m_u. In the case of D_s^*, the $D_s^* \to D_s\gamma$ process dominates over this isospin violating transition. In the case of $D_{sJ}^*(2317)$, the decay to $D_s\gamma$ is excluded if $J^P = 0^+$, to conserve angular momentum. The absence of the signal in this final state may support this hypothesis or simply indicate that the pion emission is favored over radiative decay. Further measurements are needed at this point.

Soon after the *BABAR* announcement, the CLEO collaboration provided independent evidence of the discovery [7], searching for the $D_{sJ}^*(2317)$ in 13.5 fb^{-1} of data collected with the CLEO-II detector in symmetric e^+e^- collisions at the Cornell Electron Storage Ring (CESR). They observed also the peak at 2.46 GeV/c^2, in the $D_s^*\pi^0$ invariant mass distribution, and they analyzed the cross–feed between $D_s\pi^0$ and $D_s^*\pi^0$ samples. The kinematics of these decays are quite similar, and they can *reflect* into one another. For example, by ignoring the photon from the D_s^* decay in $D_{sJ}(2460)^+ \to D_s^{*+}\pi^0$ decays, nearly all the signal combinations form a peak in the $D_s\pi^0$ invariant mass spectrum in the same region as the $D_{sJ}^*(2317)$ signal, but from simulation results the peak will be broader. Vice-versa, a random photon such that the $D_s\gamma$ combination accidentally falls in the D_s^* signal region, combined with a $D_s\pi^0$ candidate would reflect into the $D_{sJ}(2460)^+ \to D_s^{*+}\pi^0$ signal region. For this possibility *BABAR* did not claim immediately the discovery of both the resonances (anyway the observation is claimed soon after [29]).

From a simulation of the "reflection mechanism" a broader peak would be expected, relative to the real $D_{sJ}(2460)$ and only for approximately 9% of the reconstructed decays. Taking in account this contamination, CLEO still had evidence of 41 ± 12 decays $D_s^*\pi^0$, demonstrating the existence of a state at 2.46 GeV/c^2, called $D_{sJ}(2463)^+$. We will use the current notation from Particle Data Group [24] $D_{sJ}(2460)$ in the following.

If this is a $c\bar{s}$ state, the mass is 47.6 MeV below the kinematical threshold of 2.508 GeV/c^2 for its isospin-conserving decay D^*K and its decay to DK is forbidden by parity and angular momentum conservation. The width smaller than 7 MeV at 90% confidence level, is consistent with predictions from simulation in which the state is modeled with a negligible natural width.

CLEO investigated other final states and set upper limits for other decay modes such $D_s^+\gamma$, $D_s^{*+}\gamma$, $D_s^+\ \pi^+\ \pi^-$ and $D_{sJ}^*(2317)^+\gamma$. A diagram containing both the new particles, the $D^{(*)0}K$ threshold and the already known $c\bar{s}$ mesons is shown in Figure 1.11.

The Belle Collaboration investigated the properties of the D_{sJ} resonances as well. They used a 86.9 fb^{-1} data sample collected with the Belle detector at KEKB [30]. They determined the masses m($D_{sJ}^*(2317)$) and m($D_{sJ}(2460)$) (see Table 1.1) and for the last one, they also observe the decays $D_{sJ}(2460)^+ \to D_s^+\gamma$ and $D_{sJ}(2460)^+ \to D_s^+\pi\pi$. The spin-parity assignments are consistent with $J^P = 0^+$ for the $D_{sJ}^*(2317)$ and $J^P = 1^+$ for the $D_{sJ}(2460)$. The most recent results on yields of the D_{sJ} from the B-factories experiments are reported in Table 1.2. The transitions seen (or not seen) in the data are shown with a solid arrow (dashed line) in the diagrams of Figure 1.12 and 1.13 for the D_{sJ} decay with an emission of a γ or of a π^0, respectively.

Table 1.1: Masses and widths for the new D_{sJ} states from BaBar, CLEO and Belle.

	$D_{sJ}^*(2317)$		$D_{sJ}(2460)$	
Experiment	mass (MeV/c^2)	width (MeV/c^2)	mass (MeV/c^2)	width (MeV/c^2)
BABAR [35]	$2318.9 \pm 0.3 \pm 0.9$	< 10	$2459.4 \pm 0.3 \pm 1.0$	< 10
CLEO [7]	$2318.3 \pm 1.2 \pm 1.0$	< 7	$2463.3 \pm 1.7 \pm 1.0$	< 7
Belle [30]	$2317.2 \pm 0.5 \pm 0.9$	< 4.6	$2456.5 \pm 1.3 \pm 1.3$	< 5.5

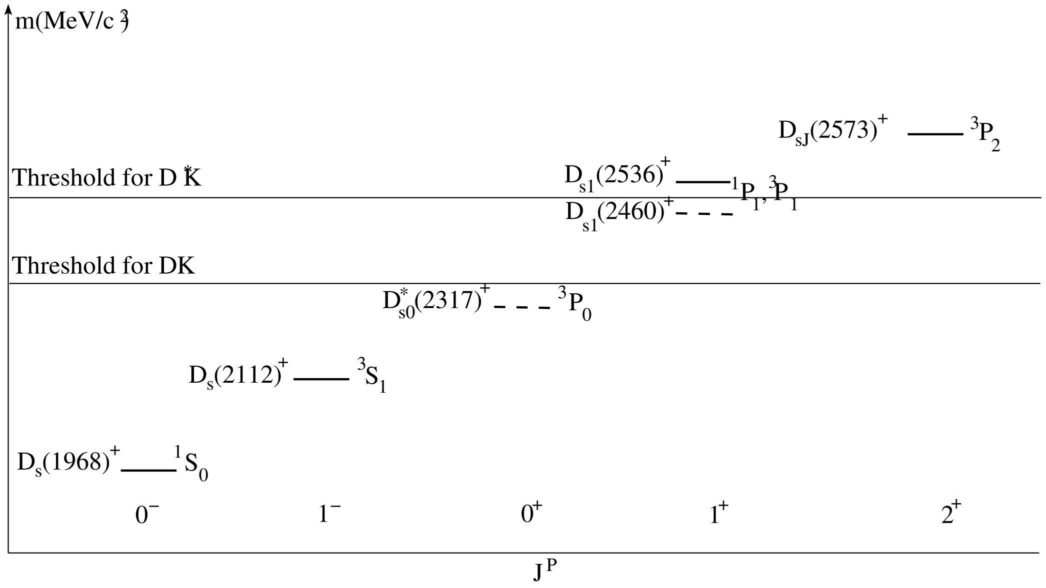

Figure 1.11: Classification of $c\bar{s}$ states, including the newly discovered $D^*_{sJ}(2317)$ and $D_{sJ}(2460)$ states (dashed lines), with their presumed quantum numbers. Established states are indicated by solid lines.

Table 1.2: Event yields for the new D_{sJ} states from BABAR, CLEO and Belle. When present, errors are statistical and systematic (in that order) otherwise only statistical error is reported.

	Event Yields		
Decay	*BABAR* [35]	CLEO [7]	Belle [30]
$D^*_{sJ}(2317)$ $[D_s\pi^0]$	1275 ± 45	135 ± 23	$761 \pm 44 \pm 30$
$D^*_{sJ}(2317)$ $[D_s\gamma]$	Not Seen	Not Seen	Not Seen
$D^*_{sJ}(2317)$ $[D^*_s\gamma]$		Not Seen	Not Seen
$D^*_{sJ}(2317)$ $[D_s\pi^+\pi^-]$	Not Seen	Not Seen	Not Seen
$D^*_{sJ}(2317)$ $[D^*_s\pi^0]$		Not Seen	
$D_{sJ}(2460)$ $[D^*_s\pi^0]$	266 ± 38	41 ± 12	$126 \pm 25 \pm 12$
$D_{sJ}(2460)$ $[D_s\gamma]$	509 ± 46	Hint	152 ± 18
$D_{sJ}(2460)$ $[D^*_s\gamma]$		Not Seen	Not Seen
$D_{sJ}(2460)$ $[D^*_{sJ}(2317)\gamma]$	Not Seen	Not Seen	
$D_{sJ}(2460)$ $[D_s\pi^+\pi^-]$	67 ± 11	Not Seen	59.7 ± 11.5
$D_{sJ}(2460)$ $[D_s\pi^0]$	Not Seen		Not Seen
Luminosity	125 fb^{-1}	13.5 fb^{-1}	86.9 fb^{-1}

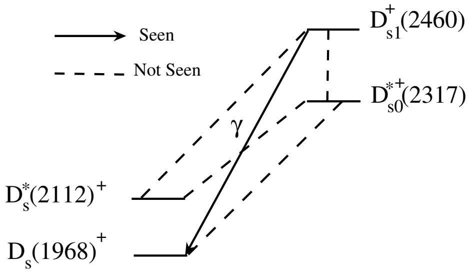

Figure 1.12: $D_{sJ} \to D^{(*)}_s\gamma$ transitions. Transitions already seen (not seen) are indicated with a solid (dashed) line.

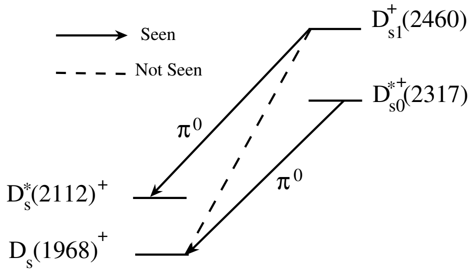

Figure 1.13: $D_{sJ} \to D^{(*)}_s\pi^0$ transitions. Transitions already seen (not seen) are indicated with a solid (dashed) line.

1.2.3 Theoretical explanations for the new states

After the discoveries described in the previous section, several theoretical papers appeared proposing explanations for the new resonances. Explanations, non-exotic and exotic, are summarized in the following. In non-exotic explanations the new particles are interpreted as $c\bar{s}$ resonances with some additional hypotheses to justify their characteristics.

- Simple potential models do not reproduce exactly the full $c\bar{s}$ mass spectra. As an example ref. [14] uses the sum of a Coulomb and a linear potential, or ref. [13] uses a potential composed of a vector part of coulombian type and a spherical part not forced to be linear. The mass of the 0^+ and 1^+ $c\bar{s}$ states are always predicted above the $D^{(*)}K$ threshold and they are expected to decay through isospin conserving modes, with a broad width, contrary to the experimental findings.

- using the QCD sum rules with the heavy quark limit, the masses of P-wave $(c\bar{s})$ states are computed in [31, 15]. The value obtained, $m_{D^*_{s0}} = 2.42 \pm 0.13\,\mathrm{GeV}$ is 100 MeV higher than the experimental for $D^*_{sJ}(2317)$ but has large uncertainties. The low mass of $D^*_{sJ}(2317)$ and $D_{sJ}(2460)$ could be explained by the repulsion between $D_s(0^+)$, $D_s(1^+)$ and DK, DK^* continuum. The computed widths $\Gamma(D_{s0} \rightarrow D_s^+\pi^0) \simeq 6\,\mathrm{keV}$ and $\Gamma(D_{s0} \rightarrow D_s^*\gamma) \simeq 1\,\mathrm{keV}$, indicate [32] that, for D_{s0}, the electromagnetic decay, not yet observed in data, is suppressed with respect to the isospin violating one (Figure 1.14). Another effect should be visible in the $(b\bar{s})$ spectrum producing narrow peaks in $B_s\pi^0$ and $B_s^*\pi^0$ mass distributions, that are not accessible at the B-factories, but could be observed at hadron colliders, that produce also B_s mesons.

- if a coupling with the OZI-allowed DK decay is included (Figure 1.15), a scalar meson is predicted with mass 2.28 GeV/c^2. Conventional $(c\bar{s})$ state is found with a mass of 2.79 GeV/c^2 and width of 200 MeV/c^2 [33], not observed in data.

- the new particles are interpreted as an heavy $J^P(0^+, 1^+)$ spin multiplet [12]. They could be the chiral partners of the $(0^-, 1^-)$ groundstate, degenerate in principle, where the spontaneous breaking of chiral symmetry elevates the first by an amount ΔM. Taking the mass difference between the *BABAR* states and the light charm-strange mesons $D_s^{(*)}$, the observed value $\Delta M = 349\,\mathrm{MeV}$ is close to what expected by the Goldberger-Treiman relation, implied by chiral invariance. If this picture turns ot to be valid, the mass splitting for all heavy-quark chiral multiplets can be established and predictions can be done for B_s and strange doubly-heavy baryon states.

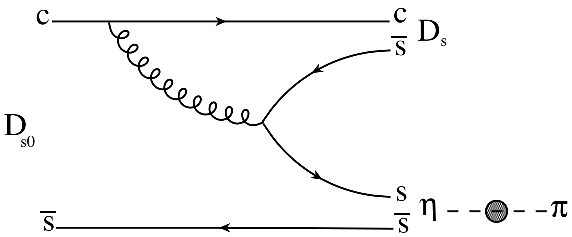

Figure 1.14: The diagram for the $D^*_{sJ}(2317) \rightarrow D_s^+\pi^0$ decay. Isospin violation is in the $\eta - \pi$ transition.

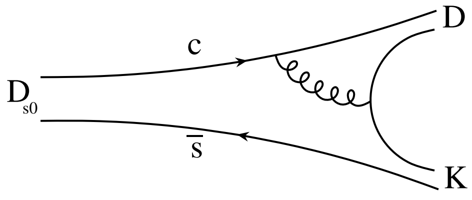

Figure 1.15: The OZI-allowed diagram $D^*_{sJ}(2317) \rightarrow DK$, that should be dominant if $m_{D_{s0}} > m_K + m_D = 2366.9\,\mathrm{MeV}$.

It has been argued [34] that lattice QCD predictions seem to be inconsistent with the simple $q\bar{q}$ interpretation for $D^*_{sJ}(2317)$, requiring exotic explanations. In this case the two missing $D^*_s(0^+)$

and $D_s(1^+)$ states are considered as not yet observed, and probably broad, while the new observed states are assumed to be of different nature with respect to $c\bar{s}$ resonances. The 4-quark states are states with additional valence quarks as $cq\bar{s}\bar{q}$. They can be divided into pure four quark states (baryonia) and hadronic "molecules" where the two "atoms" maintain their integrity.

- *DK* "molecule" [8]: a "molecule" is viewed as a 4-q state where $q\bar{q}$ meson pairs are weakly bound. Characteristics of such a state are compatible with the $D^*_{sJ}(2317)$ property of $J^P = 0^+$, and a binding energy of $\approx 40\,\text{MeV}$. A 4-q signature could be given if the elastic form factor deviate from the $1/Q^2$ expected for a $c\bar{s}$ state. Other effects proposed for experimental test are the $D^*_{sJ}(2317)$ transition to $D^*_s\gamma$, expected to have 2 keV partial width in the $c\bar{s}$ case, and the prediction of a *BD* molecule with a $B^+_c\pi$ decay.

- 4-quark: in this interpretation the $D^*_{sJ}(2317)$ is identified as the isosinglet of an isospin multiplet with quark content $[cq\bar{q}\bar{s}]^+$ (where $q\bar{q}$ is a combination of u and d quarks). The expected width is smaller than 1 MeV [9]. The remaining isostates should be instead very broad but could open double charged $D^+_s\pi^+$ (not seen [35]) and wrong pairing D^+K^- channels. B decays are proposed as a good environment to search such states with lower background. In an other 4-q interpretation [36] these isostates are instead narrow ($\sim 8.8\,\text{MeV}$ as the *BABAR* state).

- 4-quark $\Leftrightarrow$ $q\bar{q}$ oscillation [11]: the observed resonances are interpreted primarily as D_{sJ} states, mixing due to strong interaction, with broad 4-q states that lie above the $D^{(*)}K$ threshold. The parameters introduced are the mixing angle and the 4-q mass. Radiative transitions could indicate the nature of these states depending on the mixing angle. Other doubly charged $D^+_s\pi^+$ or $D^+_s\pi^-$ states are not expected to be narrow.

- $D_s\pi$ atom [10]: a strong flavor-singlet attraction could allow the capture of a pion by a charmed meson. With this hypothesis it is possible to reproduce a narrow resonance in the $D_s\pi$ spectrum corresponding to a mass of 2.32 GeV and width of 10 MeV corresponding to the *BABAR* experimental resolution. Such state should be present in other charged modes, e.g. $D^+_s\pi^\pm$, not seen [35].

Several more exotic explanations are also possible, but before looking for more complicated answers on the nature of these particles, the conventional explanations should be rejected.

Some of the predictions of these models are not accessible at the present B-factories, since they refer to the decays of B_s or B_c mesons. However, other predictions can be tested by looking at two body B decays, as $B \to D_{sJ}D^{(*)}$, as explained in the next section.

1.3 The $B \to D_{sJ}D^{(*)}$ decays

Two-body hadronic B decays are the ideal environment to study the new D_{sJ} states: in particular their quantum numbers can be extracted by an angular analysis. To produce a D_{sJ}, two-body hadronic B decay could proceed through a tree diagram via external W-emission diagram (see Figure 1.16).

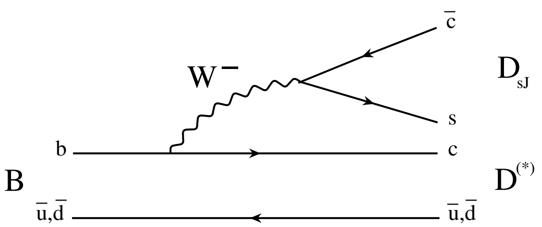

Figure 1.16: The tree diagram via external W-emission for $B \to D_{sJ}D^{(*)}$.

The modes $B \to D_{sJ}^{(*)+}M$, with $M = D, \pi, K$, can discriminate between quark-antiquark and multiquark interpretations of the $D_{sJ}^{(*)+}$ state. In the $q\bar{q}$ case the $B \to D_{sJ}^{(*)+}M$ branching ratios are expected to be of the same order of magnitude as the $B \to D_s^{(*)}M$ ones, since the $D_{sJ}^{(*)+}$ meson decay constants are expected to be close to those of low-lying $D_s^{(*)}$ mesons. In the multiquark case the branching fractions would be suppressed by inverse powers of heavy meson masses [37]. We start using decays with $M = D$ that are expected to be the dominant exclusive D_{sJ} production mechanism in B decays, because the $b \to c$ transition is CKM-favored with respect to $b \to u, d, s$.

We can therefore define the ratios of branching fractions:

$$R_{D0} = \frac{\mathcal{B}(B \to DD_{s0})}{\mathcal{B}(B \to DD_s)}$$

$$R_{D^*0} = \frac{\mathcal{B}(B \to D^*D_{s0})}{\mathcal{B}(B \to D^*D_s)} \tag{1.8}$$

and similarly for D_{s1}:

$$R_{D1} = \frac{\mathcal{B}(B \to DD_{s1})}{\mathcal{B}(B \to DD_s)}$$

$$R_{D^*1} = \frac{\mathcal{B}(B \to D^*D_{s1})}{\mathcal{B}(B \to D^*D_s^*)} \tag{1.9}$$

Within factorization and the heavy quark limit assumption, neglecting phase space and other effects that are subleading in the heavy quark expansion, they can be re-written in terms of the decay constants [21]:

$$R_{D0} = |\frac{f_{D_{s0}}}{f_{D_s}}|^2 \tag{1.10}$$

$$R_{D1} = |\frac{f_{D_{s1}}}{f_{D_s^*}}|^2 \tag{1.11}$$

defined from the transition-matrix elements in Section 1.1.2. In the heavy quark limit $f_{D_{s0}} = f_{D_{s1}}$ and $f_{D_s} = f_{D_s}^*$ and one would predict $R_{D0} \approx R_{D1}$ if all these assumptions are valid. Estimates of $f_{D_{s0}}$ are available from quark models and QCD sum rule calculations [38, 39] and typically find the p-wave states to have similar decay constants as the ground state mesons. Therefore, if $f_{D_{s0}} \sim f_{D_s}$ one expects

$$R_{D0} \approx R_{D1} \approx 1. \tag{1.12}$$

Comparison of these predictions with the experimental results by Belle [40] and by *BABAR* (this thesis) will be presented in section 4.6.

It is also interesting that three-body B decay to DDK final states could be used to test the molecular nature of the D_{sJ} [21]. Qualitatively, the nonleptonic decay $B \to DD_{sJ}^*(2317)$ could proceed through two stages: the decay $B \to DDK$, followed by the state DK forming the molecule $D_{sJ}^*(2317)$ with some probability. The measurements of the ratios of two-body and three-body B decay branching ratios could allow to find evidence for the formation of "molecules" in the $D^{(*)}K$ state.

Chapter 2

The *BABAR* Detector at SLAC

2.1 The PEP-II *B*-factory

The main physics motivations for PEP-II [17] are an exhaustive study of CP violation, using the rich spectrum of B meson decays, and a broad program of bottom quark, charm quark, τ, and two-photon physics. This program requires a machine that produces in excess of 10^7 neutral B mesons per year. The PEP-II facility consists of two independent storage rings (Fig. 2.1), one located atop the other in the 2.2 km tunnel: the high-energy ring (HER), that stores a 9 GeV electron beam, and the low-energy ring (LER), that stores 3.1 GeV positrons. The injection system with the 3 km long linear accelerator is displayed in Fig. 2.2. The design luminosity of 3×10^{33} $cm^{-2}s^{-1}$ is based on high circulating currents (approximately 1-2 A), stored in each ring, separated into more than 1600 bunches. The design luminosity was reached in October 2000 while the last best results (July 2004) are a luminosity of $9.213 \times 10^{33} cm^{-2} sec^{-1}$ and currents of 1.5 A for HER and 2.4 A for LER. The beams collide at a center of mass energy ($E_{c.m.}$) of 10.58 GeV. In Fig. 2.3 the first three resonances are the lowest-lying S states of a bound $b\overline{b}$ quark system. The narrowness of the resonances reflects their stability against strong decays; the states have insufficient energy to decompose into a pair of mesons, each carrying a b quark. The fourth state, $\Upsilon(4S)$, has just sufficient energy ($E_{\Upsilon(4S)} = 10.58$ GeV) to decay to a pair of B mesons (B^0 and $\bar{B}^0$ or B^+ and B^-); these channels totally dominate the decay of the $\Upsilon(4S)$. For this reason PEP-II is operated at the $\Upsilon(4S)$ $b\overline{b}$ resonance for a large fraction of the time. About 10% of the data is taken at a center of mass (c.m.) energy 40 MeV below the $\Upsilon(4S)$ peak, to measure hadronic backgrounds

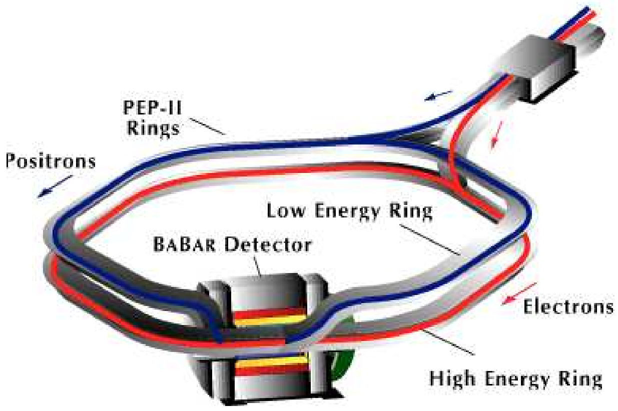

Figure 2.1: The PEP-II storage rings.

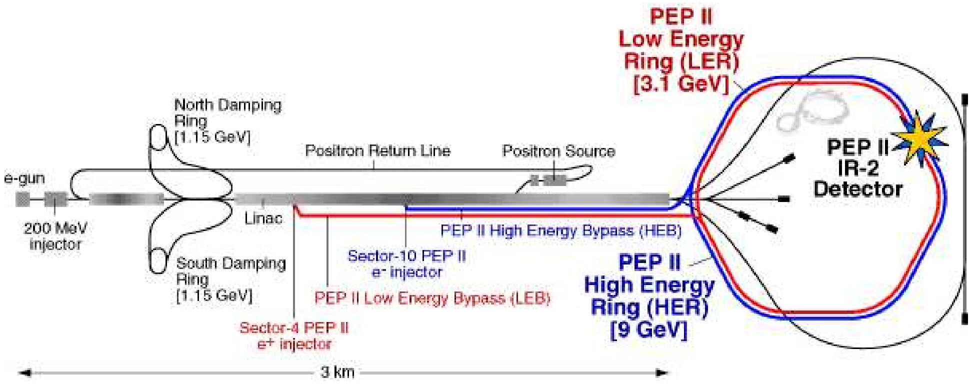

Figure 2.2: The injection system and PEP-II.

from the continuum production of lighter quark pairs (u, d, s, c). The asymmetric beam energies

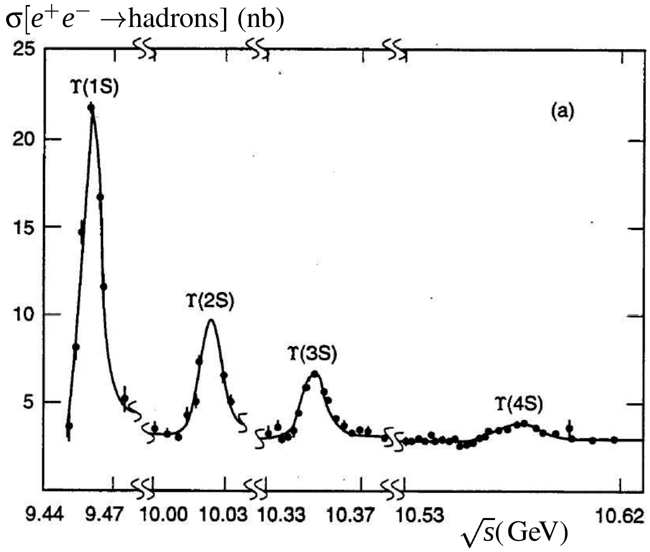

Figure 2.3: The hadronic cross section in e^+e^- collisions in the center-of-mass energy region near 10 GeV. The resonances form the Υ family interpreted as radial excitation of a bound $b\bar{b}$ quark pair. The data are from the CUSB detector group [41].

configuration boosts the $\Upsilon(4S)$ in the laboratory frame ($\beta\gamma = 0.56$). The $\beta\gamma$ boost factor was chosen optimizing the sensitivity of the measurement of CP-violating asymmetries in the decays of the B mesons [42].

2.2 The detector

The *BABAR* detector was designed and built by a large international team of scientists and engineers. It consists of a silicon vertex tracker, a drift chamber, a ring-imaging Cherenkov detector, and a CsI calorimeter [43]. These detector systems are surrounded by a superconducting solenoid that is designed for a field of 1.5 T. The steel flux return is instrumented for muon and neutral hadron detection. The detector surrounds the PEP-II interaction region. To maximize the geometric acceptance for the boosted $\Upsilon(4S)$ decays, the whole detector is offset relative to the beam-beam interaction point (IP) by 0.37 m in the direction of the lower energy beam. Fig. 2.4 shows a longitudinal section through the detector center. The detector is of compact design, its transverse dimension being constrained by the 3.5 m elevation of the beam above the floor. The solenoid radius was chosen by balancing the physics requirements and performance of the drift chamber and calorimeter against the total detector cost. As in many similar systems, the calorimeter was the most expensive single subdetector and thus considerable effort was made to minimize its total volume without undue impact on the performance of either the tracking system or the calorimeter itself. The forward and backward acceptance of the tracking system are constrained by components of PEP-II, a pair of dipole magnets (B1) followed by a pair of quadrupole magnets (Q1). The vertex detector and these magnets are placed inside a support tube (4.5 m long and 0.217 m inner diameter). The central section of this tube is fabricated from a carbon-fiber composite.

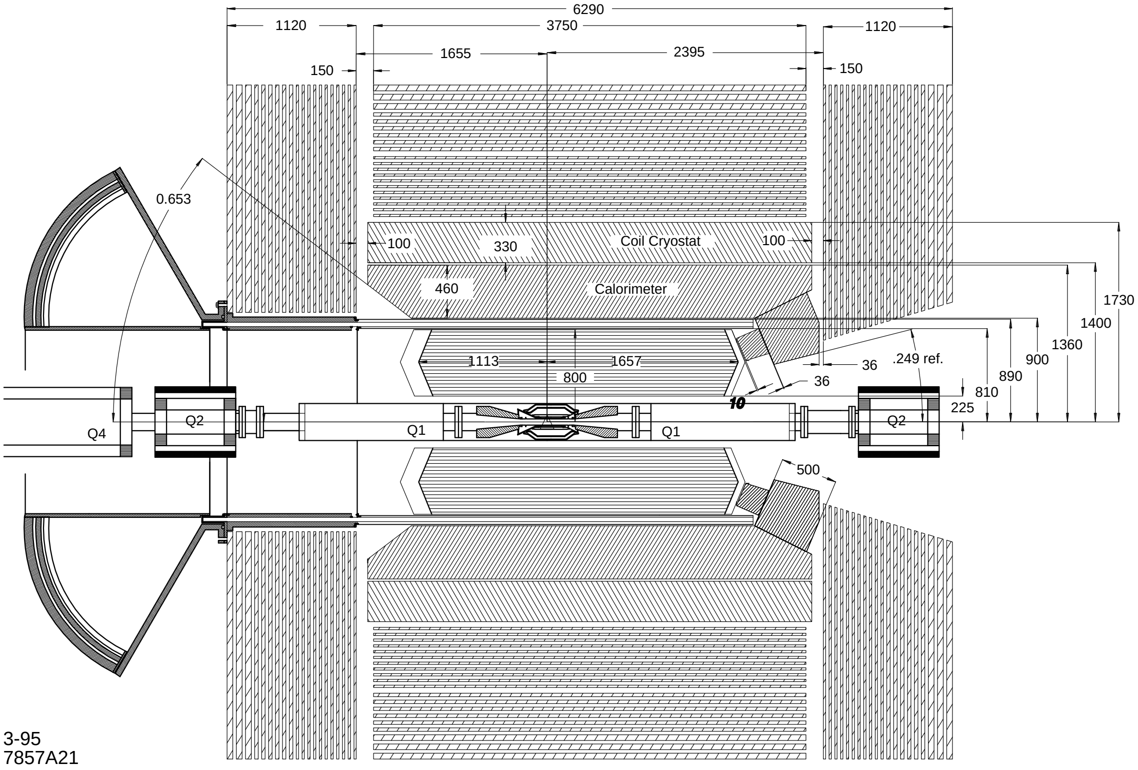

Figure 2.4: BABAR detector longitudinal section.

Since the average momentum of charged particles produced in B-meson decay is less than 1 GeV$/c$, the precision of the measured track parameters is heavily influenced by multiple Coulomb scattering. Similarly, the detection efficiency and energy resolution of low energy photons are severely impacted by material in front of the calorimeter. Thus, special care has been taken to keep material in the active volume of the detector to a minimum.

All *BABAR* detector systems share a common electronics architecture. Event data from the detector flows through the Front-End Electronics (FEE), while monitoring and control signal are handled by a separate, parallel system, the Online Detector Control (ODC). All FEE systems are mounted directly on the detector to optimize performance and to minimize the cable plant, thereby avoiding noise in long signal cables. FEE consists of signal processing and digitization electronics and a trigger latency buffer for storing data during the trigger processing before to transfer data to the data acquisition system.

The trigger system operates as a sequence of two independent stages, the first level, Level 1 (L1), is implemented in hardware, the other, conditional upon the first, Level 3 (L3), in software. The L1 trigger selection is based on data from DCH, EMC, and IFR. The maximum L1 response latency for a given collision is 12 μs. Based on both the complete event and L1 trigger information, the L3 software algorithms select events of interest which are then stored for processing. The L3 output rate is limited to 120 Hz so as not to overload the downstream storage and processing capacity.

The ODC system controls and extensively monitors the electronics, the environment, and assures the safety of the detector. Its implementation is based on the Experimental Physics Industrial Control System (EPICS) toolbox [44], providing detector-wide standardization for control and monitoring, diagnostics and alarm handling. Monitoring data are archived in an *ambient database*.

A summary of the *BABAR* detector systems is given in table 2.1.

Table 2.1: Overview of the coverage, segmentation, and performance of the BABAR detector systems. The notation (C), (F), and (B) refers to the central barrel, forward and backward components of the system, respectively. The detector coverage in the laboratory frame is specified in terms of the polar angles θ_1 (forward) and θ_2 (backward). The number of readout channels is listed. The dynamic range (resolution) of the FEE circuits is specified for pulse height (time) measurements by an ADC (TDC) in terms of the number of bits (nsec). Performance numbers are quoted for $1\,\mathrm{GeV}/c$ particles, except where noted. The performances for the SVT and DCH are quoted for a combined Kalman fit (for the definition of the track parameters, see sec. 2.3.1.)

System	θ_1 (θ_2)	No. Channels	ADC (bits)	TDC (ns)	No. Layers	Segmentation	Performance
SVT	20.1° (-29.8°)	150K	4	–	5	$50-100\mu$m r$-\phi$ $100-200\mu$m z	$\sigma_{d_0} = 55\mu$m $\sigma_{z_0} = 65\mu$m
DCH	17.2° (-27.4°)	7,104	8	2	40	6–8mm drift distance	σ_ϕ = 1 mrad $\sigma_{tan\lambda} = 0.001$ $\sigma_{p_t}/p_t = 0.47\%$ $\sigma(dE/dx) = 7.5\%$
DIRC	25.5° (-38.6°)	10,752	–	0.5	1	35×17mm^2 ($r\Delta\phi \times \Delta r$) 144 bars	σ_{θ_C} = 2.5 mrad per track
EMC(C)	27.1° (-39.2°)	2×5760	17–18	–	1	47×47 mm^2 5760 cystals	$\sigma_E/E = 3.0\%$ $\sigma_\phi = 3.9$ mrad $\sigma_\theta = 3.9$ mrad
EMC(F)	15.8° (27.1°)	2×820			1	820 crystals	
IFR(C)	47° (-57°)	22K+2K	1	0.5	19+2	20–38mm	$90\%\mu^\pm$ eff. $6-8\%\pi^\pm$ mis-id (loose selection, $1.5-3.0\,\mathrm{GeV}/c$)
IFR(F)	20° (47°)	14.5K			18	28–38mm	
IFR(B)	-57° (-26°)	14.5K			18	28–38 mm	

2.2.1 Background and *BABAR* protection

Beam-generated backgrounds affect the detector causing radiation damage to the electronics and to the components, limiting the lifetime of the experiment and generating extraneous signals that can degrade resolution and decrease efficiency. Many sources of background are present during normal running conditions: synchrotron radiation from accelerated electrons and positrons; interactions between the beam particles and the residual gas in the rings; electromagnetic showers generated by beam-beam collisions. To know the amount of radiation accumulated, a system that monitors the instantaneous and integrated dose is installed on SVT, DCH and EMC.

In particular, for the SVT there are twelve diodes (called PIN-diodes). They are mounted on three horizontal planes, placed at $z = +12.1cm$ and $z = -8.5cm$ at a radial distance of 3 cm from the beam line. The four PIN-diodes in the middle are exposed to a radiation 10 times more intense than the others. These diodes are connected to the beam abort system while the others are used to monitor the integrated dose. To dump a beam could be necessary in case of very high radiation level. Trip thresholds are set to two different time scales: an the instantaneous dose of the order of 1 rad/ms and an average of 50 mrad/s over a 5-min period. After every beam dump the 10-15 min period of injection has significant radiation exposure, so high-dose events are tolerated as long as the dose remains less than the thresholds to maximize the ratio of integrated luminosity over the integrated radiation. During the injection thresholds are imposed to higher levels, in order to return quickly to take data.

Since the first year of running, PIN-diodes protected the SVT well but they suffered the damage from the integrated dose. The radiation dose is measured by the current in the PIN-diode generated by the passing of particles. Each PIN-diode has a high leakage current which must be subtracted from the total current in order to measure the signal current from radiation. This leakage current has a temperature dependence (roughly $10\%/K$) and increase with the radiation damage (currently is of the order of 2-3 μA). For this reason, new sensors are developed, the pCVD diamonds [45], which are much more radiation hard than silicon-based sensors. They were installed near the SVT and under test since 2002; the replacement of PIN-diodes is expected in 2005.

2.2.2 The SVT

The Silicon Vertex Tracker (SVT) has been designed to provide precise reconstruction of charged particle trajectories just outside the beam pipe, thus minimizing the impact of multiple scattering on the extrapolation to the vertex. This is critical for the measurement of the time-dependent CP asymmetry. The mean vertex resolution along the z-axis for a fully reconstructed B decay must be better than 80 μm and of order $\sim 100\mu m$ in the plane perpendicular to the beam line [46].

Many of the decay products of B mesons have low p_t. The SVT must provide standalone tracking for particles with transverse momentum less than 120 MeV$/c$, the minimum that can be measured reliably in the DCH alone. This feature is fundamental for the identification of “slow” pions from D^*-meson decays: a tracking efficiency of 70% or more is desiderable for tracks with a transverse momentum in the range 50-120 MeV$/c$. Beyond the standalone tracking capability, the SVT provides the best measurement of track angles, critical to contain uncertainties on the DIRC Cherenkov angle for high momentum tracks.

The SVT (fig. 2.5) is composed of five layers of double-sided silicon strip sensors ($300\mu m$ thick) that are assembled from modules with readout at each end, thus reducing the inactive material in the acceptance volume. The inner three layers provide position and angle information for the measurement of the vertex position. The outer two layers are at much larger radii, providing the coordinate and angle measurements needed for linking SVT and DCH tracks. The spatial resolution for perpendicular tracks is $10-15\mu m$ in the three inner layers and about $40\mu m$ in the two outer layers.

Each layer is organized in 6, 6, 6, 16, 18 modules, starting from the innermost. Strips on opposite sides of each sensor are oriented parallel (ϕ strips) and transversely (z strips) to the beam axis. Modules of the inner three layers are straight, while to minimize the amount of silicon

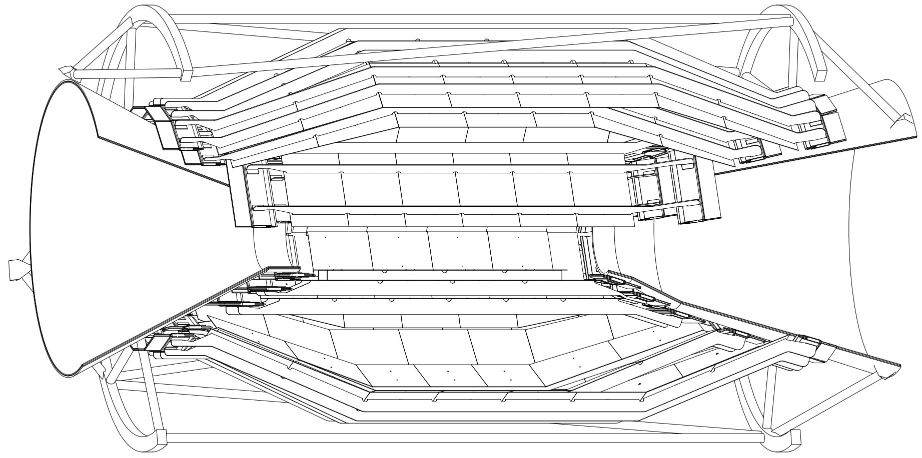

Figure 2.5: A three dimensional view of the Silicon Vertex Tracker.

required to cover the solid angle, and to increase the crossing angle for particles near the edges of acceptance, the modules of layers 4 and 5 are arch-shaped.

Allowing an overlap region, the inner modules are tilted in ϕ by 5 degrees while layers 4 and 5 are divided into two sub-layers and placed at slightly different radii.

The support structure is a rigid body made from two cones connected by a frame, all in carbon-fiber. SVT is cooled to remove the heat generated by the electronics. Since it is inaccessible during normal detector operations, reliability and robustness are essential and redundancies are built in whenever possible and practical. Major concerns for SVT monitoring are temperature and humidity, mechanical position, and radiation dose (see sec. 2.2.1). A cooling system is provided with water at 8 degrees Celsius, to eliminate the 350 W dissipated by the SVT modules mainly in the Front End Electronics (FEE). Humidity is reduced by a stream of dry air in the support tube to avoid condensation. Thermistors and humidity sensors are employed to check the SVT conditions and are used as an interlock to the power supplies in case of risk of damage.

The FEE consist of *A Time-Over-Threshold Machine* (ATOM) chips, connected with a thin *kapton tail* to the *matching cards*. Digitized signals are *multiplexed* by the MUX modules, converted into optical signals and transmitted to the *Readout Modules* (ROMs). The power to the SVT modules (silicon sensor bias voltage and ATOM low voltages) is provided by a CAEN A522 power supply system.

The ATOM chips (fig. 2.6) receive the signals from the silicon sensors. There is a linear analog section composed of a preamplifier followed by a shaper; the signals are then presented to a comparator, designed so that the output width of the pulse (*Time over Threshold* or ToT) is a quasi-logarithmic function of the collected charge. This output is sampled at 30 Mhz and stored in a 193 location revolving buffer. Upon receipt of a L1 trigger, the time and the ToT is retrieved from this latency buffer and stored; then, if the event is accepted, the output data are sent to the ROMs.

Once a day, and each time the SVT configuration changes, calibrations are performed in the absence of circulating beams. Gain, thresholds and electronic noise are measured, and defective channels are identified. The calibration results have proven very stable and repeatable and are useful to occasionally discover a new defective channel.

Since the support tube structure is mounted on the PEP-II accelerator supports, independently of *BABAR*, the SVT needs to be aligned with respect to the rest of the detector, in particular the DCH. The alignment is performed in two steps: first determining the relative positions of the 340

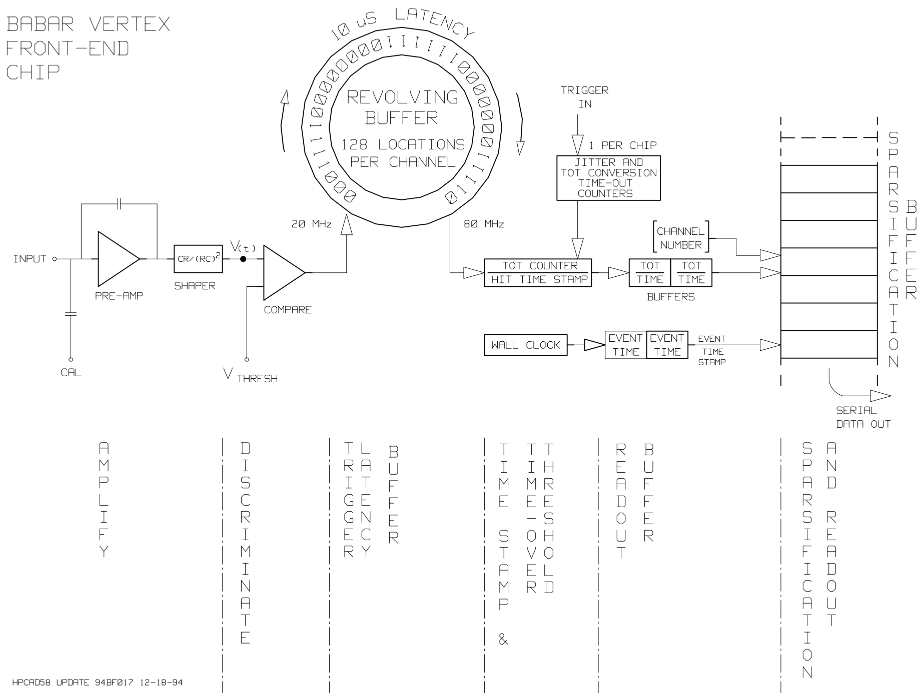

Figure 2.6: The ATOM chip.

silicon sensors (local calibration) using tracks from $e^+e^- \to \mu^+\mu^-$ events and cosmic rays; then doing an alignment with the global coordinate system defined by the DCH using tracks with sufficient numbers of SVT and DCH hits. The global alignment parameters are obtained minimizing the difference between track parameters obtained with the SVT-only and DCH-only fits.

The alignment constants obtained in a given run are then used to reconstruct data in the subsequent run (*rolling calibration*) to correct displacements that can occur during the day due to variations of temperature or after magnet quenches, as an example. Movements within a single run are small compared to the size of the beam.

2.2.3 The DCH

The principal purpose of the Drift CHamber (DCH) is the momentum measurement for charged particles. It also supplies information for the charged particle trigger and a measurement of dE/dx for particle identification. A resolution of about 7% allows π/K separation up to 700 MeV$/c$. The reconstruction of decay and interaction vertices outside of the SVT volume, for instance the K_S^0 decays, relies solely on the DCH.

The DCH (fig. 2.7) is of compact design, 3 m long, with 40 layers of hexagonal cells. Longitudinal information is derived from wires placed in 24 of the 40 layers at small angles with respect to the z-axis. The layers are grouped by four into ten superlayers, with the same wire orientation and equal numbers of cells in each layer of a superlayer. The stereo angles of the superlayers alternate between axial (A) and stereo (U,V) pairs, in the order AUVAUVAUVA (fig. 2.8). The stereo angles vary between $\pm 45\,\mathrm{mrad}$ and $\pm 76\,\mathrm{mrad}$.

The 7104 drift cells are small: $1.2 \times 1.8\,\mathrm{cm}^2$ along the radial and azimuthal directions, respectively. The hexagonal cell configuration is desirable because approximate circular symmetry can be achieved over a large portion of the cell. Each cell consists of one sense wire surrounded by six field wires. The sense wires are $20\mu m$ gold-plated tungsten-rhenium, the field wires are $120\mu m$

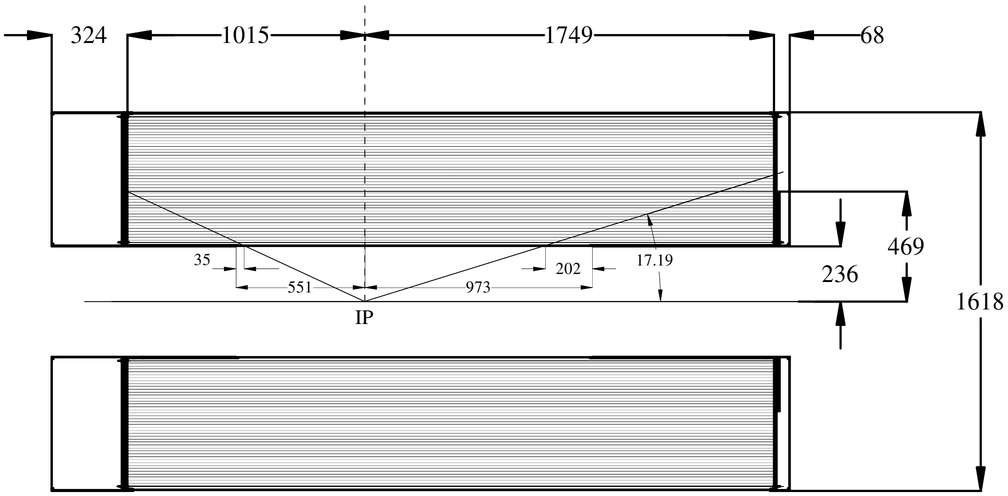

Figure 2.7: Side view of the BABAR drift chamber. The dimensions are in mm.

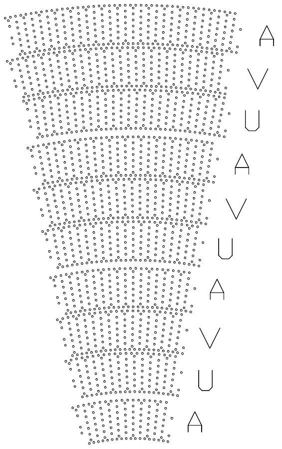

Figure 2.8: Cell layout in the BABAR drift chamber.

and 80μm gold-plated aluminum.

By choosing low-mass aluminum wires, and helium-based gas mixture (80:20 helium:isobutane) the multiple scattering inside the DCH is minimized having a good spatial and dE/dx resolution and reasonably short drift time. 50 ns isochrones in a typical cell in a 1.5 T magnetic field are shown in fig. 2.9. Spatial resolution of the DCH is 140 μm.

The chamber volume is about 5.2 m^3. Gas mixing is controlled by mass flow controllers; the total flow is tuned to 15 $l/$min, of which 2.5 $l/$min are fresh gas. Complete DCH gas volume is recirculated in six hours, and one full volume of fresh gas is added every 36 hours. The pressure is maintained at 4 mbar.

The voltages of the sense wires was initially set to 1960 V and for the field-shaping wires at the boundaries of the superlayers to 340 V, supplied by HV assemblies. Guard wires are connected to the ground. The chamber voltage was lowered for part of the first run to 1900 V because a small region of the chamber that was damaged during the commissioning phase by inadvertently applying 2 kV to the guard wires. The wires in this region are now disconnected and the HV is

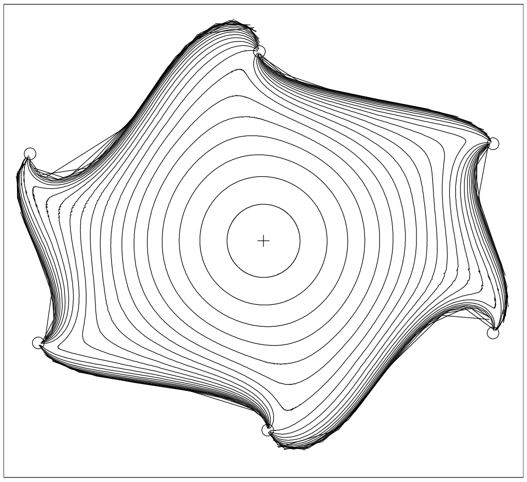

Figure 2.9: 50 ns isochrones in a typical BABAR drift chamber cell.

currently set to 1930 V for all the others.

The readout electronics are mounted on the backward endplate of the chamber, minimizing the amount of material in front of the calorimeter endcap and eliminating the heavily shielded cable plant. DCH amplifier and digitizer electronics are installed in electronics front-end assemblies (FEAs). The readout is segmented in 16 sectors that reflect the 16-fold symmetry of the cell pattern. These sectors are separated by brass cooling bars that provide mechanical support and water cooling.

TDCs and FADCs detect the leading edge of the signal from the charge arriving at the sense wire, then amplify and digitize the time with 1 ns resolution. The data are written through a $12\mu s$ trigger latency buffer into 4 levels of event buffers to minimize the dead time. The electronics provides prompt trigger signals by sending the hit information from all 7104 channels to the Level 1 Trigger system at a sampling frequency of 3.75 MHz. The system is designed to maintain good performance in severe background conditions. The expected single-cell efficiency for the trigger signal is greater than 95%.

2.2.4 The DIRC

In order to investigate rare decays like $B^0 \to \pi^+\pi^-$ and $B^0 \to K^+\pi^-$ kaons and pions must be well identified even if they have momenta greater than 1.7 GeV$/c$ where their de/dx measurements are not well separated. The *Particle Identification* (PID) system relies on the *Detector of Internally Reflected Cherenkov* light (DIRC) for π/K separation of $\sim 4\sigma$ or greater, for all tracks up to 4.2 GeV$/c$. In a quartz radiator (refractive index close to 1.474), the Cherenkov threshold for kaons (460 MeV$/c$) is well below the value of momentum for which there is no possible confusion between a pion and a kaon through ionization loss measurement (dE/dx) in the drift chamber (700 MeV$/c$): the two systems are remarkably complementary as far as π/K separation is concerned. Anyway PID below 700 MeV$/c$ relies primarily on the dE/dx measurements in the DCH and SVT.

The DIRC is based on the principle that the magnitudes of angles are maintained upon reflection from a flat surface. The DIRC radiator (see fig. 2.10) consists of 144 long, straight bars of synthetic quartz with rectangular section, arranged in a 12-sided polygonal barrel. The bars have transverse dimensions of 1.7 cm thick by 3.5 cm wide, and are 4.9 m long.

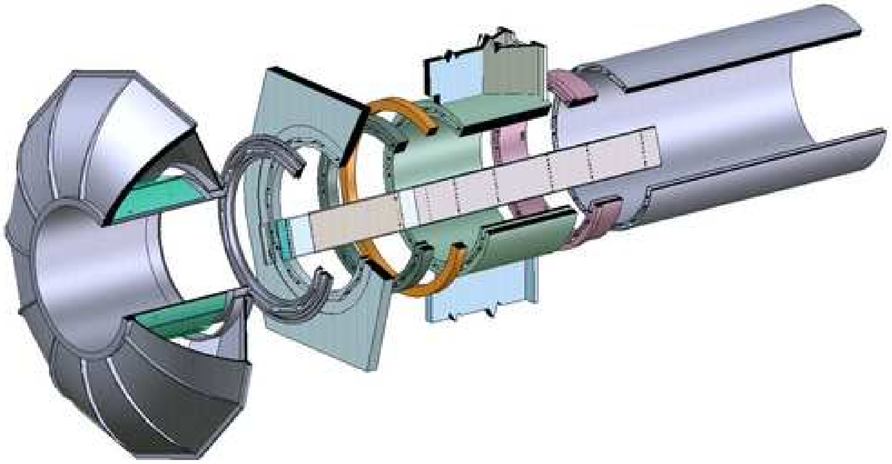

Figure 2.10: The DIRC detector.

The DIRC radiator extends through the steel of the solenoid flux return in the backward direction, to bring the Cherenkov light, through successive total internal reflections, outside the tracking and magnetic volumes. Only this end of the bars is instrumented. A mirror placed at the other end on each bar reflects forward-going photons to the instrumented end. The Cherenkov angle at which a photon was produced is preserved in the propagation, modulo a certain number of discrete ambiguities, some of which can be resolved by the photon arrival-time measurement. Remaining ambiguities are dealt with by the pattern recognition during Cherenkov angle reconstruction. The measurement of this angle with the knowledge of the track angle and momentum from the DCH allows a determination of the particle velocity.

An advantage of the DIRC for an asymmetric collider is that high momentum tracks are boosted forward which causes a much higher light yield than for particles at normal incidence. This is due to two effects: the longer path lenght in the quartz and the larger fraction of light emitted. In the nominal 1.5 T magnetic field, the DIRC radiator polygon, with an internal radius of 80 cm, can only be reached by particles produced (at the IP) with transverse momenta larger than 250 MeV$/c$.

At the instrumented end, the Cherenkov image is allowed to expand. The expansion medium is purified water (de-gassed, de-ionized and free of bacteria), whose refractive index matches reasonably well that of the bars, thus minimizing the total internal reflection at the quartz-water interface. About 11.000 photomultiplier tubes (PMTs) of 2.82 cm diameter operating directly in water, collect the Cherenkov light. They are equipped with light concentrators and shielded to maintain the magnetic fringe field at an acceptable level for PMT operation.

The dominant contributor to the overall detection efficiency is the quantum efficiency of the PMT. Taking into account additional wavelength independent factors, such as the PMT packing fraction and the geometrical efficiency for trapping Cherenkov photons in the fused silica bars via total internal reflection, the expected number of photoelectrons is ~ 28 for a $\beta = 1$ particle entering normal to the surface at the center of a bar, and increases by over a factor of two in the forward and backward directions.

2.2.5 The EMC

The electromagnetic calorimeter (EMC) is located outside the DIRC and within the magnet cryostat. It is designed to detect electromagnetic showers with excellent energy and angular resolution over the energy range from 20 MeV to 4 GeV. This coverage allows the detection of low energy π^0s from B and D_{sJ} decays and higher energy photons and electrons from electromagnetic, weak, and radiative processes.

The EMC is built in two sections, a barrel and a forward endcap (figure 2.11) made of thallium-doped cesium iodide (CsI(Tl)) crystals. Each crystal is a trapezoid with a length that vary with the polar angle from 16.1 (29.76 cm) to 17.6 (32.55 cm) radiation lengths starting from the backward. The transverse size of the crystals is chosen to be comparable to the Molière radius (3.8 cm). The crystals are arranged in modules that are supported individually from an external support structure.

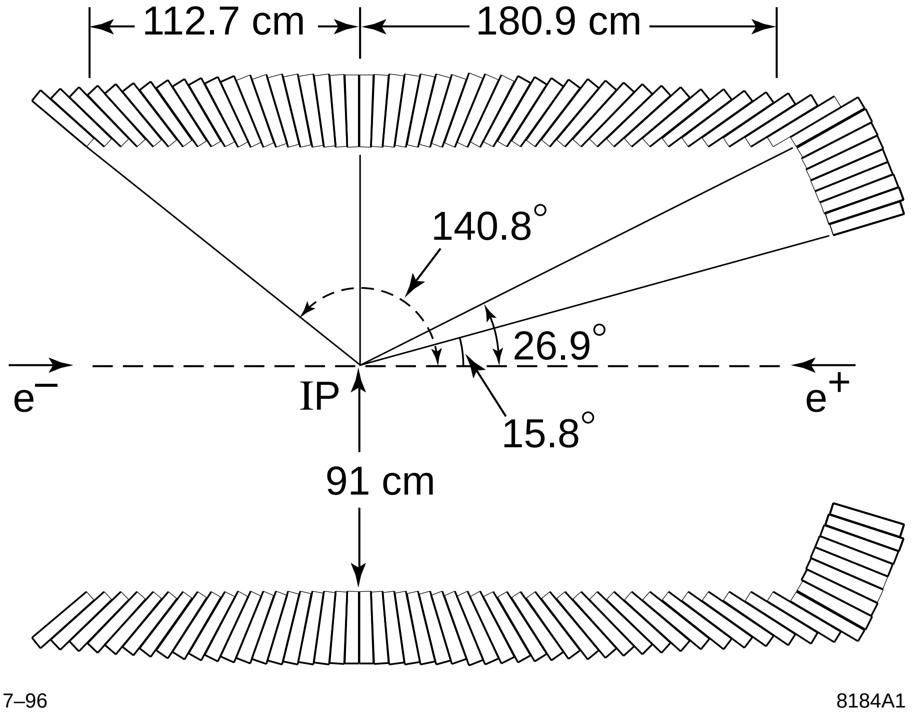

Figure 2.11: The EMC barrel and forward endcap.

The barrel consists of 5760 crystals arranged in 48 polar-angle (θ) rows of 120 crystals each. The endcap is constituted with 9 radial rows of crystals. The angle coverage corresponds to $-0.916 \leq cos\theta \leq 0.895$ in the center-of-mass frame.

To obtain the desired resolution, the amount of material in front of and in between the crystals is held to a minimum. The energy resolution of a homogeneous crystal calorimeter (see fig. 2.12) can be described empirically in terms of a sum of two terms added in quadrature

$$\frac{\sigma_E}{E} = \frac{\sigma_1}{\sqrt[4]{E(\mathrm{GeV})}} \oplus \sigma_2, \tag{2.1}$$

where E and σ_E refer to the energy of a photon and its error, measured in GeV. The energy dependent term σ_1 arises primarily from the fluctuations in photon statistics, but it is also impacted by electronic noise of the photon detector and electronics. Furthermore, beam-generated background

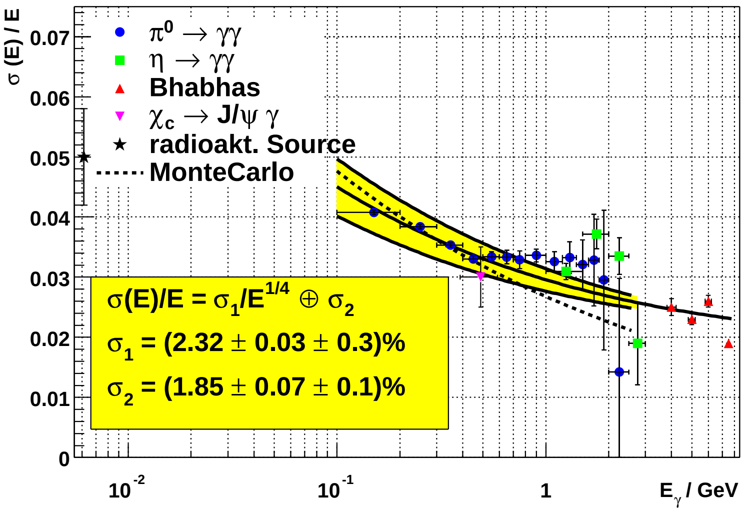

Figure 2.12: *EMC resolution as a function of the energy.*

will lead to large numbers of additional photons that add to the noise. This term is dominant at low energies. The constant term, σ_2 is dominant at higher energies ($> 1\,\text{GeV}$). It arises from non-uniformity in light collection, leakage or absorpion in the material between and in front of the crystals, and uncertainties in the calibrations.

The angular resolution is determined by the transverse crystal size and the distance from the interaction point. Empirically

$$\sigma_\theta = \sigma_\phi = \frac{c}{\sqrt{E(\text{GeV})}} + d \tag{2.2}$$

where $c \approx 3$ mr and $d \approx 2$ mr and E is measured in GeV.

The individual crystals are read out by pairs of silicon PIN photodiodes. The diodes are operated at a voltage of 50 V. They have a quantum efficiency of 85% for the CSI(Tl) scintillation light. Calibration is made with a 6.13 MeV radioactive source and using colliding beam events providing constraints: two-body final states such as e^+e^- (Bhabhas), $\gamma\gamma$, and $\mu^+\mu^-$, as well as radiative Bhabhas and $\gamma\gamma\gamma$ states, and a clean subset of $\pi^0 \to \gamma\gamma$ decays in more complex states.

2.2.6 The IFR

The instrumented flux return (IFR) is designed to identify muons and to detect neutral hadrons. Muons are important for *CP* violation studies, both to reconstruct the $J/\psi \to \mu^+\mu^-$ decay and to tag the B flavor in semileptonic decays.

For this purpose, the magnet flux return steel in the barrel and the two end doors is segmented into layers, increasing in thickness from 2 cm on the inside to 10 cm at the outside. Between these steel absorbers, single gap resistive plate chambers (RPCs) are inserted which detect streamers from ionizing particles via external capacitive readout strips.

By grading the segmentation it is possible to improve the performance without increasing too much the number of layers, in fact muon identification at low momentum and K_L^0 detection improve, for a given amount of absorber, as the thickness of the iron plates decreases. This effect is most important in the first absorption length.

There are 19 layers of RPCs in the barrel sectors and 18 layers of RPCs in the end doors. Two additional cylindrical layers of RPCs with four readout planes are placed at a radius just inside the magnet cryostat to detect particles exiting the EMC. The barrel extends radially from 1.78 to 3.01 m and is divided into sextants; the length of each sextant is 3.75 m, and the width varies from

1.88 to 3.23 m. Each endcap consists of hexagonal plates, divided vertycally into two parts to allow opening of the detector and has a central hole for the beam components and the magnetic shields. The total detector surface is ≈ 2000 m^2.

The RPC consist of two bakelite sheets, 2 mm thick and separated by a gap of 2 mm. The resistivity of the bakelite sheets is $10^{11} - 10^{12}\Omega$ cm. The external surfaces are coated with graphite connected to high voltage (≈ 8 kV) and ground, and protected by an insulating mylar film. The bakelite surfaces facing the gap are treated with linseed oil. The RPCs are operated in limited streamer mode and the signals are read out capacitively, on both sides of the gap, by external electrodes made of aluminum strips on a mylar substrate.

Each module has 32×32 orthogonal strips connected to the readout electronics. Even and odd numbered strips are connected to different front-end cards (FECs), so that a failure of a card does not result in a total loss of signal, since a particle crossing the gap typically generates signals in two or more adjacent strips.

The RPCs operate with a non-flammable gas mixture, Argon based (56.7%). The discharge generated by a ionizing particle is quenched by Freon (38.8%) that recapture the electrons, and isobutane (4.5%) that absorbs UV photons. Oil bubblers monitor the flow of the gas before and after the chambers and protect against overpressure limiting of about 1 Torr.

The efficiency of the RPCs is evaluated with cosmic ray. Two different algorithms are used: one that uses only IFR information and trigger, the other that uses tracks reconstructed in the DCH. All RPC modules were tested and their efficiency measured before installation: 75% of them exceed an efficiency of 90%.

Early test indicated that the RPC dark current was very temperature dependent, increases of $14-20\%$ per °C. After the first summer of operation, the temperature inside the steel rose to more than 37 °C and a large fraction of the RPCs($> 50\%$) showed very high dark currents and reduction in efficiency. Water cooling has been installed on the barrel and end door steel, stabilizing the temperature at $20-24$ °C. After this intervention some of the modules continued to deteriorate. For some of this, linseed oil accumulated at various spots under the influence of the electric field. Since summer 2004 substitution of RPC with Limited Streamer Tubes (LST) in the IFR has started.

2.3 Reconstruction methods

2.3.1 Tracking

The reconstruction of charged particle tracks use information from the SVT and the DCH. Charged tracks are defined by five parameters (d_0, ϕ, ω, z_0, $\tan\lambda$) and their associated error matrix (see fig. 2.13). They are characterised by the point of closest approach (P) to the z-axis; d_0 and z_0 are the distances of this point from the origin of the coordinate system in the $x-y$ projection and along the z-axis, respectively. The angle ϕ is the azimuthal angle of the track at point P, λ the dip angle relative to the transverse plane, and $\omega = 1/p_t$ is its curvature. The sign of d_0 and ω depends on the charge of the tracks. A Kalman-filter algorithm [47] that takes into account the distribution of material in the detector and the map of the magnetic field is used to find and fit tracks.

Tracks are first reconstructed in DCH superlayers, adding unassigned hits with two procedures to find tracks that either do not cross the entire DCH or do not originate from the interaction point. To the resulting tracks the segments found in the SVT are added. Those with the largest number of SVT layers and smallest number of residual hits are retained. The Kalman fit is performed on the DCH hits and on the full set of DCH and SVT hits. A minimum of four space points are required to form a good track. To recover tracks scattered in the support tube an attempt is made to combine tracks that are only found by one of the two tracking systems.

The absolute tracking efficiency of the DCH is determined as the ratio of the reconstructed

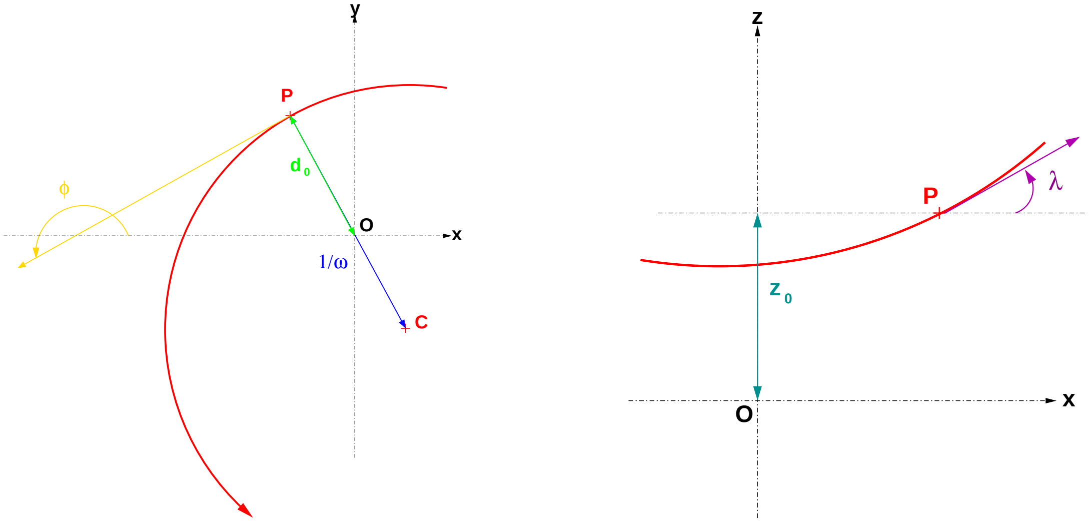

Figure 2.13: Charged tracks parameter definitions.

DCH tracks to the number of tracks detected in the SVT that fall within the DCH acceptance. At 1960 V voltage the efficiency averages 98 ± 1% per track above 200 MeV/c and polar angle $\theta > 500$ mrad. At 1900 V the efficiency is reduced by about 5% for tracks at close to normal incidence.

SVT have a high standalone tracking efficiency for tracks that have low transverse momentum. This feature is important for the detection of D^* decays. A detailed study of the relative efficiency for slow pion from $D^* \to D^0\pi$ decays is performed in sec. 2.4.

In *BABAR* there are standard criteria to select tracks for different analyses. In particular we use a “very loose” selection (Good Tracks Very Loose, GTVL) and a “loose” selection (Good Tracks Loose, GTL). The characteristics of the two selections are summarized in the following.

- GTVL:
  - momentum $p < 10$ GeV
  - distance of closest approach to (0,0) in the xy plane $d_0 < 1.5$ cm
  - absolute distance of closest approach to $z = 0$ $|z_0| < 10$ cm

  A detailed study on the “very loose” selection, with a computation of relative efficiency and estimation of the systematic error is given in sec. 2.4.

- GTL, in addition to the GTVL criteria:
  - transverse momentum $p_T > 100$ MeV
  - 12 or more DCH hits

  The efficiency for “loose” selected tracks as a function of p_t, θ, ϕ and of the number of tracks present in the event is shown in fig. 2.14. The average efficiency in data (simulation) is 96.37% (96.95%) for the HV of the DCH set to 1930 V. To correct for differences between simulation and data we apply a correction of -0.8% per track. The systematic error associated to this correction is 1.3% per track. If the event has a track multiplicity higher than 5, an additional factor of 0.7% to the systematic error should be added to compensate for the fact that the result was extracted from the analysis of low multiplicity $e^+e^- \to \tau^+\tau^-$

events [48] while there is a multiplicity dependence. In this case the total systematic error is 1.4% per track.

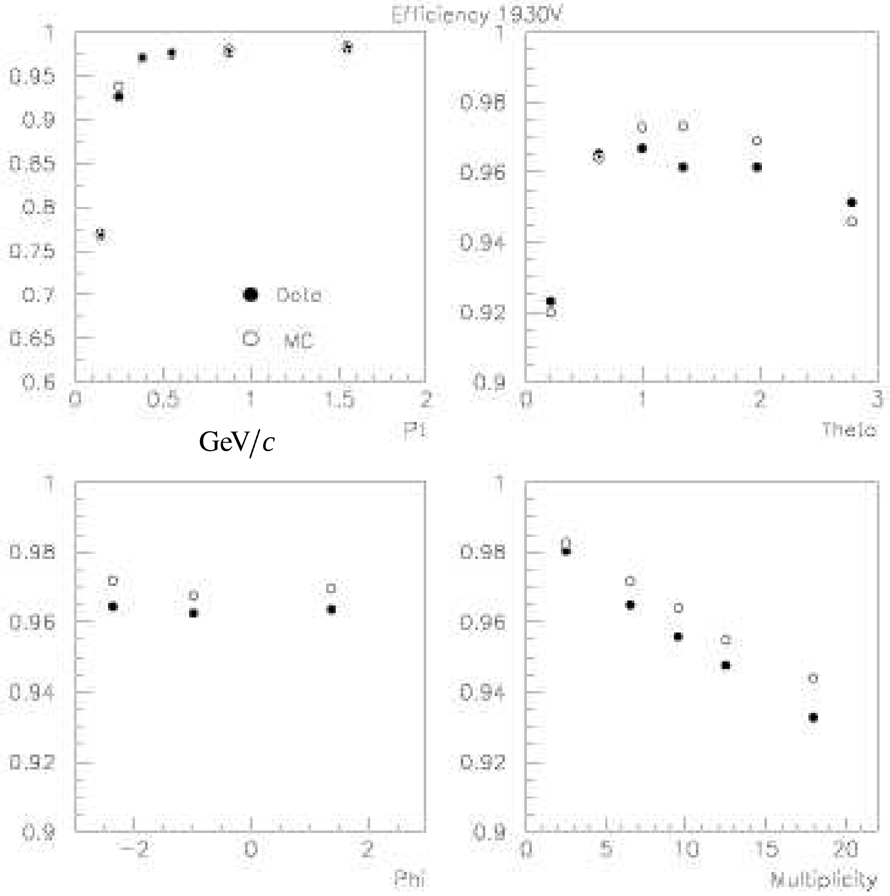

Figure 2.14: Good Tracks Loose efficiency plots for DCH at 1930 V. Black dots are from data and empty dots are from simulation. Dependence of efficiency on p_t, θ, ϕ and multiplicity are shown (starting from top left corner). There is a dependence on track multiplicity.

2.3.2 Particle identification

An unbinned maximum likelihood fit is performed to incorporate all information provided by the measurements of space (emitted Cherenkov angle) and time (arrival time of the photons) from the DIRC. The angular opening of the Cherenkov radiation cone depends on the particle speed:

$$cos\theta_c = \frac{1}{n\beta} \tag{2.3}$$

where θ_c is the Cherenkov opening angle, n is the refractive index of the material and β is the particle velocity divided by the speed of light. The reconstructed Cherenkov angle has an ambiguity that can be up to 16-fold. The reconstruction program associates the track with the candidate PMT signal within the intrinsic PMT time spread of 1.5 ns, overconstraining the measurement and dealing with ambiguities on the arrival time of photons and situations of high backgrounds.

The resolution on the track Cherenkov angle is

$$\sigma_{C,track} = \frac{\sigma_{C,\gamma}}{\sqrt{N_{pe}}} \tag{2.4}$$

where $\sigma_{C,\gamma}$ is the single photon angle resolution ($\sim$ 10.2 mrad) obtained from di-muon events and N_{pe} is the number of photoelectrons associated with the track.
Finally a likelihood value is provided for each of the five stable particle types (e, μ, π, K, p) for the track combining the information from SVT, DCH and DIRC.
In sec. 3.3 we will use two Particle IDentification (PID) criteria based on a likelihood value computed using dE/dx information from DCH and *Cherenkov* angle from DIRC. They are introduced here:

- **KMicroNotPion**: it is optimized with respect to kaon efficiency by rejecting identified pions not compatible with beeing a kaon ("Not A Pion"). A plot of selection efficiency versus momentum for these criteria is represented in fig. 2.15, 2.16;
- **KMicroTight**: it is designed to keep mis-identification below 5% up to momenta of 4 GeV$/c$. It uses the DIRC only for $p > 0.6$ GeV$/c$. The efficiency is lowered by the harder ("Tight") requirements, see also fig. 2.17, 2.18

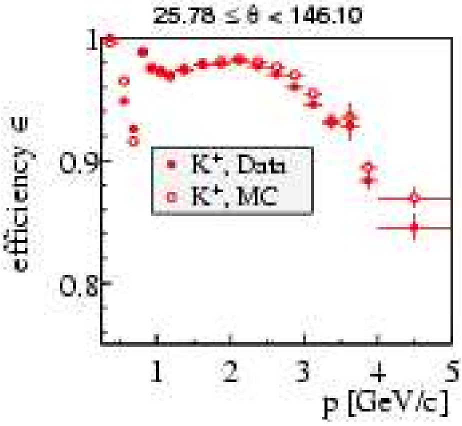

Figure 2.15: Efficiency vs momentum for kaons selected with "Not A Pion" PID criteria.

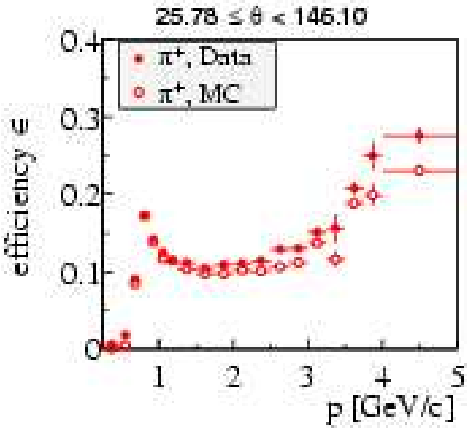

Figure 2.16: Fake rate vs momentum for pions selected with "Not A Pion" PID criteria.

2.3.3 Photon and π^0 reconstruction

Tipically a shower spreads over many adjacent EMC crystals forming a *cluster* of energy deposit. Clusters from different showers can merge and algorithms are necessary to differentiate clusters with one energy maximum from *bumps* of clusters with more than one local energy maximum.

A cluster should have at least one crystal with an energy above 10 MeV. If surrounding crystals exceeds a threshold of 1 MeV they are considered part of the cluster and also if they are contiguous neighbors of a crystal with at least 3 MeV. A bump is associated with a charged particle by projecting a track to the inner face of the calorimeter. If the distance between the bump centroid and the track impact point is consistent with the angle and momentum of the track, the bump is associated with this charged particle. Otherwise, it is assumed to originate from a neutral particle. Electromagnetic showers are separated from charged hadron showers on the basis of the shower

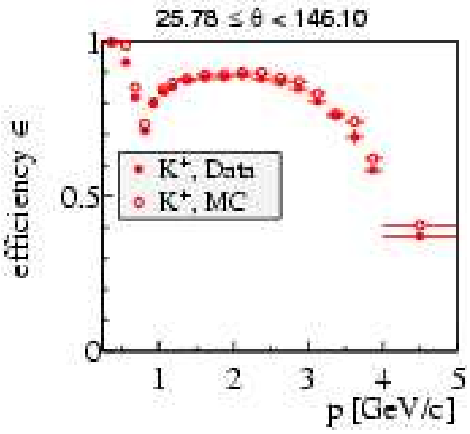

Figure 2.17: Efficiency vs momentum for kaons selected with “Tight” PID criteria.

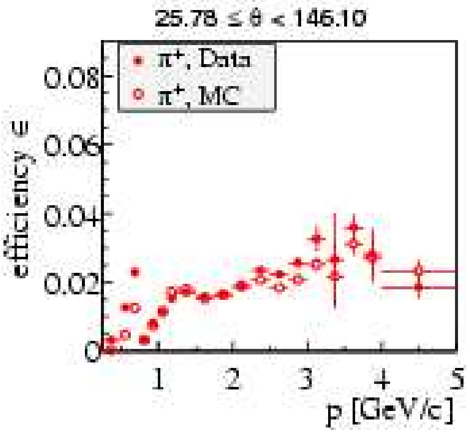

Figure 2.18: Fake rate vs momentum for pions selected with “Tight” PID criteria.

energy, lateral shower moments, and track momentum. The lateral distribution of the energy in a crystal (LAT) is defined in sec. B.2

To reconstruct a π^0, two γ showers are combined. The invariant mass resolution is dominated by the energy resolution at low energies and by the angular resolution at high energies because the two photons are almost collinear. In fig. 2.19 is reported the invariant m($\gamma\gamma$) for π^0 that satisfy a loose selection. See sec. 3.2.1 for more details about the selection of π^0 in $B \to D_{sJ}D^{(*)}$ decays.

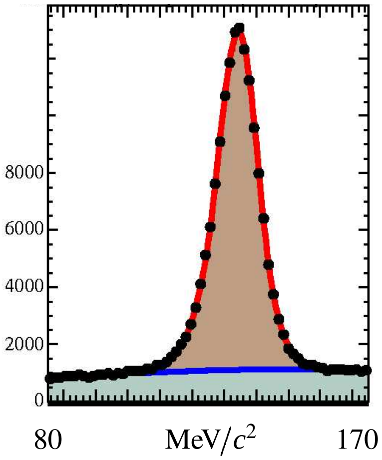

Figure 2.19: Invariant mass of π^0 selected in τ decays where the two photons have almost the same energy in the 500-750 MeV window. The fitted mass is 134.5 MeV/c^2 and the resolution is 6.4 MeV/c^2.

2.4 “Soft” pion reconstruction efficiency

The study of the reconstruction efficiency of the “soft” pion and the systematic error associated is fundamental not only for the $D_{sJ}D^*$ decays but also for all the analyses that make use of the D^*. Furthermore the identification of the charge of the D^* through the measurement of the soft pion is also used to tag the B flavor in analyses that need to distinguish between B^0 and $\bar{B}^0$.

In this section we will describe a technique, first introduced in [49], to extract the relative efficiency for low momentum charged pions, also called “soft” or “slow” pions, produced in a D^* decay. We then estimate the systematic uncertainty associated to tracks reconstructed and selected with the “very loose” criteria defined in sec. 2.3.1.

2.4.1 Motivations and method

The b quark mainly decays to a c quark, since the CKM matrix element $|V_{cb}|$ is close to unity; therefore in a B-factory there is a large production of charmed particles as secondary products of B decays. In particular, the inclusive D^* branching ratio in B decays is high: 22.5% [24]. The main decay mode for a D^* is $D^0\pi^+$ (67.7%) but the Q-value for this decay is quite small, 145.42±0.01 MeV, against a π mass of 139.57018±0.00035 MeV [24]; the decay into $D^+\pi^0$ is also possible (30.7%) but this is less favoured since the D^+ is heavier than the D^0. As a consequence of the small energy available, the momentum of the pion is also very low (π_s); its detection is difficult and depends strongly on the magnitude of the transverse momentum, determined by the angle of the emission in the detector. In general, particles that have low transverse momentum will cross only a few layers in the detector (or even no layer at all), and are less well measured, with loss of efficiency.

The goal of this section is to describe a method to estimate the inefficiency in the reconstruction of the soft pions as a function of their momentum in the laboratory. Since we cannot know the absolute number of lost soft-pions, we will measure a relative efficiency normalized to the efficiency for reconstructing high momentum tracks.

This method is based on the determination of the so called helicity angle θ^*, of the soft pion π_s in the two-body decay $D^{*+} \to D^0\pi_s^+$, defined as the angle between the π_s direction of motion in the D^* rest frame and the direction of motion of the D^* (fig. 2.20).

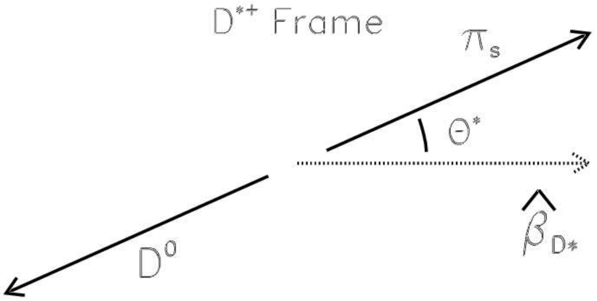

Figure 2.20: Definition of the slow pion helicity angle θ^*

It will be shown in par. 2.4.2 that the helicity angle θ^* distribution is an even function of $\cos\theta^*$. Any asymmetry that may appear in the distributions can be attributed to the efficiency loss in the detection of slow pions at small values of θ^*. To enhance this effect, since a slower D^* will correspond in average to a slower π_s, we look at the helicity angle distribution in different intervals of D^* momentum. We expect those corresponding to the slower D^* to be more asymmetric. In fact, for a given D^* momentum, the relation between the energy of the π_s and $\cos\theta^*$ is linear:

$$E_{\pi_s} = \gamma\,(E^*_{\pi_s} + \beta\; p^*_{\pi_s} cos\theta^*) \tag{2.5}$$

$$E^*_{\pi_s} = 145.0\,\mathrm{MeV}, \quad p^*_{\pi_s} = 39.3\,\mathrm{MeV}/c$$

where E_{π_s} is the energy in the laboratory, $p^*_{\pi_s}$ and $E^*_{\pi_s}$ are the momentum and the energy of the soft pion in the D^* rest frame; γ and β are the boost parameters of the D^* in the B rest frame.

The relative efficiency for reconstructing soft pions as a function of their laboratory momenta can be finally estimated from combined fit of the experimental helicity angle distributions in eight D^* laboratory momentum bins (sec. 2.4.3).

At PEP-II the D^* is produced in both B meson decays and in the fragmentation of $c\bar{c}$ events. The $p(D^*)$ distribution, fig. 2.21, shows a peak at low momentum from B decays and a long tail at higher momentum due to $c\bar{c}$ fragmentation. The division in eight bins of different widths is also shown. In each of them the relationship between the slow pion momentum and $\cos\theta^*$ is roughly linear. Fig. 2.21, shows the slow π laboratory momentum as a function of $\cos\theta^*$, for each bin of $p(D^*)$, for a mixture of $b\bar{b}$ and $c\bar{c}$ simulated events representative of the data collected at the $\Upsilon(4S)$. Any given slow pion momentum value is sampled by at least two $p(D^*)$ bins. This overlap makes it possible to determine the efficiency at low momentum relative to the efficiency at high momentum, where other independent efficiency measurements are possible.

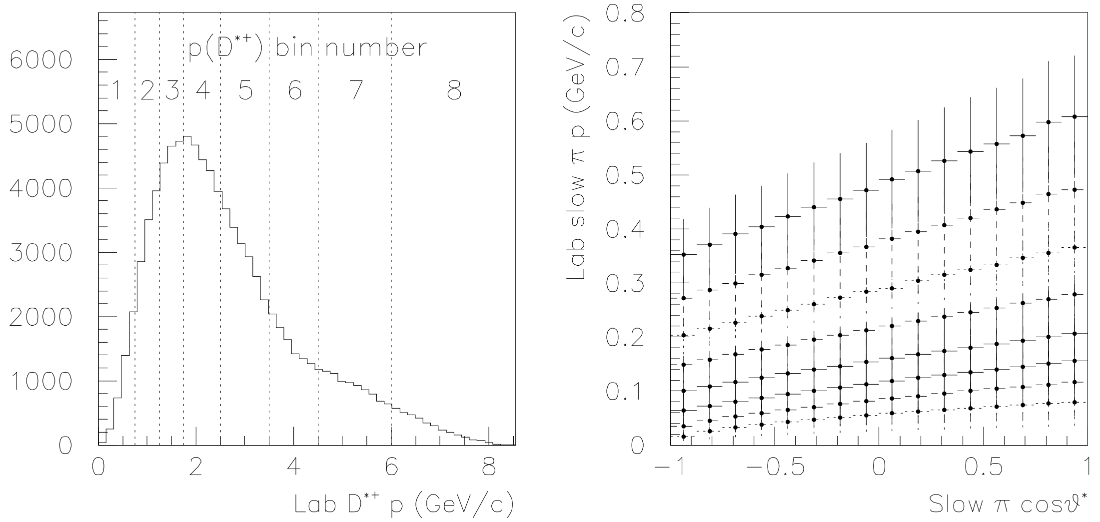

Figure 2.21: The histogram on the left shows the D^* laboratory momentum spectrum for a mixture of $b\bar{b}$ and $c\bar{c}$ simulated events representative of the data collected at the $\Upsilon(4S)$. The distribution is divided into eight bins. The plot on the right shows the slow π laboratory momentum as a function of the $\cos\theta^*$, where θ^* is the helicity angle defined in the text. The top (bottom) set of points is for $p(D^*)$ bin 8 (bin 1).

The analysis method including the subtraction of the background is described in par. 2.4.3. Results are summarized in sec. 2.4.4.

2.4.2 Helicity distribution

Let us now introduce a few basic concepts: the polarization, the alignment and the helicity of the particles, to understand why the helicity angle distribution is symmetric in D^* decays if experimental inefficiency effects are excluded.

In the quark model, a meson is composed of two spin $\frac{1}{2}$ valence quarks that can combine to form four spin states in the absence of orbital angular momentum. In the base J, and its z-component, J_z, they are the vector states $|1,1>$, $|1,0>$, $|1,-1>$, and the pseudoscalar state $|0,0>$. The helicity formalism describes the angular distributions and correlations in the production and decay of particles with non-zero spin. For a particle with momentum $\vec{p}$, the helicity is defined as

$$\lambda = \frac{\vec{J}\cdot\vec{p}}{|\vec{p}|}, \tag{2.6}$$

that in the case of a spin-1 particle is just the z-component of the spin when the z-direction has been chosen as the flight direction of the meson. The helicity density matrix, whose elements are formed of bilinear combinations of the helicity amplitudes, is used to organize information about the spin of a particle. The diagonal elements $\rho_{\lambda\lambda}$, with $\sum_{\lambda}\rho_{\lambda\lambda} = 1$, represent the probability that the particle has helicity λ.

Statistical expectations are that all helicity states of a spin J particle are equally populated, but production and fragmentation dynamics can lead to polarized particles. A system of particles is polarized if there is a net angular momentum, i.e. $\rho_{\lambda\lambda} \neq \rho_{-\lambda-\lambda}$ for some helicity λ. For the case of a vector meson decaying to two pseudoscalar mesons, the angular distribution can be written [50]

$$\frac{d\Gamma}{dcos\theta^*} = N_0\frac{3}{4}[(1-\rho_{00}) + (3\rho_{00}-1)cos^2\theta^*] \tag{2.7}$$

where θ^* is the helicity angle defined previously, and N_0 is a normalization factor. By using the variable

$$\alpha = \frac{3\rho_{00}-1}{1-\rho_{00}}, \tag{2.8}$$

the angular distribution can be re-expressed as

$$\frac{d\Gamma}{dcos\theta^*} = N(1+\alpha cos^2\theta^*) \tag{2.9}$$

where N is a normalization factor equal to $3/(6+2\alpha)$. The value of α can range between -1 and $+\infty$, where the angular distribution would be isotropic if $\alpha = 0$, proportional to $\sin^2\theta^*$ if $\alpha = -1$ and proportional to $\cos^2\theta^*$ if $\alpha \to \infty$. The α parameter is expected to be zero for D^* production from the continuum, but may be non-zero for D^* hadrons from B decay [51]. Since we will have D^* produced in both resonant (trough a B meson from $b\bar{b}$) and non-resonant (from fragmentation in $c\bar{c}$) decays, the information on α in the distribution will be mixed-up, at least for low momentum D^*. But the α value is not actually relevant in our analysis, since what matters is the symmetry in the helicity angle distributions. Moreover with more detailed studies it is possible, in principle, to disentangle α for $b\bar{b}$ and $c\bar{c}$.

As we already said, we can assume that any asymmetry observed in $d\Gamma/dcos\theta^*$ is therefore due to a relative efficiency asymmetry that can be mapped on to a specific part of the slow π momentum spectrum.

2.4.3 Analysis Procedure

In this section the procedure adopted to select events with a D^* candidate and estimate and subtract backgrounds is described in more detail. Particular care in background subtraction is needed to avoid producing additional distortions in the helicity distributions. At the end we will choose a function to model the soft pion efficiency and fit its parameters. The results are given in the next subsection.

We select the decay chain: $D^{*+} \to D^0\pi^+$, $D^0 \to K^-\pi^+$ and charge-conjugate, using only three tracks: one kaon, one fast pion, and one slow pion candidate. The soft π from the D^* is reconstructed following a “very loose” selection (GTVL) as defined in section 2.3.1. The kaon and the fast pion from the D^0 are also required to satisfy the “loose” conditions (GTL). All the tracks are required to be in the tracking fiducial volume defined by the polar angle θ: $-0.824 < cos\theta < 0.917$; outside this range the tracks fall outside the active detector geometry.

We require a converging vertex fit to combine the kaon and pion tracks into the D^0 candidate. We fix its mass to the nominal D^0 mass [24] (mass constraint), then reconstruct the D^* with the soft pion track. We refit the vertex with the slow pion with the mass constraint for the D^* candidate, since this procedure improves the invariant mass resolution,

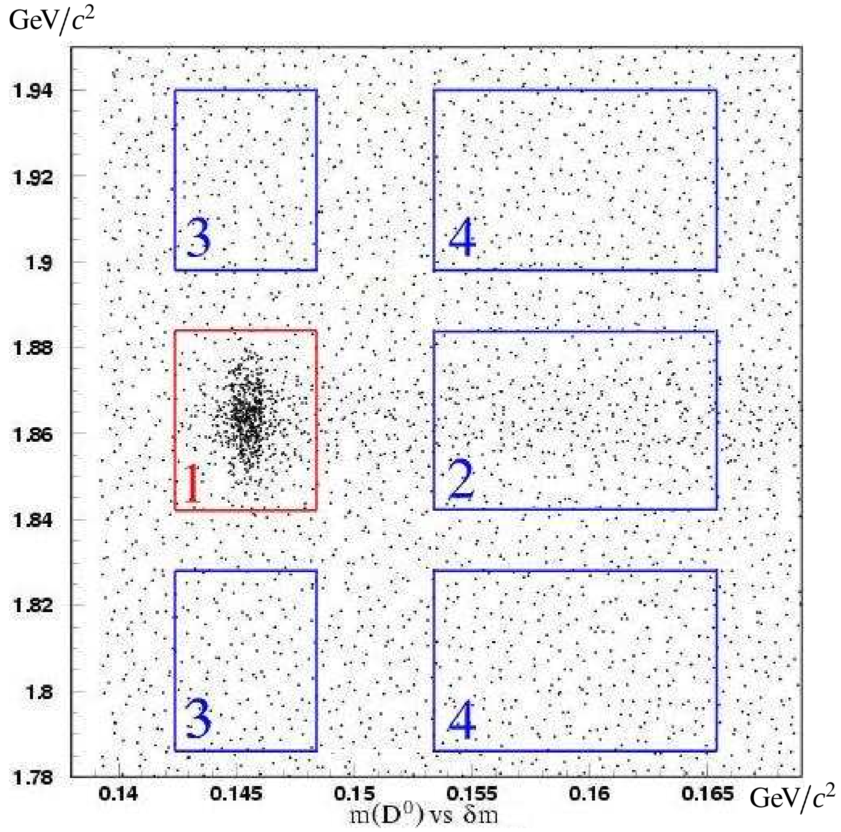

Figure 2.22: Signal (zone 1) and sideband regions (zone 2-4) in $\delta m - m(K\pi)$ plane.

To identify the kaon in the D^0 decay we use SVT, DCH and DIRC information: tracks that satisfy the particle identification requirement (PID) for the kaon hypothesis (KMicroNotPion criteria, defined in sec. 2.3.2) are used to reconstruct "Good-PID" D^* candidates. To define a control sample for an estimate of the background, other D^* candidates are formed in exactly the same way, but using for the kaon candidate a track that does not satisfy the PID requirement ("PID-antiselect" D^* candidates).

The background subtraction procedure uses two kinematic variables: m_{D^0} (the invariant mass $m(K\pi)$) and the difference between the invariant mass of the D^* and D^0 candidates $\delta m = m_{D^*} - m_{D^0}$. We define for the two variables a signal region, and a sideband region, that is used to estimate background events in the signal region by extrapolation. They are defined as (fig. 2.22):

- $m(K\pi)$ signal region: $1.863 \pm (3 \times 0.007)$ GeV/c
- $m(K\pi)$ sideband region: $(1.863 - 8 \times 0.007) \pm (3 \times 0.007)$ GeV/c
  and $(1.863 + 8 \times 0.007) \pm (3 \times 0.007)$ GeV/c
- δm signal region: $0.1454 \pm (3 \times 0.010)$ GeV/c
- δm sideband region:$(0.1454 + 14 \times 0.0010) \pm (6 \times 0.010)$ GeV/c

Reconstructed events can be classified in four categories:

1. **Signal candidates**: real $D^0 \to K^- \pi^+$ from a D^{*+} and a real slow pion from a D^{*+}; it should be in the small box region (zone 1).

2. **real-D^0 + bad-π_s**: a real $D^0 \to K^-\pi^+$ that may or may not have come from a D^{*+} combined with a slow pion that is a fake track or did not come from a D^{*+}; it should be in the intersection of $m(K\pi)$ signal region and δm sideband region (zone 2).

3. **bad-D^0 + real-π_s**: a mis-reconstructed D^0 with a real slow pion from a D^{*+}. This is mostly $D^0 \to K^-K^+$, $D^0 \to K^-\pi^+\pi^0$, $D^0 \to \pi^-\pi^+$, or cases where the kaon and pion assignments have been swapped; it should be in the intersection of δm signal region and $m(K\pi)$ sideband region. This is essentially signal and should not be subtracted (zone 3).

4. **Combinatoric background**: fake D^0 with a slow pion that is a fake track or did not come from a D^{*+};

The real background to be subtracted is the one described in point 2 and 4. The subtraction procedure requires a few steps for each bin n of the laboratory momentum of the D^* p_{D^*} and illustrated in fig. 2.23:

- consider the "PID-antiselect" sample (B) in the $m(K\pi)$ sideband region (zones 3 and 4); divide the number of events in the δm signal (zone 3) by the number of events in the δm sideband (zone 4). This gives the scale factor ($f^{(n)}$) to extrapolate the background from sideband to signal in δm in the n-th bin of p_{D^*}:

$$f^{(n)} = \frac{B_3^{(n)}}{B_4^{(n)}} \tag{2.10}$$

- consider the "Good-PID" (S) sample events in δm sideband region, $m(K\pi)$ signal region (zone 2) rescaled by the previous factor. This value is the factor $b^{(n)}$ to rescale background in the n-th bin of p_{D^*}:

$$b^{(n)} = S_2^{(n)} \cdot f^{(n)} \tag{2.11}$$

- use this factor to obtain the rescaled (R) $\cos\theta^*$ distribution given by the "PID-antiselect" sample in δm signal, $m(K\pi)$ sideband (events in zone 2):

$$\left(\frac{dN}{dcos\theta^*}\right)_R^{(n)} = \left(\frac{dN}{dcos\theta^*}\right)_{B_2}^{(n)} \cdot \frac{b^{(n)}}{B_2^{(n)}} \tag{2.12}$$

- subtract the previous result to the same distribution for the "Good-PID" sample in the signal region (red zone 1) to obtain the final distribution:

$$\left(\frac{dN}{dcos\theta^*}\right)_F^{(n)} = \left(\frac{dN}{dcos\theta^*}\right)_S^{(n)} - \left(\frac{dN}{dcos\theta^*}\right)_R^{(n)} \tag{2.13}$$

The goal of this rather complicated procedure is to estimate the amount of combinatoric background and background from real-D^0 and badly reconstructed π_s in the signal region, using background samples defined by sidebands, that cover the same soft pion kinematic range within each $p(D^*)$ bin n. The distributions are shown in fig. 2.24 The background subtracted distribution in $\cos\theta^*$ is fitted bin by bin in $p(D^*)$ with the angular distribution function (2.9) convoluted with the efficiency function:

$$\varepsilon(p) = \begin{cases} 1 - \frac{1}{\beta(p-p_0)+1} & \text{if } p > p_0 \\ 0 & \text{if } p \leq p_0 \end{cases} \tag{2.14}$$

where p_0 is the momentum value corresponding to the efficiency threshold and β describes how fast the efficiency function rises to the plateau value. The parameters fitted are eighteen: two for

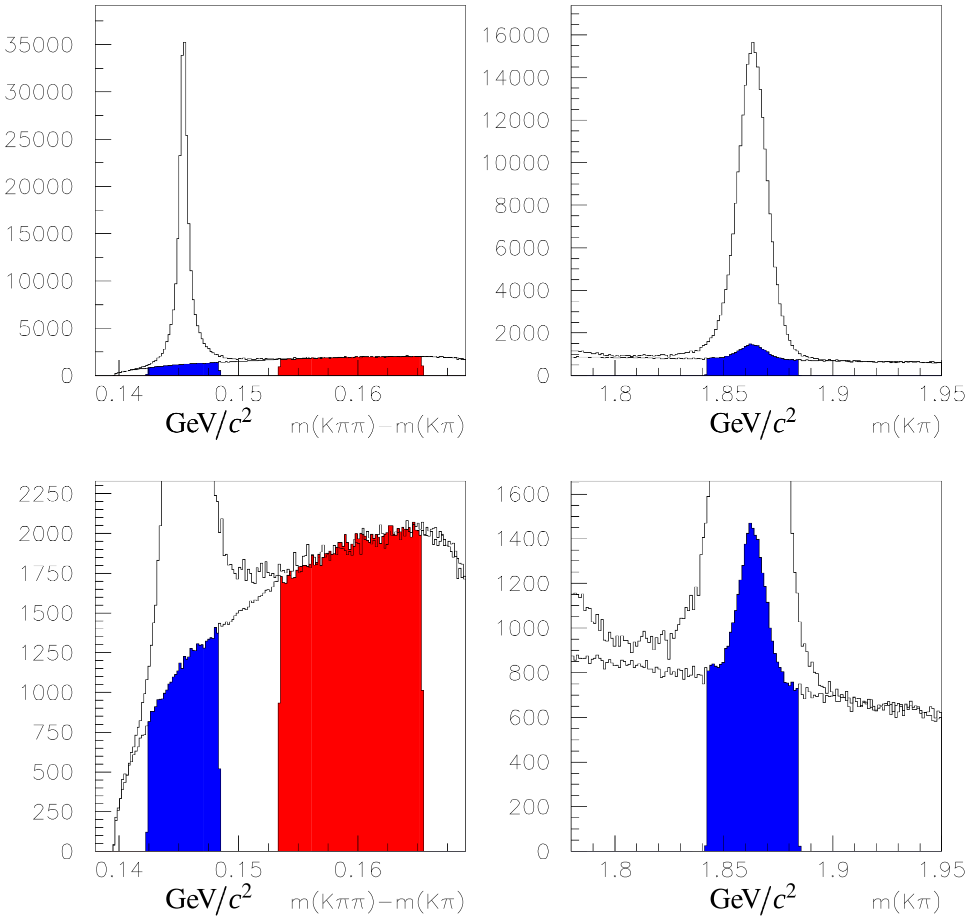

Figure 2.23: Background subtraction procedure: the plots on the left show the δm distribution of the signal (top histogram) and the PID-antiselect $m(K\pi)$ sideband (zoom in the bottom histogram) rescaled by the factor b computed in eq. 2.11. In this way the two samples agree in the δm sideband region by construction. The ratio of the area of the two colored regions (zone 3 and 4 in fig. 2.22) gives the scale factor f, computed in eq. 2.10, needed for comparing the δm signal and sideband regions (zone 1 and 2 in fig. 2.22) in $m(K\pi)$ shown on the right. The integral of the colored region in the plots on the right gives the amount of combinatoric and real-D^0 and badly reconstructed π_s background. The excess to the left of the $m(K\pi)$ peak in the signal distribution over the rescaled distribution from the δm sideband is due to $D^0 \to K^+K^-$ and $D^0 \to K^-\pi^+\pi^0$.

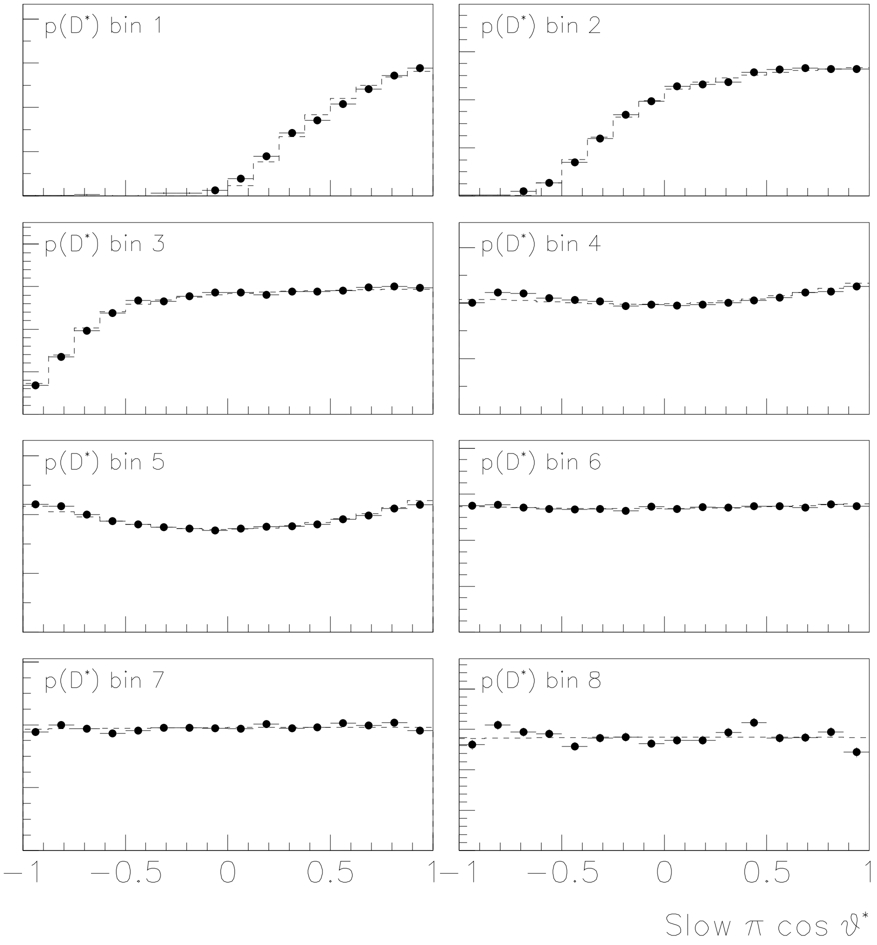

Figure 2.24: Helicity distribution and fit results for the on-resonance data. The events are divided in bins of $p(D^{*+})$ as shown in Figure 2.21, where bin 1 (8) is the lowest (highest) $p(D^{*+})$ bin. The points with error bars are background-subtracted reconstructed $\cos\theta^*$ *histograms and the dashed histogram is the result of the fit.*

each bin in $p(D^*)$ (N and α) and two for the efficiency function, β and p_0. Each $\cos\theta^*$ distribution has 16 bins. Since each bin in each of the $\cos\theta^*$ distributions covers a significant range in $\cos\theta^*$ and $p(D^{*+})$, a two-dimensional numerical integration is performed: for a given $\cos\theta^*$ bin n ($n = 1,16$) in the k^{th} distribution in bin k ($k = 1,8$), if i indicates a step in $\cos\theta^*$ within the given bin ($i = 1,10$) and j indicates a step in $p(D^{*+})$ within the bin ($j = 1,10$), the integration is calculated as

$$S_{nk} = \sum_{ij} \varepsilon(p_0, \beta, p_{ij}) \cdot N_k (1 - \alpha_k \cos\theta^*_i) \tag{2.15}$$

$$p_{ij} = \sqrt{(\beta_j \gamma_j p^* \cos\theta^*_i + \gamma_j E^*) - m^2_\pi} \tag{2.16}$$

The fit is performed minimizing the global χ^2:

$$\chi^2 = \sum_{nk} (D_{nk} - S_{nk})^2 / \sigma^2_{D_{nk}} \tag{2.17}$$

where D_{nk} is the height of bin n in histogram k and $\sigma_{D_{nk}}$ is the statistical error on D_{nk}. The integration above assumes a locally uniform distribution in $\cos\theta^*$. The asymmetry due to the changing efficiency is largest for the low $p(D^{*+})$ bins, as shown in fig. 2.24. The fit reproduces the experimental data satisfactorily (see sec. 2.4.4).

2.4.4 Results

The results of the fits are presented in table 2.2 for each DCH voltage subsample, that is for periods where the DCH tracking efficiency could vary due to different high voltage settings. It should be noted that the *BABAR* detector, using the SVT also for tracking purposes, achieves a very low threshold (about 65 MeV/c) for the detection of pions and reaches a relative efficiency of about 90% already at about 100 MeV/c.

Table 2.2: Results of the fit on various sample.

sample	β	p_0	χ^2
data 1999-2000 DCH 1900	175 ± 19	66.0 ± 0.4	1.60
data 2000 DCH 1960	147 ± 17	65.2 ± 0.5	1.25
data 2001 DCH 1930	170 ± 11	65.2 ± 0.2	2.81
data 2002	170 ± 13	65.8 ± 0.3	2.23
all data	170 ± 7	65.5 ± 0.2	4.78
simulation	148 ± 16	65.0 ± 0.4	1.40

The comparison of the relative efficiency curves obtained separately in data and simulation is useful to estimate the systematic uncertainty on the efficiency for reconstructing soft pions and in general to a track selected with “very loose” criteria (see fig. 2.25). Taking the integral of the efficiency as a function of soft π laboratory momentum for data and simulation, the relative

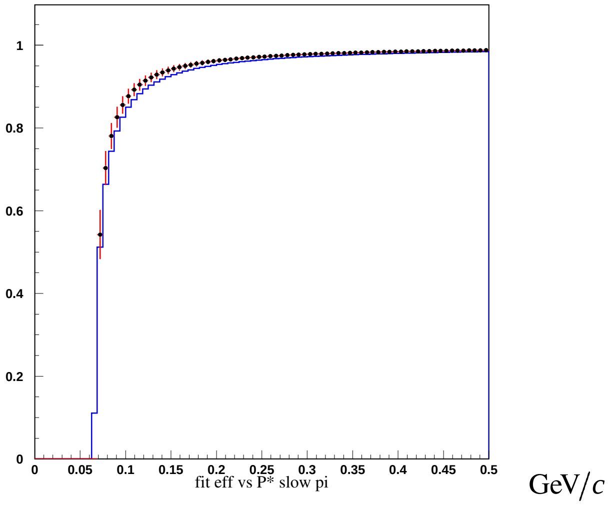

Figure 2.25: Relative efficiency as defined in eq. 2.14, for slow pions, for simulation (histogram) and for data (dots).

difference is 0.9%. For high-momentum “very loose” selected tracks the agreement between data and simulation is extracted from hadronic τ decays events [48]. The sum in quadrature of this number (1.3%) with the previous uncertainty give the final systematic value of 1.6%.

Chapter 3

The $B \to D_{sJ}D^{(*)}$ analysis

As shown in Section 1.3, the $B \to D_{sJ}D^{(*)}$ decays are the best environment to study the D_{sJ} states. In this chapter we will describe the analysis and the procedure to measure combined branching ratios of B and D_{sJ} decays and quantum numbers for the $D_{sJ}(2460)$.

The choice of decay channels and of the intermediate states (for instance D and D_s mesons), and the data samples used in this analysis are described in Section 3.1, together with the analysis strategy.

Pre–selection of a reduced data set is described in Section 3.2. Final selection criteria for intermediate particles 3.3 and for B candidates (Section 3.4) are based on a study of simulated signal and background events.

The methods used to study backgrounds peaking in the signal region, to estimate efficiencies and "cross–feed" between different signal channels are described in Section 3.5.

To validate the analysis method, we also use a *control sample* of decays $B \to D_s^{(*)}D^{(*)}$ using the same requirements to reconstruct the intermediate states; the branching ratios obtained are compared with the available previous measurements (Section 3.6).

Two different naming conventions for the two D_{sJ} states are based on the masses, $D_{sJ}^{*}(2317)$ and $D_{sJ}(2460)$, and plausible assumptions on the spin, D_{s0} and D_{s1}, respectively. The symbol $D^{(*)}$ is used to represent one of the mesons D^0, D^{*0}, D^-, D^{*-} and charge conjugates; a similar convention is used for $D_s^{(*)}$.

3.1 Analysis strategy

We will consider all the possible B final states containing a $D^{(*)}$ and a D_{sJ} mesons, that means the following eight B decay modes:

- $B^+ \to \bar{D}^0 D_{sJ}^*(2317)^+$; $B^+ \to \bar{D}^0 D_{sJ}(2460)^+$
- $B^O \to D^- D_{sJ}^*(2317)^+$; $B^O \to D^- D_{sJ}(2460)^+$
- $B^+ \to \bar{D}^{*0} D_{sJ}^*(2317)^+$; $B^+ \to \bar{D}^{*0} D_{sJ}(2460)^+$
- $B^O \to D^{*-} D_{sJ}^*(2317)^+$; $B^O \to D^{*-} D_{sJ}(2460)^+$

The D_{sJ} is reconstructed in the decay modes:

- $D_{sJ}^*(2317)^+ \to D_s^+ \pi^0$
- $D_{sJ}(2460)^+ \to D_s^{*+} \pi^0$

- $D_{sJ}(2460)^+ \to D_s^+\gamma$

What we actually measure is the product of the B and D_{sJ} branching ratios. So at the end we will have twelve measurements, distinguishing the two $D_{sJ}(2460)$ final states in the same B decay channel. We aim to observe previously unmeasured decay chains (final state with $D^{*\pm}$, D^{*0}), and improve the branching ratio ($\mathcal{B}$) measurements for known decays (final states with $D^\pm$ and D^0). We will use the decays $B^+ \to \bar{D}^0 D_{sJ}(2460)^+$ and $B^O \to D^- D_{sJ}(2460)^+$ to extract $D_{sJ}(2460)$ quantum numbers by means of an angular analysis.

The intermediate states are fully reconstructed in the following decays:

- $D^0 \to K^-\,\pi^+, D^0 \to K^-\,\pi^+\,\pi^0, D^0 \to K^-\,\pi^+\,\pi^-\,\pi^+$
- $D^+ \to K^-\,\pi^+\,\pi^+$
- $D_s^+ \to \phi\pi^+$ and $D_s^+ \to \bar{K}^{*0}\,K^+$, with $\phi \to K^+K^-, \bar{K}^{*0} \to K^-\pi^+$
- $D^{*0} \to D^0\pi^0, D^{*0} \to D^0\gamma$
- $D^{*+} \to D^0\,\pi^+$
- $D_s^{*+} \to D_s^+\gamma$

By adding selected π^0 or γ to reconstructed $D_s^{(*)}$, D_{sJ} candidates are constructed, which are subsequently combined with other $D^{(*)}$ candidates into B candidates. We use kinematic variables to disentangle signal and background and selection criteria optimized with simulated events.

In summary, we are considering (D^0, D^+, D^* and D^{*0}) × ($D_s\pi^0$, $D_s^*\pi^0$ and $D_s\gamma$) final states and we select at most one B candidate for each of the twelve final state for each event. Events which are found to be compatible with one of the eight two–body decays $B \to D_s^{(*)}D^{(*)(0)}$ are discarded in the D_{sJ} analysis, but are considered separately in order to obtain a useful control sample (see Section 3.6).

To compute the branching ratios we need to know the total number of $B\bar{B}$ pairs produced, the number of selected events, the reconstruction efficiency, the branching ratios of the intermediate $D^{(*)}$, $D_s^{(*)}$ sub-decays and an estimate of the background.

We take the branching fractions of the intermediate $D^{(*)}$, $D_s^{(*)}$ sub-decays from ref. [24]. The number of $B\bar{B}$ pairs and the integrated luminosity are summarized below.

The number of observed events in data is fitted in the $m(D_{sJ}^{(*)+})$ invariant mass distributions (Section 4.2) subtracting non-peaking background on a statistical basis. These distributions are constructed selecting one B candidate per event for each of the twelve B mode (Section 3.4.4) estimating the efficiencies and the peaking background source, the cross–feed between different signal channels.

This analysis is performed on data recorded by the *BABAR* detector on the $\Upsilon(4S)$ peak between 1999 and 2002. Data taking periods are divided in runs; the data sample corresponds to the runs 1-3. The associated integrated luminosity is $\mathcal{L} \approx 113\ \mathrm{fb}^{-1}$, corresponding to $[122.1 \pm 0.6(stat) \pm 1.3(syst)]$ millions of $B\bar{B}$ events. Simulation studies are performed on generic ($e^+e^- \to q\bar{q}, B\bar{B}$, no $B \to D_{sJ}D^{(*)}$), signal ($e^+e^- \to B\bar{B}, B \to D_{sJ}D^{(*)}$) and background ($e^+e^- \to B\bar{B}, B \to D_s^{(*)}D^{(*)}$) events.

Approximately one hundred million generic decays of each initial state B^+B^- and $B^0\bar{B}^0$, where signal decay modes associated with this analysis are not produced, are mainly used to verify the absence of background from other processes peaking in the signal region (Section 3.5.1).

To estimate the reconstruction efficiency signal decay modes are produced supposing that $D_{sJ}^*(2317)$ and $D_{sJ}(2460)$ decay are a scalar and a vector mesons respectively. The masses and widths used are $m_{D_{s0}} = 2316\,\mathrm{MeV}/c^2$, $\Gamma_{D_{s0}} = 1\,\mathrm{MeV}$ for D_{s0} and $m_{D_{s1}} = 2457\,\mathrm{MeV}/c^2$, $\Gamma_{D_{s1}} =$

1 MeV for D_{s1}. We distinguish different intermediate states, simulating separately modes with the same B and D_{sJ} decay but different D or D_s^+ decay. In total we simulated sixty different signal decay modes, detailed in table A.1.

Two–body decays $B \to D_s^{(*)} D^{(*)}$ are expected to be a major background to the $B \to D_{sJ}^+ \overline{D}^{(*)}$ analysis: the specific selection criteria applied to suppress it is described in Section 3.4.2 and Section 3.5.2). Therefore, samples of 55000–61000 events per $D_s \times D$ decay submode (e.g. $\phi\pi \times K\pi\pi^0$,...) have been simulated. The detailed list of modes is given in table A.2. This sample is also used in a measurement of $B \to D_s^{(*)} D^{(*)}$ branching ratios (Section 3.6), which provides an important cross check of the analysis procedure and the detector model.

3.2 Pre–selection

In this section we will describe the selection of the intermediate particles that will be used to reconstruct the B decay modes.

First of all we do not process all the *BABAR* data but only those that satisfy minimal requirement to be a multi-hadron physics event candidate [52].

- at least three loose selected tracks in fiducial volume $0.41 < \theta < 2.54$;
- the ratio of the second to the zeroth Fox-Wolfram moment (calculated from the selected tracks + neutral) $R2 < 0.5$ (see Section B.1);
- Total energy (charged + neutral) $> 4.5\,\mathrm{GeV}$;
- xy distance (see Section 2.3.1) between primary vertex and measured beam spot $\sqrt{\Delta_x^2 + \Delta_y^2} < 0.5\,\mathrm{cm}$;
- z distance (see Section 2.3.1) between primary vertex and measured beam spot $|\Delta_z| < 6$ cm.

The primary vertex is computed using a fast algorithm that uses only the charged tracks. To compute the total energy, the neutral clusters used are in the angular region $0.41 < \theta < 2.409$ and have an energy greater than 30 MeV. The efficiency of keep $B\bar{B}$ events with this requirements is very high: $\varepsilon_{BB} = 0.954$.

Hadronic events contain a rather large number of tracks and photons: to reduce the combinatorics we use a pre–selection procedure. Only those D and D_s^+ candidates and theirs particles daughters that satisfy the criteria discussed below are actually considered (Section 3.2.2), before combining them with a selected π^0 or γ (Section 3.2.1) to make the final B candidates (Section 3.2.4).

3.2.1 Reconstruction of π^0 and π^0 veto on γ

Reconstructed π^0 candidates are built from pairs of photons with an energy $E(\gamma) > 30\,\mathrm{MeV}$ and a lateral shower shape consistent with the expected pattern of the energy deposit for an electromagnetic shower. This is expressed by requiring $LAT < 0.8$ (see Section B.2). The invariant mass is required to be in the window $115 < m(\gamma\gamma) < 150\,\mathrm{MeV}/c^2$. To improve the π^0 momentum resolution, a mass constrained (see Section 2.4.3) fit is applied to the π^0 used in the D^0, D^{*0}, and B reconstruction.

Single photons are used in the decays $D^{*0} \to D^0\gamma$, $D_s^{*+} \to D_s^+\gamma$, and $B \to D^{(*)} D_s^+ \gamma$. The photons selected have $E(\gamma) > 100\,\mathrm{MeV}$ and $LAT < 0.8$. To reduce the huge combinatorial background from $\pi^0 \to \gamma\gamma$ decays, a π^0 veto is applied: photons should not belong to a π^0 candidate built from two photons with $E(\gamma) > 100\,\mathrm{MeV}$ and $LAT < 0.8$, and having an invariant mass $115 < m(\gamma\gamma) < 150\,\mathrm{MeV}/c^2$.

3.2.2 Reconstruction of the D^0, D^+ and D_s^+ mesons

The decay modes with higher reconstruction efficiency and large branching fraction are chosen to reconstruct intermediate mesons. The first one is mainly affected by the number of charged tracks and photons in the final states. Track reconstruction efficiency is higher than photon reconstruction efficiency, and we discard final states with low product of efficiency and branching fraction ($\varepsilon\mathcal{B}$), as an example $D^0 \to K_S^0\, \pi^+\, \pi^-$, and $D^{*+} \to D^+\pi^0$ where the neutral pion have also rather small energy (see Section 3.2.3). In the D_s^+ decays, the presence of an intermediate particle, like the ϕ in the $D_s^+ \to \phi\pi^+$ decay, can be used to reject the combinations using a mass cut with little efficiency loss. We choose to fully reconstruct D and D_s mesons in the modes reported in table 3.1, with the corresponding branching fractions. The branching fractions for $\phi \to K^+K^-$ and $\bar{K}^{*0} \to K^\pm\pi^\mp$ are $(49.1 \pm 0.6)\%$ and $\sim 66\%$ respectively.

Table 3.1: D, D_s^+ mesons branching fractions [24].

Mode	Branching Fraction (%)
$D^0 \to K^-\pi^+$	3.80 ± 0.09
$D^0 \to K^-\pi^+\pi^0$	13.0 ± 0.8
$D^0 \to K^-\pi^+\pi^+\pi^-$	7.46 ± 0.31
$D^+ \to K^-\pi^+\pi^+$	9.2 ± 0.6
$D_s^+ \to \phi\pi^+ \times \phi \to K^+K^-$	1.77 ± 0.44
$D_s^+ \to K^{*0}K^+) \times K^{*0} \to K^-\pi^+$	2.20 ± 0.60

The selection criteria used at the pre–selection level to reconstruct the D's are summarized in appendix A.2 (Table A.3 for D^0 and D^+ and Table A.4 for D_s). Charged pions are selected between tracks that pass a very loose selection (GTVL, see Section 2.4.3). Charged Kaons are selected between tracks that pass a very loose selection and are required to satisfy the PID for the kaon hypothesis (KMicroNotPion, see Section 2.4.3). The invariant D mass is required to be in a wide window centered at the nominal D mass value [24], varying from $\pm 30\,\mathrm{MeV}$ to $\pm 50\,\mathrm{MeV}$ depending from the decay mode. The $D^0 \to K^-\, \pi^+\, \pi^0$ require a wider window because the energy loss of the photons from π^0 can cause an asymmetric mass distribution with a queue at low values.

For the decays $D_s^+ \to \phi\pi^+$ and $D_s^+ \to \bar{K}^{*0}\, K^+$, the ϕ candidates are reconstructed from K^+K^- pairs with a mass within $\pm 12.5\,\mathrm{MeV}/c^2$ of the nominal ϕ mass; the K^{*0} candidates are built from $K^+\pi^-$ pairs with a mass within $\pm 25\,\mathrm{MeV}/c^2$ of the nominal K^{*0} mass. The invariant D_s^+ mass is required to be in a $\pm 30\,\mathrm{MeV}$ window centered at the nominal D_s^+ mass value [24].

$D_{(s)}$ candidates are built by combining the kaon, pion(s) and π^0 fitted to a common vertex but with no requirement of convergence. This computation is useful to have another handle for the final selection.

3.2.3 Reconstruction of the D^*, D^{*0} and D_s^* mesons

The decay modes used to reconstruct D^*, D^{*0} and D_s^* mesons together with their known branching fractions [24] are summarized in table 3.2.

$D^{*+} \to D^0\pi^+$ are reconstructed by combining the D^0 candidates defined above with a charged track, applying the very loose selection. The mass difference Δm between the masses of D^* and D^0 candidates is required to be within $4.1\,\mathrm{MeV}/c^2$ of its nominal value [24], $5.1\,\mathrm{MeV}/c^2$ for the case in which the D^0 is reconstructed into the channel $D^0 \to K^-\, \pi^+\, \pi^0$.

$D^{*0} \to D^0\pi^0$ decays are reconstructed by combining the D^0 candidates defined above with π^0 candidates built as in 3.2.1. A $p^*(\pi^0) < 450\,\mathrm{MeV}/c$ cut is applied on their momentum in the $\Upsilon(4S)$ frame. The reconstructed $D^{*0} - D^0$ mass difference is required to be $138 < \Delta m < 146\,\mathrm{MeV}/c^2$.

Table 3.2: D^*, D^{*0} and D_s^* mesons branching fractions [24].

Mode	Branching Fraction (%)
$D^{*+} \to D^0\,\pi^+$	67.7 ± 0.5
$D^{*0} \to D^0\pi^0$	61.9 ± 2.9
$D^{*0} \to D^0\gamma$	38.1 ± 2.9
$D_s^* \to D_s\gamma$	94.2 ± 2.5

The D^* pre–selection criteria are listed in table A.5. Decays $D^{*0} \to D^0\gamma$ and $D_s^{*+} \to D_s^+\gamma$ are reconstructed by combining the D^0 or D_s^+ candidates defined above with a π^0 vetoed photon (sec.3.2.1). D^{*0} (D_s^*) candidates are selected if the $D^{*0} - D^0$ ($D_s^{*+} - D_s^+$) mass difference is $112 < \Delta m < 172\,\mathrm{MeV}/c^2$ ($114 < \Delta m < 174\,\mathrm{MeV}/c^2$). The Δm mass difference for the D^*, D^{*0} and D_s^* are reported in Figure 3.4 for data and simulation (see also Section 3.3.1).

3.2.4 Reconstruction of the B meson

The $D^{(*)}$ and $D_s^{(*)}$ candidates, as defined above, and π^0 or γ candidates are combined together reconstructing each one of the final states $D^{(*)}D_s^{(*)}$, $D^{(*)}D_s^{(*)}\pi^0$ and $D^{(*)}D_s\gamma$. Neutral pions are built as described in section 3.2.1 with no momentum or energy requirement. Photons are selected as described in section 3.2.1 with the π^0 veto.

We define two kinematic variables related to the reconstructed B. The *energy substituted mass* (m_{ES}):

$$m_{\mathrm{ES}} = \sqrt{(E^*_{beam})^2 - (p^*_B)^2} \tag{3.1}$$

and the *energy difference* ΔE:

$$\Delta E = E^*_B - E^*_{beam} \tag{3.2}$$

where E^*_{beam} is the beam energy and E^*_B and p^*_B are the energy and momentum of the B in the center of mass of the $\Upsilon(4S)$ frame. These quantities are in good approximation uncorrelated, since the uncertainty on ΔE is dominated by the E^*_B contribution:

$$\sigma(\Delta E) = \sqrt{(\sigma(E^*_B))^2 + (\sigma(E^*_{beam}))^2} \tag{3.3}$$

with the uncertainties $\sigma(E^*_B) \sim 10 - 20\,\mathrm{MeV}$ and $\sigma(E^*_{beam}) \approx 1.5\,\mathrm{MeV}$, while the uncertainty on m_{ES} is dominated by E^*_{beam}:

$$\sigma(m_{\mathrm{ES}}) = \frac{1}{m_{\mathrm{ES}}} \cdot \sqrt{(E^*_{beam}\sigma(E^*_{beam}))^2 + (p^*_B\sigma(p^*_B))^2} \tag{3.4}$$

with $E^*_{beam} \approx 5\,\mathrm{GeV}$, $p^*_B \approx 300\,\mathrm{MeV}$, and the uncertainty $\sigma(p^*_B) \approx 15\,\mathrm{MeV}$.
A correctly reconstructed B meson will have a ΔE around 0 and a m_{ES} that will peak at the B mass. The scatter plot of the two variables is shown in Figure 3.1 while projections are shown in Figure 3.2. The signal for both variables can be modeled with a Gaussian function, while background of the m_{ES} distribution is modeled with an *Argus function* [53]:

$$f\,(m_{ES};A,\xi) = A m_{ES}\sqrt{1 - \frac{4m^2_{ES}}{E^*_{beam}}}\; e^{\xi\left(1 - \frac{4m^2_{ES}}{E^*_{beam}}\right)} \tag{3.5}$$

where the free parameters ξ model the shape of the function and A is a normalization factor.

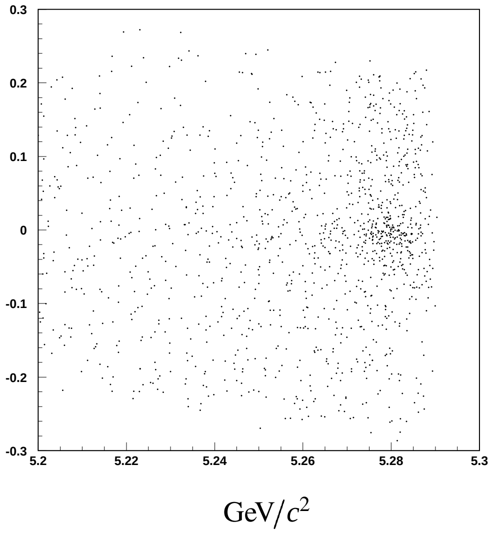

Figure 3.1: Scatter plot of ΔE *vs* $m_{\rm ES}$ *in the pre–selected region. Projections are reported in Figure 3.2. This example is taken from* $B^+ \to D^{*0}D_s^+\gamma$ *mode reconstructed in data.*

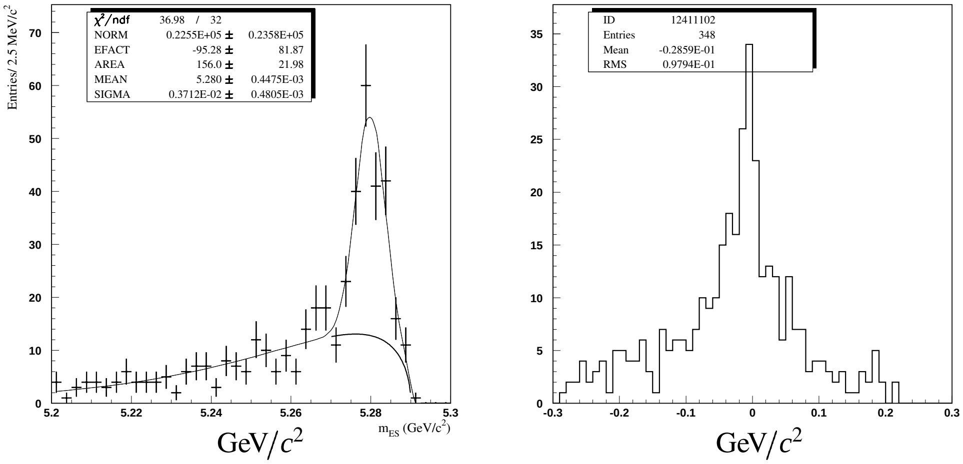

Figure 3.2: Projections of $m_{\rm ES}$ *and* ΔE *variables in the preselection plane. The Argus+Gaussian fit is shown for the* $m_{\rm ES}$ *plot. This example is taken from* $B^+ \to D^{*0}D_s^+\gamma$ *mode reconstructed in data.*

We apply a pre–selection requirement $5.15 < m_{ES} < 5.35\,{\rm GeV}/c^2$ and $|\Delta E| < 300$ MeV. All the B candidates and their daughters components, satisfying these cuts are kept in consideration for further study. As we will see in section 3.4.4, only one B candidate will be chosen for each mode for each event.

3.3 Optimization of D, D_s^+ and D^* final selection

In this section we describe the steps used to improve the significance of the signal yield in each of the decay channels. We define a signal region in the two variables m_{ES} and ΔE (see Section 3.2.4) and look for a peak in the $D_s^{(*)+}\pi^0$ or $D_s^+\gamma$ invariant mass spectra at the D_{sJ} mass.

The resolution in m_{ES} is independent of the decay modes considered and we therefore select B candidates by applying a common selection $5.272 < m_{\mathrm{ES}} < 5.288\,\mathrm{GeV}/c^2$. On the contrary, the ΔE resolution depends on the B final states, as an example it depends on the number of produced gammas. We have studied the ΔE resolution from the signal simulated sample (see Section 3.4.1).

The selection criteria are optimized individually by maximizing the significance ratio:

$$\frac{S}{\sqrt{S+B}} \tag{3.6}$$

the expected signal S is determined from the number of $B\overline{B}$ events (Section 3.1), using the efficiencies extracted from the signal simulation (Section 3.5.3), the already known intermediate branching fraction from [24] and assuming a branching fraction of 10^{-3} for $\mathcal{B}(B \to D_{s0}\overline{D}^{(*)}) \times \mathcal{B}(D_{s0}^+ \to D_s^+\pi^0)$, $\mathcal{B}(B \to D_{s1}^+\overline{D}^{(*)}) \times \mathcal{B}(D_{s1}^+ \to D_s^{*+}\pi^0)$ and $\mathcal{B}(B \to D_{s1}^+\overline{D}^{(*)}) \times \mathcal{B}(D_{s1}^+ \to D_s^+\gamma)$. The background B is determined from the data, by selecting events in the ΔE, m_{ES} signal region and extrapolating the background from two symmetrical, 4σ wide sidebands in $m(D_s^{(*)+}\pi^0)$ or $m(D_s^+\gamma)$ around the D_{sJ} mass.

In Section 3.3.1 we show the mass spectra from inclusive $D_{(s)}^{(*)}$ pre–selected samples and the choice of the cut based on the width of the distributions; in the subsequent sections we define different D^0, D^+, D_s^+ selection levels, based on kaon and pion particle identification (see Section 2.3.2), and vertexing, starting from the loosest level and adding new cuts to the tighter level.

To establish the best combination of cuts, different combinations are tested on the pre–selected sample sequentially, varying one cut at a time and the final significance is then computed for each of the decay modes.

3.3.1 Resolutions

The D and D_s^+ invariant mass distributions where studied from the inclusive mass spectra of all the D's present in the events after the pre–selection. The same procedure was applied to the simulated signal events, to compare the D reconstruction in the data and in the simulation. The resulting spectra are shown in Figure 3.3(a) for the data and Figure 3.3(b) for the simulation. The average reconstructed masses and mass resolutions are given in Table A.6. The resolution σ, found in the data, is 11.8 MeV/c^2 for $D^0 \to K^-\ \pi^+\ \pi^0$ decays and varies from 5.3 to 6.3 MeV/c^2 for the other decay modes.

We retained D and D_s^+ candidates within a mass window around the average reconstructed mass. To choose the window width we use an optimization procedure. We tryied all the combinations ± 2, ± 2.5 and ± 3 σ mass cut for D, D_s^+, then evaluate the variation of significance (eq. 3.6) for each decay mode. The combinations that maximize the significance is retained. The same procedure will be used for ΔE, (Section 3.4.1). We set at ± 3 σ around the average reconstructed D and D_s^+ masses (Table A.6) the cut for the cleanest modes ($K^-\ \pi^+$,$K^-\ \pi^+\ \pi^+$, $\phi\pi$), while for modes with more background ($K^-\ \pi^+\ \pi^0$, $K^-\ \pi^+\ \pi^-\ \pi^+$, $K^{*0}\ K^+$) the cut is set at ± 2.5 σ.

The D^* and D_s^* reconstruction has been studied in the same way and plots of the $D^* - D$ mass are shown in Figure 3.4 . The corresponding resolutions are given in Table A.7. From these results the following cuts are applied in the final D^* selection:

- $D^{*+} \to D^0\pi^+$: $143.4 < \Delta m < 145.4\,\mathrm{MeV}/c^2$

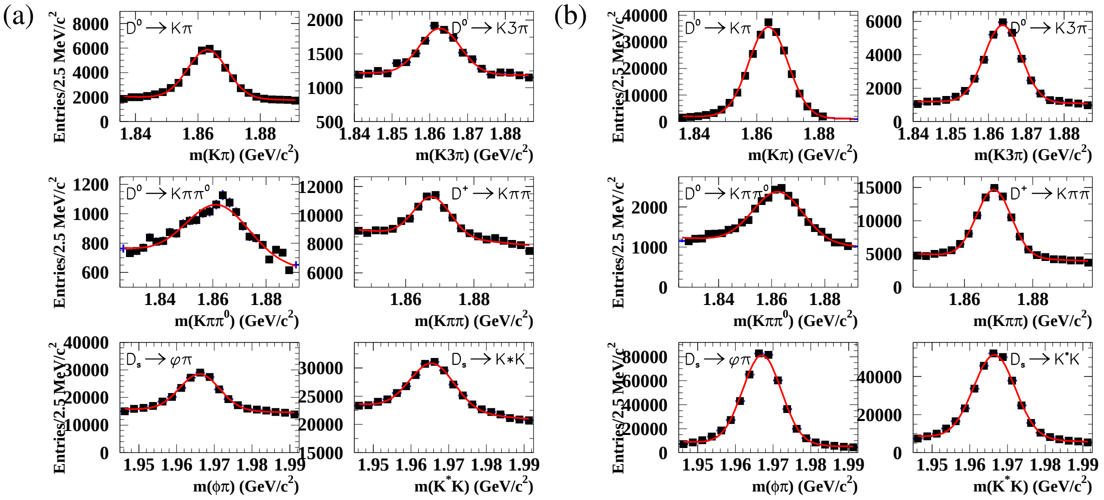

Figure 3.3: D mass fits for (a) the data and (b) the simulated signal. For D_s and some D_0 modes, the simulation is a bit too optimistic in the reproduction of the background.

- $D^{*0} \to D^0\pi^0$: $140.0 < \Delta m < 144.0\,\mathrm{MeV}/c^2$
- $D^{*0} \to D^0\gamma$: $132.0 < \Delta m < 152.0\,\mathrm{MeV}/c^2$
- $D_s^* \to D_s\gamma$: $133.8 < \Delta m < 153.8\,\mathrm{MeV}/c^2$

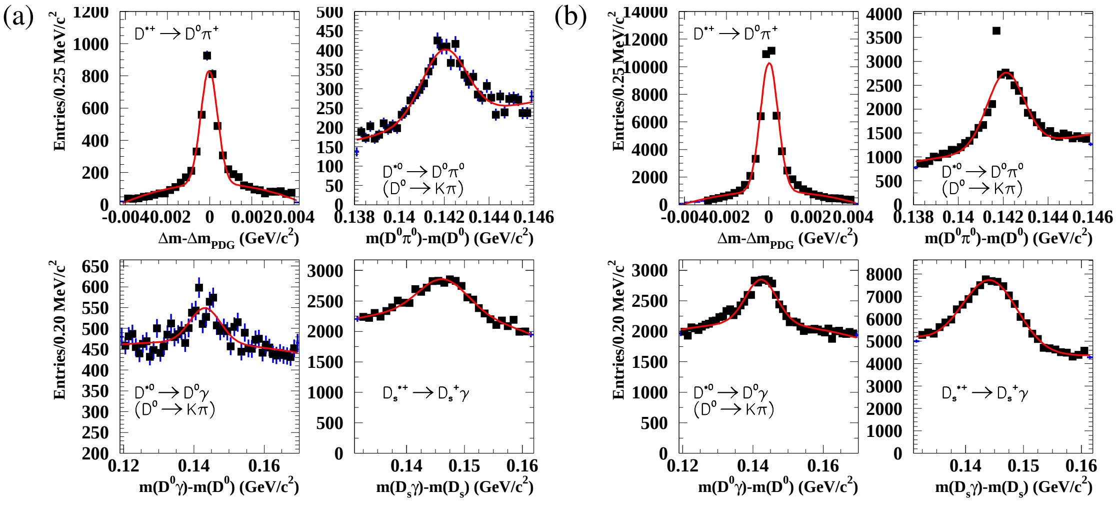

Figure 3.4: D^* mass fits for (a) the data and (b) the simulated signal

3.3.2 $D^0 \to K^- \pi^+$ selection

From this section trough Section 3.3.6 we look for tecniques to suppress background in the preselected sample. Some of them are common to all the subdecays considered here. Kaon PID requirements (see Section 2.3.2) and vertex probability cut are useful to suppress combinatorial background but not always this effect is balanced by the loose in efficiency. The cleanest modes such as $D^0 \to K^- \pi^+$, that have few tracks in the final state and lower combinatorial background, do not require a tight kaon PID cut, as we will see.

We try each combination of cuts for D^0, D^+, and D_s^+, then we compute the significance as in eq. 3.6 for each subdecay mode. The combination of cuts that give the higher value of significance for each mode is considered as the optimal one.

To improve the $D^0 \to K^- \pi^+$ selection we tested three sets of selection criteria:

1. requiring the $K^\pm$ to satisfy the KMicroNotPion PID criteria (as defined in Section 2.3.2) and have a momentum $p(K) > 250\,\mathrm{MeV}$
2. adding a tight PID criteria to the $K^\pm$ (KMicroTight);
3. requiring that the $K\pi$ vertex fit has converged and that the χ^2 vertex fit probability satisfies $prob(\chi^2) > 10^{-3}$.

For a majority of decay modes, the best significance ratio is obtained using the loosest of these cuts, i.e. KMicroNotPion PID criteria and $p(K) > 250\,\mathrm{MeV}$. Therefore, this cut is used in the final analysis for all the B decay modes studied here.

3.3.3 $D^0 \to K^- \pi^+ \pi^0$ selection

The $D^0 \to K^- \pi^+ \pi^0$ decays occur mainly trough the resonances $\bar{K}^*(892)^0$, $K^*(892)^-$, or $\rho(770)^+$. We use these resonances to reduce the background in this decay mode, calculating the decay probability in the $(m^2_{K^-\pi^+}; m^2_{K^-\pi^0})$ phase space. Indicating with i, j, and k the three particles K^-, π^0, and π^+ we define in the $k-i$ center of mass system the angle θ^*_{ij} as the angle between the momenta $\vec{p}^*_i$ and $\vec{p}_j$. For each possible resonance R the decay amplitude $\mathcal{A}_R$ is:

$$\mathcal{A}_R = \frac{C_R e^{\frac{i\phi_R \pi}{180}} \sqrt{\frac{\Gamma_R}{2\pi}} \cos\theta^*_{jk}}{m_R - m_{ij} - i\frac{\Gamma}{2}} \tag{3.7}$$

i and j are the indexes of the particles that make the resonance R; Γ_R and m_R are the width and mass of R from [24], and C_R and ϕ_R are the amplitude and the phase of the resonance in the decay $D^0 \to K^- \pi^+ \pi^0$. These parameters were determined in the E691 experiment [54] (see Table 3.3).

Table 3.3: Parameters of intermediate resonances in the $D^0 \to K^- \pi^+ \pi^0$ decay.

Resonance	m_R (MeV/c^2)	Γ_R (MeV/c^2)	C_R	ϕ_R
$\bar{K}^*(892)^0 \to K^-\pi^+$	896.1	50.7	3.19	$-13°$
$K^*(892)^- \to K^-\pi^0$	891.66	50.8	2.96	68°
$\rho(770)^+ \to \pi^+\pi^0$	766.5	150.2	8.56	40°

We take the amplitude of the non-resonant part as reference with $\mathcal{A}_0 = 1$. Then we compute the probability density:

$$\mathcal{P}_{D^0 \to K^-\pi^+\pi^0}\left(m\left(K^-\pi^+\right)^2, m\left(K^-\pi^0\right)^2\right) = \left|\mathcal{A}_0 + \mathcal{A}_{\bar{K}^{*0}} + \mathcal{A}_{K^{*-}} + \mathcal{A}_{\rho^+}\right|^2 \tag{3.8}$$

This probability, convoluted with two gaussian resolution functions, is used to compute the “Dalitz Weight” (Dw). A simulation of $D^0 \to K^- \pi^+ \pi^0$ events is shown in Figure 3.5, on the left without any requirements, on the right with the requirement $Dw > 10$. This requirement raises the purity from 3.2% to 4.6% while keeping the efficiency at about 90%.

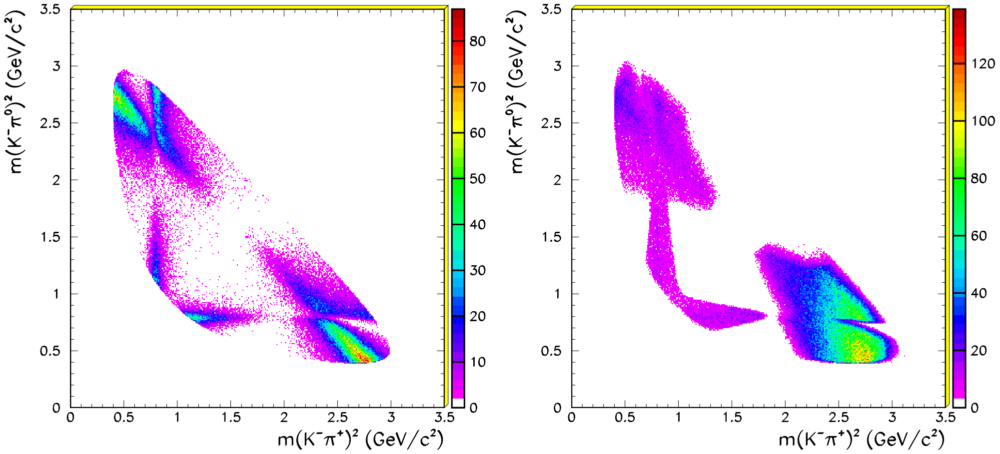

Figure 3.5: Dalitz plot for $D^0 \to K^- \pi^+ \pi^0$ simulated events: signal (left) and after the requirement $Dw > 10$ (right).

The following set of cuts have been tested for the selection of $D^0 \to K^- \pi^+ \pi^0$:

1. requiring the K^- to satisfy the KMicroNotPion PID criteria and have a momentum $p(K) > 250\,\text{MeV}$. Require also the π^0 energy to satisfy $E(\pi^0) > 200\,\text{MeV}$;
2. requiring tight PID criteria (KMicroTight) for the K^-;
3. cut on the dalitz weight $Dw > 10$;
4. requiring both photons from the π^0 to have an energy $E(\gamma) > 50\,\text{MeV}$;
5. requiring that the $K\pi\pi^0$ vertex fit has converged and that the χ^2 vertex probability satisfies $prob(\chi^2) > 10^{-3}$.

As in Section 3.3.2, we establish that for modes $B \to D_{sJ}D^{*+}$ ($D^{*+} \to D^0\pi^+$) the best cut is the loosest one (i.e. KMicroNotPion PID criteria and $p(K) > 250\,\text{MeV}$). For all the other modes, the selection with KMicroTight and $Dw > 10$ is chosen.

3.3.4 $D^0 \to K^- \pi^+ \pi^- \pi^+$ selection

Since the large number of tracks the vertex cut is very powerful to remove background. The effect of the vertex cut is shown in Figure A.1. The following set of cuts have been tested for the selection of $D^0 \to K^- \pi^+ \pi^- \pi^+$:

1. requiring the K^- to satisfy the KMicroNotPion PID criteria, have a momentum $p(K) > 250\,\text{MeV}$;
2. requiring tight PID criteria (KMicroTight) for the K^-;
3. requiring that the $K\pi\pi\pi$ vertex fit has converged and that the vertex χ^2 probability satisfies $prob(\chi^2) > 10^{-3}$;

4. requiring that all the three π tracks satisfy the GoodTracksLoose selection criteria.

As in Section 3.3.2 we establish that for modes $B \to D_{sJ} D^{*+}$ ($D^{*+} \to D^0 \pi^+$) the best cut is found to be the loosest one (i.e. KMicroNotPion PID criteria and $p(K) > 250\,\text{MeV}$). For all the other modes, the selection with KMicroTight and $p(K) > 250\,\text{MeV}$ and $prob(\chi^2) > 10^{-3}$ is chosen.

3.3.5 $D^+ \to K^- \pi^+ \pi^+$ selection

The following set of cuts have been tested for the selection of $D^+ \to K^- \pi^+ \pi^+$:

1. requiring the K^- to satisfy the KMicroNotPion PID criteria and have a momentum $p(K) > 250\,\text{MeV}$;
2. requiring tight PID criteria (KMicroTight) for the K^-;
3. requiring that the $K\pi\pi$ vertex fit has converged and that the χ^2 vertex probability satisfies $prob(\chi^2) > 10^{-3}$.

As in Section 3.3.2 we establish that the loosest selection, i.e. KMicroNotPion PID criteria and $p(K) > 250\,\text{MeV}$, is found to give the maximum significance and is therefore chosen.

3.3.6 $D_s^+ \to \phi\pi^+$ and $D_s^+ \to \bar{K}^{*0} K^+$ selection

The two particles ϕ and K^* have $J^P = 1^-$. They are recontructed in their decays $\phi \to K^+ K^-$ and $K^* \to K^- \pi^+$. Inclusive invariant mass distributions of the two resonances in our data are reproduced in Figure 3.6.

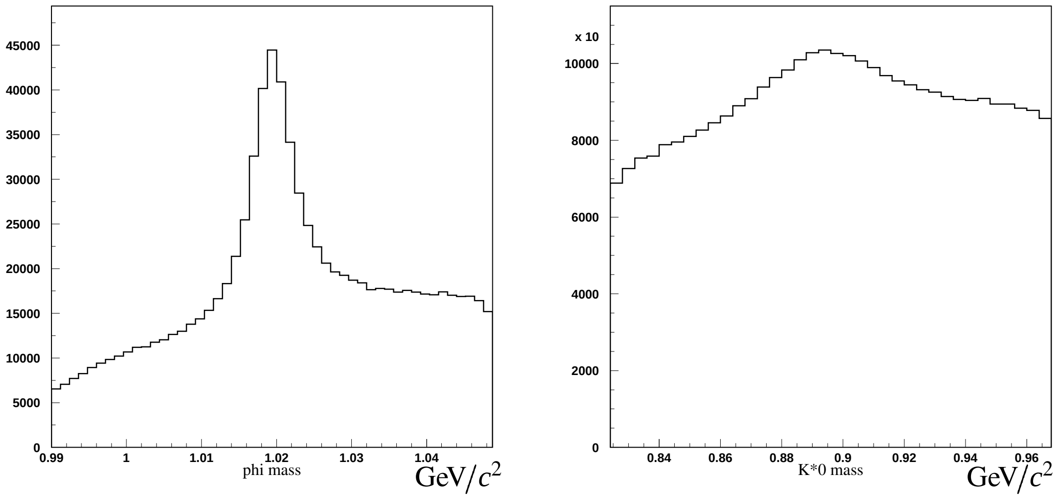

Figure 3.6: Inclusive invariant mass distributions of the ϕ candidates (left) and of the K^* candidates (right), in data events.

The decays $D_s^+ \to \phi\pi^+$ and $D_s^+ \to \bar{K}^{*0} K^+$ are of the type $0^- \to 1^- 0^-$: as a result the ϕ and the K^* are polarized. Defining a helicity angle as in Section 2.4.1, it is possible to separate signal from background using the two different helicity-angle distribution shapes. Background should not show any polarization and should have a flat helicity angle distribution. In Figure 3.7 and

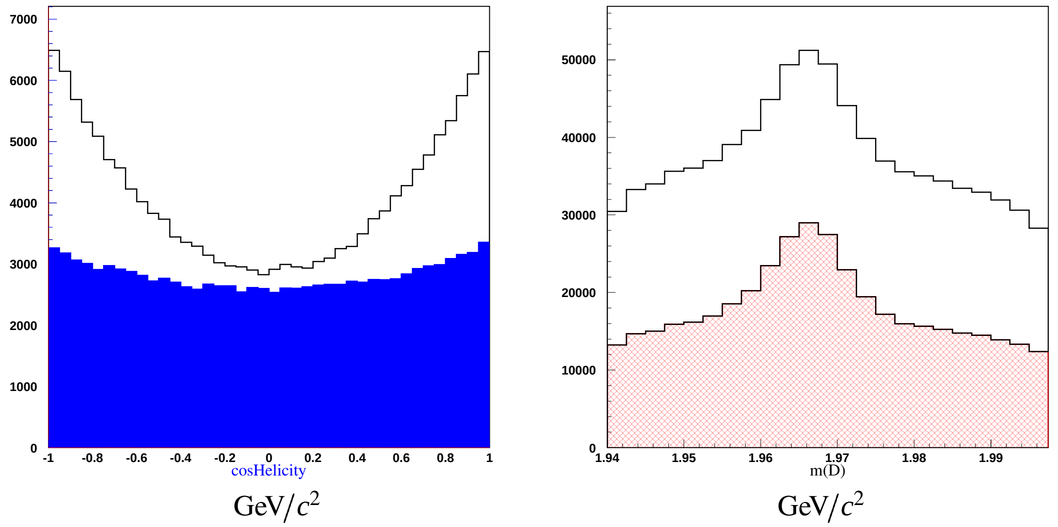

Figure 3.7: (left) Helicity angle distributions for $D_s^+ \to \phi\pi^+$ candidates, with $1.955 < m < 1.977\,\mathrm{GeV}/c^2$; the shaded histogram shows the same distribution from background events with the complementary selection for $m_{D_s^+}$; (right) invariant mass distribution for $D_s^+ \to \phi\pi^+$ candidates; the shaded area corresponds to the events after requiring $|cos(\theta_h)| > 0.3$.

Figure 3.8 are reported, on the left, the helicity angle distributions for ϕ and K^* candidates that come from D_s^+ candidate that have $1.955 < m < 1.977\,\mathrm{GeV}/c^2$. The shaded histogram shows the same distribution from background events with the complementary selection for $m_{D_s^+}$. The effect on the D_s^+ mass distribution of a $|cos(\theta_h)| > 0.3$ requirement is shown on the right. The following set of cuts have been tested for the selection of $D_s^+ \to \phi\pi^+$ and $D_s^+ \to \overline{K}^{*0}\, K^+$:

1. using an invariant mass window on the ϕ (K^*) at $1005 < m(K^+K^-) < 1035\,\mathrm{MeV}/c^2$ ($821 < m(K^-\pi^+) < 971\,\mathrm{MeV}/c^2$);
2. requiring that the helicity angle satisfies $|cos(\theta_h)| > 0.3$;
3. requiring that at least one K satisfies the KMicroTight criteria;
4. requiring that the $\phi\pi$ or K^*K vertex fit has converged and that the χ^2 vertex probability satisfies $prob(\chi^2) > 10^{-3}$;
5. requiring that both K^+ and K^- satisfy the KMicroTight criteria.

The optimal selection depends not only on the D_s^+ decay but also on the B mode considered. The selection choices after the optimization are summarized in table A.9.

3.3.7 Selection summary

A short summary of the D, D_s and D^* selection criteria is provided in Tables A.8, A.9, and A.10.

3.4 B final selection

In this section we will describe the final selection of B candidates: we define a B signal region in (m_{ES},ΔE) plane (Section 3.4.1); we introduce a veto on the two-body $B \to D_s^{(*)}D^{(*)}$ decays

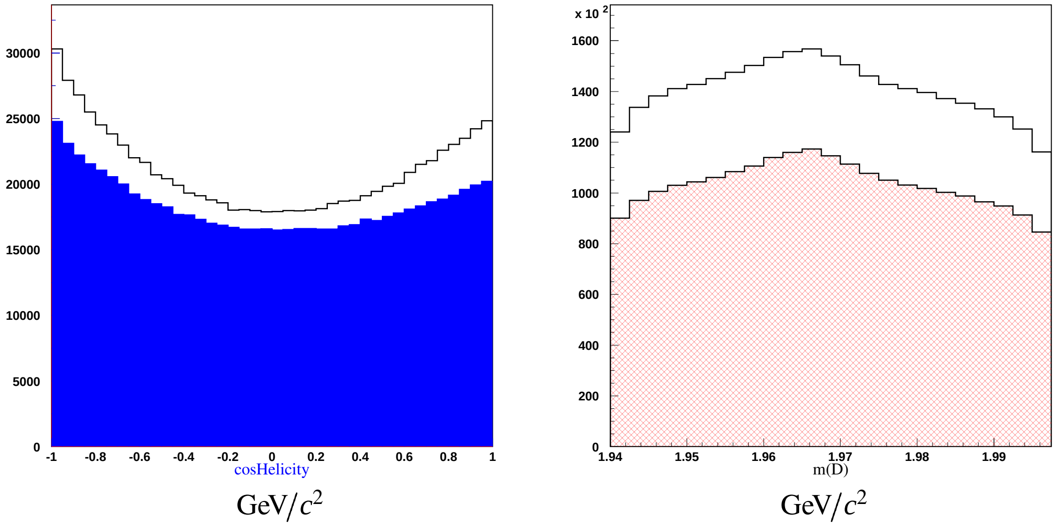

Figure 3.8: (left) Helicity angle distributions for $D_s^+ \to \overline{K}^{*0}\ K^+$ candidates, with $1.955 < m < 1.977\,\mathrm{GeV}/c^2$; the shaded histogram shows the same distribution from background events with the complementary selection for $m_{D_s^+}$; (right) invariant mass distribution for $D_s^+ \to \overline{K}^{*0}\ K^+$ candidates; the shaded area corresponds to the events after requiring $|cos(\theta_h)| > 0.3$.

(Section 3.4.2), and a kinematic cut on the $D^*\pi^0$, $D\pi^0$, or $D\gamma$ invariant mass (Section 3.4.3); we study the multiplicity of B candidates in the signal region after applying all the cuts (Section 3.4.4). We then develop a method to select only one B candidate per final state per selected event. Finally, we present the yields results (Section 3.4.5).

3.4.1 ΔE resolution and signal region

As explained in sec 3.3, the m_{ES} signal region is independent of the decay modes considered and we define it as:

$$5.272 < m_{\mathrm{ES}} < 5.288\,\mathrm{GeV}/c^2. \tag{3.9}$$

The ΔE resolution instead depends on the B final state. Using signal simulated events, we obtain the ΔE spectra in Figure 3.9. The selected candidates have $5.272 < m_{\mathrm{ES}} < 5.288\,\mathrm{GeV}/c^2$ and a $D_s^{(*)+}\pi^0$ or $D_s^+\gamma$ mass in the expected D_{sJ} signal invariant mass region. In this plot, we separate the $D_s^+\overline{D}^{(*)}\pi^0$ final states (upper plot), the $D_s^{*+}\overline{D}^{(*)}\pi^0$ final states (middle plot) and the $D_s^+\overline{D}^{(*)}\gamma$ final states (bottom plots). An asymmetry in the ΔE distribution of the $B \to D_{s1}^+\overline{D}^{(*)}$ ($D_{s1} \to D_s^+\gamma$) events is visible. This can happen if part of the electromagnetic shower is not completely contained in the calorimeter. This appear as an excess at low values in the ΔE distribution. In the $D_s^{(*)+}\pi^0$ final states the mass-constrained fit applied to the π^0 allow a much better energy resolution and no tail in ΔE. A shift of about $\Delta E_0 = -4\,\mathrm{MeV}$ (Table 3.4) is also observed on the ΔE central values.

To define the ΔE signal region we conducted an optimization study as in Section 3.3.1. We computed the significance retaining events in the region $|\Delta E - \Delta E_0| < n\sigma_{\Delta E}$ where $n = 2.0, 2.5, 3.0$. We establish that a 2σ cut on ΔE gives the best significance ratio for most of the modes. Therefore, in all the following the ΔE signal region is defined to be:

$$|\Delta E - \Delta E_0| < 2\sigma_{\Delta E}. \tag{3.10}$$

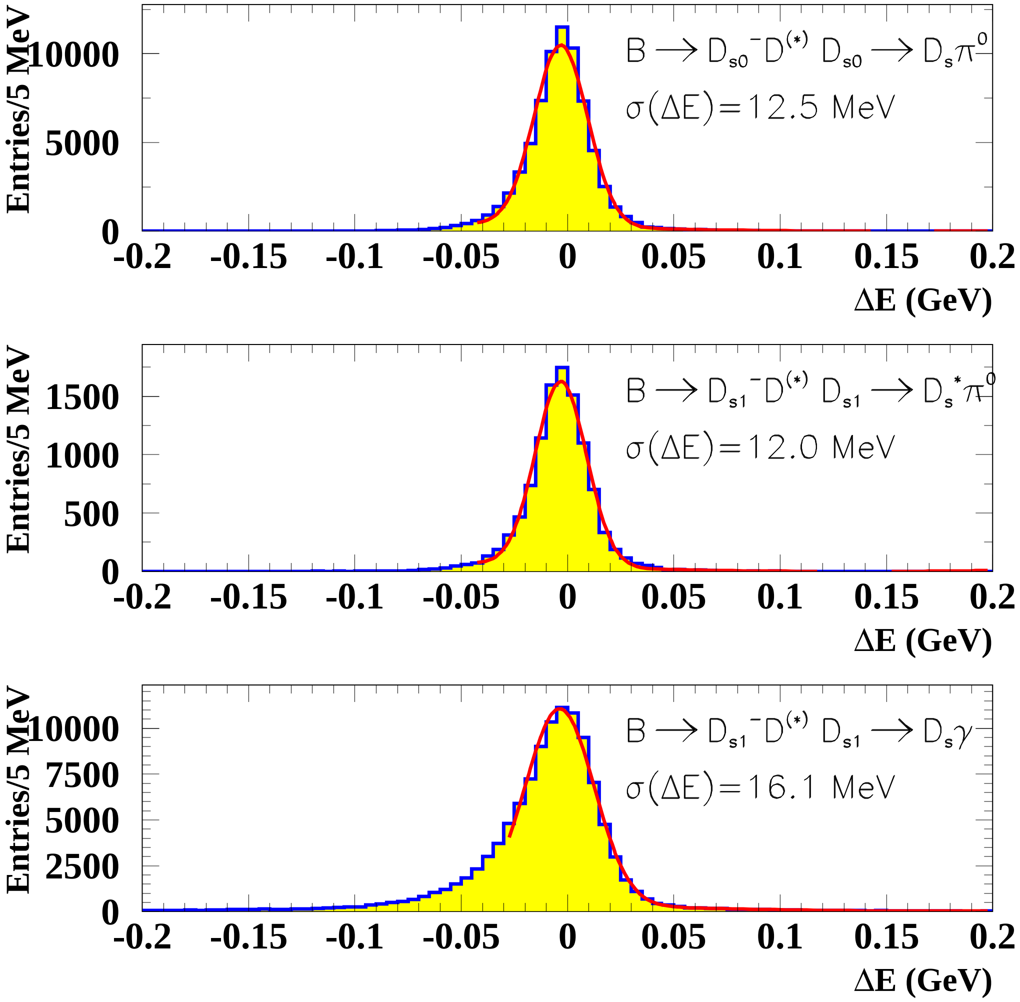

Figure 3.9: ΔE resolution for the simulated signal: from top to bottom, events with $D_{sJ}^{*}(2317)^{+} \to D_s^{+}\pi^0$, $D_{sJ}(2460)^{+} \to D_s^{*+}\pi^0$, and $D_{sJ}(2460)^{+} \to D_s^{+}\gamma$.

In Figure 3.10, we show the reconstructed $D_s^{+}\pi^0$, $D_s^{*+}\pi^0$, $D_s^{+}\gamma$ mass spectra for $B \to D_{sJ}D^{(*)}$ signal simulated events lying in the (m_{ES},ΔE) B signal region defined previously; the final selection criteria have been applied and the submodes with the same $D_{sJ}^{(*)+}$ decay are summed. The invariant mass resolutions σ_m predicted by the simulation are about $8\,\mathrm{MeV}/c^2$ for $D_{s0}^{+} \to D_s^{+}\pi^0$ and $D_{s1}^{+} \to D_s^{*+}\pi^0$; they are about $13\,\mathrm{MeV}/c^2$ for $D_{s1}^{+} \to D_s^{+}\gamma$ (Table 3.4). As already seen in ΔE distributions the resolutions are better for $D_s^{+}\pi^0$, $D_s^{*+}\pi^0$ than for $D_s^{+}\gamma$.

Anticipating our results, from the fits performed on the data (Table 3.6) the values used for defining the ΔE signal region in the data are ΔE_0=-5 MeV, $\sigma_{\Delta E} = 16$ MeV for the π^0 final states and $\sigma_{\Delta E} = 20$ MeV for the γ final states. The uncertainties on these numbers, about 3 MeV, are accounted for in the systematics errors.

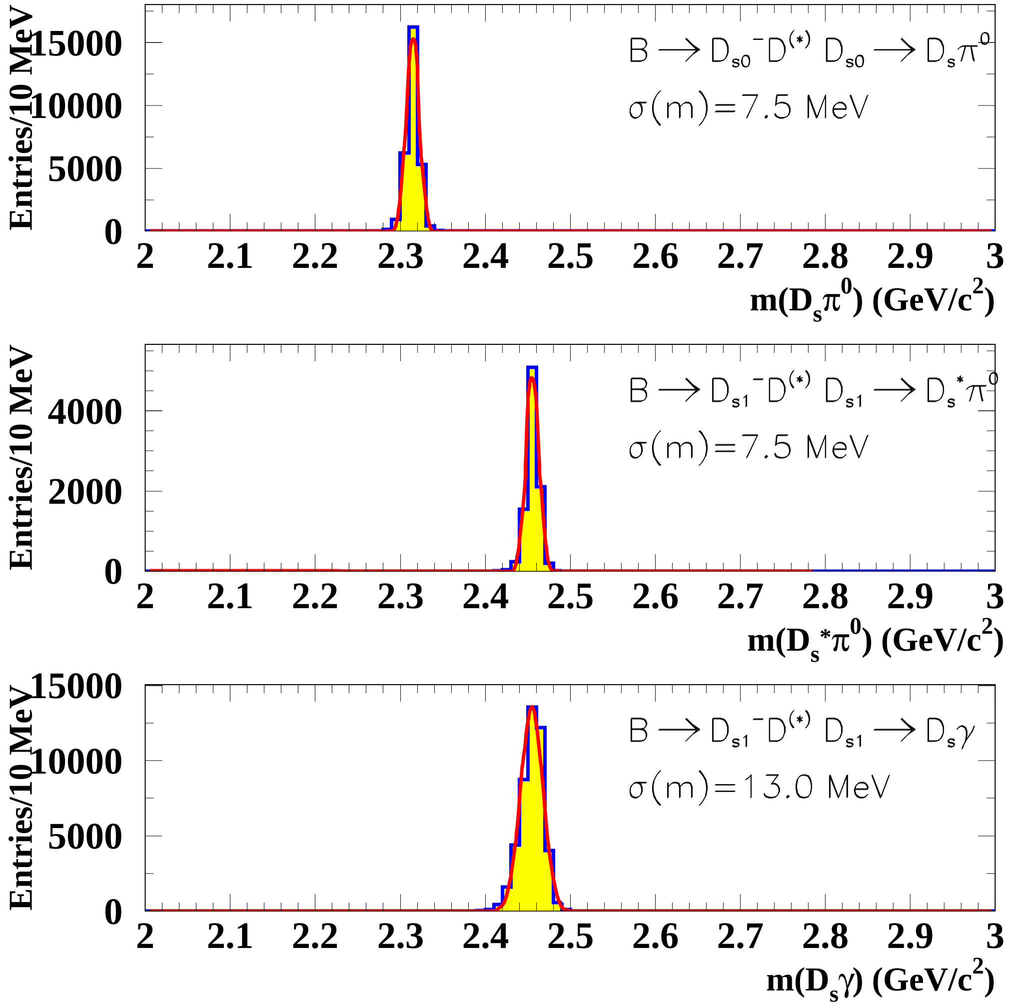

Figure 3.10: $m(D_{sJ})$ resolution for the simulated signal: from top to bottom, events with $D^*_{sJ}(2317)^+ \to D_s^+\pi^0$, $D_{sJ}(2460)^+ \to D_s^{*+}\pi^0$, and $D_{sJ}(2460)^+ \to D_s^+\gamma$.

3.4.2 Rejection of $B \to D_s^{(*)}D^{(*)}$ decays

Two body decays $B \to D_s^{(*)}D^{(*)}$, have a branching fraction of $(4.9 \pm 1.2\%)$ average of B^0, B^+ decays [24]. When associated with a random γ or π^0, they can form a significant combinatorial background to the $D_s^{(*)+}D^{(*)}\gamma$ and $D_s^{(*)+}D^{(*)}\pi^0$ final states from $B \to D_{sJ}D^{(*)}$. To fight this background a veto is applied on the two body decays $B \to D_s^{(*)}D^{(*)}$: these decays are reconstructed using exactly the same D, D_s and D^* selection as in the D_{SJ} analysis. If a $B \to D_s^{(*)}D^{(*)}$ candidate with $m_{\text{ES}} > 5.27\,\text{GeV}/c^2$ and $|\Delta E - \Delta E_0| < 20\,\text{MeV}$ is found in the event, then this event is rejected in the $B \to D_{sJ}D^{(*)}$ analysis. The effect of this selection can be seen in Figure 3.11 for signal simulation and Figure 3.12 for data. The effect on the simulated control sample $B \to D_s^{(*)}D^{(*)}$ is discussed in Section 3.5.2. As one can see in Figure 3.11, the efficiency loss on signal events introduced by this selection is negligible.

Table 3.4: ΔE and $m(D_{sJ})$ resolutions for simulated signal, from a single gaussian fit to the spectra of Figs. 3.9, 3.10

mode	$\langle\Delta E\rangle$ (MeV)	$\sigma_{\Delta E}$	$m(D_{sJ})$ (MeV/c^2)	σ_m
$B \to D_{s0}^+\overline{D}^{(*)}$ $(D_{s0}^+ \to D_s\pi^0)$	-3.1	12.6	2314.5	7.5
$B \to D_{s1}^+\overline{D}^{(*)}$ $(D_{s1} \to D_s^{*+}\pi^0)$	-3.1	12.1	2455.7	7.5
$B \to D_{s1}^+\overline{D}^{(*)}$ $(D_{s1} \to D_s^+\gamma$	-3.6	16.1	2455.8	13.0

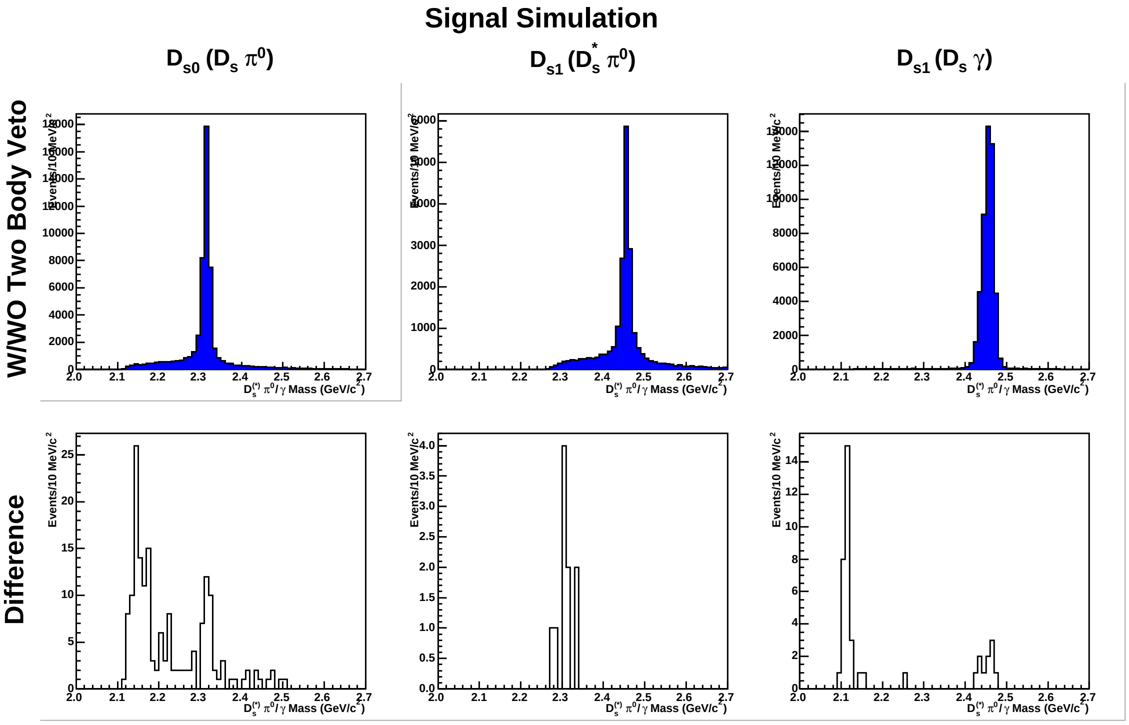

Figure 3.11: Effect of $B \to D_s^{(*)}D^{(*)}$ veto on signal simulation. The top row of plots shows D_{sJ} mass distributions with (shaded histogram) and without the veto. The effect is negligible on this scale. The bottom row shows the $D_s^{(*)}\pi^0/\gamma$ mass spectra of the vetoed events.

3.4.3 Kinematic $D^{(*)}$ π^0/γ selection

We studied a selection both on the $\overline{D}^{(*)}\pi^0$, $\overline{D}^*\gamma$ masses and on the π^0 or γ momentum to improve the separation of the signal from the combinatorial background. Figure 3.13 shows the $D^-\pi^0$ and $D^-\gamma$ mass spectra for combinatorial background events selected in the data from the ΔE sidebands, and for simulated signal $B \to D_{sJ}^+D^-$ events. A clear difference is observed in these mass spectra between the data and the combinatorial background. Other $B \to D_{sJ}^+\overline{D}^{(*)}$decays involving D^0, D^{*+} and D^{*0} show similar spectra. Details on the optimization of this selection are shown in Appendix A.3 where the fractions of selected events are shown, both for the signal and for the background, separately for each of the twelve final states.

The best separating power is obtained, for each of the modes, by a cut $m(\overline{D}\pi^0,\gamma) > 2.3\,\mathrm{GeV}/c^2$ for modes involving D's and $m(\overline{D}^*\pi^0,\gamma) > 2.4\,\mathrm{GeV}/c^2$ for modes involving D^*. This selection was

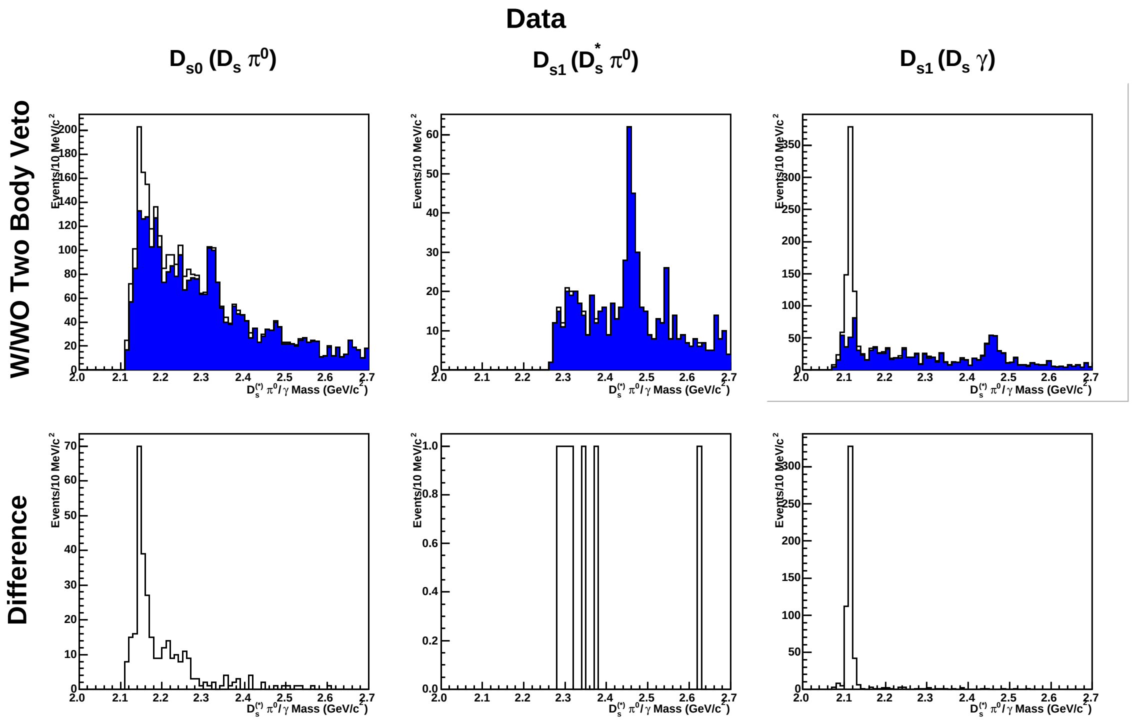

Figure 3.12: Effect of $B \to D_s^{(*)} D^{(*)}$ veto on data. The top row of plots shows D_{sJ} mass distributions with (blue) and without the veto. The bottom row shows the $D_s^{(*)}\pi^0/\gamma$ mass spectra of events vetoed.

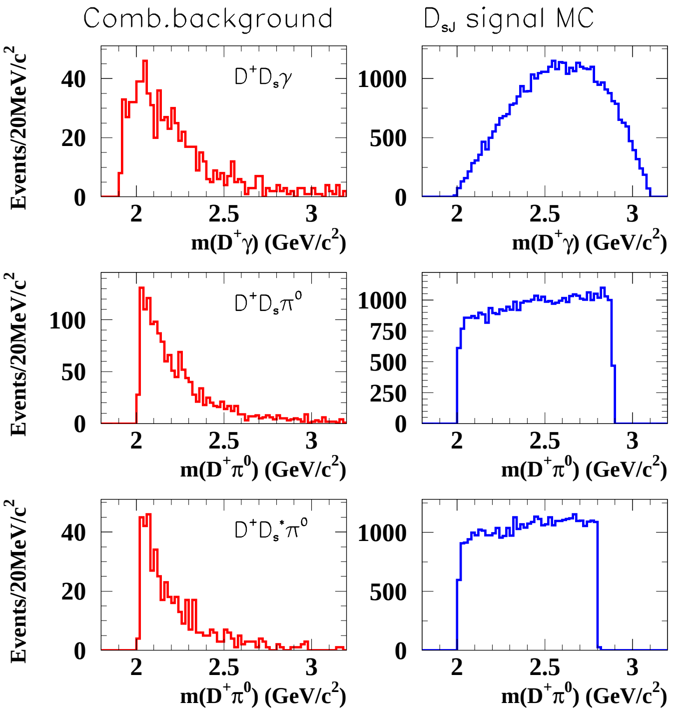

Figure 3.13: $D^-\gamma$ or $D^-\pi^0$ mass spectra for combinatorial background in the data, selected from the ΔE sidebands (left column), and for simulated signal events (left column) $B \to D_{s1}^+ D^-$, $D_{s1}^+ \to D_s^+\gamma$ (top), $B \to D_{s0}^+ D^-$, $D_{s0}^+ \to D_s^+\pi^0$ (middle) and $B \to D_{s1}^+ \overline{D}^-$, $D_{s1}^+ \to D_s^{*+}\pi^0$ (bottom)

adopted in all the results presented below, unless explicitly stated. We checked that for all the twelve modes, this selection improves the significance ratio.

A cut on the γ or π^0 momentum was also found to give a good separating power between signal and background, but it is slightly less efficient and is correlated with the mass cut. Therefore, we decided not use it in our analysis.

3.4.4 Multiplicity studies

Fof final states with π^0 and γ a rather large number of B candidates is found in the signal ($m_{\rm ES}$, ΔE) region in the selected events. This is due mostly to the large combinatorial backgrounds. We define the number of these B candidates per each submode as the multiplicity per selected event. We show in Figure 3.14 the multiplicity distributions for data and simulation summed on the submodes. To reduce the multiplicity, we studied algorithms to select either only one candidate per B mode per event or only one single B candidate per event. To select the best B candidate, we tested three different criteria:

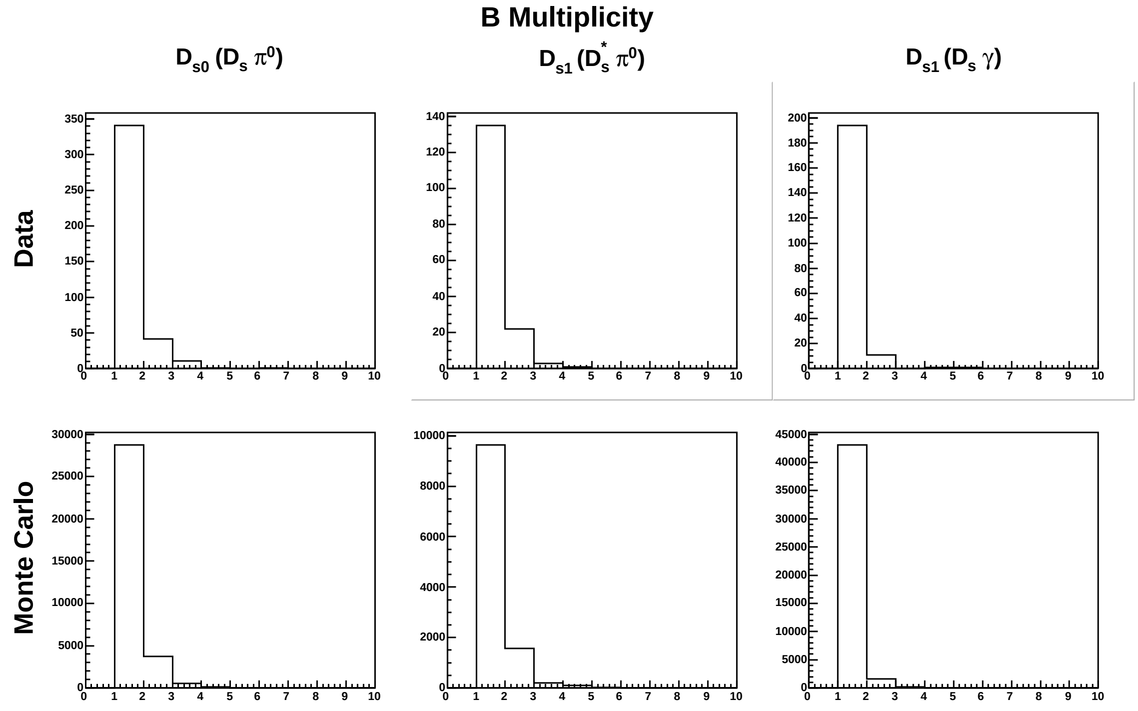

Figure 3.14: Multiplicity distributions for data and simulation. The x-axis is number of candidates for each submode per event after all selection criteria have been applied (except for selecting best candidate per sub–mode). Distributions for the sub–modes have been summed for clarity.

- ΔE: if multiple candidates are present, only the B candidate with the smallest $|\Delta E - \Delta E_0|$ is selected.
- m_{ES}: if multiple candidates are present, only the B candidate with the smallest $|m_{\rm ES} - m_{\rm ES0}|$, with $m_{\rm ES0} = 5.279\,{\rm GeV}/c^2$, is selected.
- χ^2: a χ^2, based on the D, D_s and D^* masses differences vs their nominal reconstructed masses divided by the resolution, is built. If multiple candidates are present, only the B candidate with the smallest χ^2 is selected.

Table 3.5: Efficiency and significance computed for different selection criteria of the B candidate. These values are obtained after applying all the selection requirements, differing only for the final candidate choice. The mode considered is $B^0 \to D^- D_{s1}^+$ $(D_{s1}^+ \to D_s^+\gamma, D^+ \to K^- \pi^+ \pi^+, D_s^+ \to \phi\pi^+)$.

	1 candidate/event			1 candidate/B mode		
	χ^2	$m_{\rm ES}$	ΔE	χ^2	$m_{\rm ES}$	ΔE
efficiency (%)	3.12	4.70	5.35	5.36	6.38	6.62
significance	1.89	2.40	2.58	2.59	2.85	2.91

From a study on simulated data we found that selecting one candidate per mode based on the smallest $|\Delta E - \Delta E_0|$ is the most efficient (see Table 3.5). Therefore it has been chosen to fill the histograms of $m(D_s^{(*)}\pi^0)$, $m(D_s\gamma)$ spectra, from which we extract the $B \to D_{sJ}D^{(*)}$ branching fractions. Of course this criterion is biasing the ΔE spectra of the selected events and it will therefore not be used either when presenting the ΔE spectra of the selected candidates or when searching for resonant backgrounds in the ΔE sidebands. Without this selection and taking all candidates, the final multiplicity (number of D_{sJ} fitted from the $D_s^{(*)}\pi^0$ or D_s^γ mass spectra) is 1.1–1.2 candidates per selected event for modes $D_s\gamma$ and 1.2–1.4 candidates per selected event for $D_s^*\pi^0$ modes.

3.4.5 Evidence for signal in the data

Before proceeding with the extraction of branching ratios, we sum all the modes with the same D_{sJ} decay channel and look at the kinematic variables ΔE, $m_{\rm ES}$ and at the $D_s\pi^0, D_s^*\pi^0, D_s\gamma$ invariant mass distributions. We expect to see the signature of $B \to D_{sJ}D^{(*)}$ decays in the ΔE and $m_{\rm ES}$ plots and $D_{sJ}^{(*)+}$ signal peaks in invariant mass plots. We will use these distributions to estimate the resolution of ΔE and $m(D_{sJ}^{(*)+})$ in data and also as a cross-check: the signal yields obtained fitting the kinematic variables ΔE or $m_{\rm ES}$ or $m(D_{sJ}^{(*)+})$ should be the same within errors. Since we need the ΔE variable to choose one B candidate per mode, for this cross-check we use distributions without this requirement.

We already defined in the ΔE vs $m_{\rm ES}$ plane the B signal region: $5.272 < m_{\rm ES} < 5.288\,{\rm GeV}/c^2$ and $|\Delta E - \Delta E_0| < 2\sigma_{\Delta E}$ (see Section 3.4). Now we also define in the $D_s^{(*)+}\pi^0[\gamma]$ mass spectra a signal region

$$|m(D_s^{(*)+}\pi^0[\gamma]) - m(D_{sJ}^{(*)+})| < 2.5\sigma_m \qquad (3.11)$$

and a sideband region

$$4\sigma_m < |m(D_s^{(*)+}\pi^0[\gamma]) - m(D_{sJ}^{(*)+})| < 12\sigma_m \qquad (3.12)$$

with $m(D_{sJ}^{(*)+}) = 2.317\,{\rm GeV}/c^2$ $(2.460\,{\rm GeV}/c^2)$ for $D_s^+\,\pi^0$ $(D_s^{*+}\,\pi^0, D_s^+\,\gamma)$.

The ΔE, $m_{\rm ES}$ spectra of selected events are shown in Figure3.15 for each of the three $D_{sJ}^{(*)+}$ final states, after combining the charged and neutral $B \to D_{sJ}^{(*)+}\overline{D}^{(*)}$ modes and summing over all the $\overline{D}^{(*)}$ and $D_s^{(*)+}$ decays. No requirement of one single B candidate per mode is applied. The signal region of the other variable is selected. Data points are from $m(D_{sJ}^{(*)+})$ signal region, while the cross-hatched histograms are from the $m(D_{sJ}^{(*)+})$ sidebands. Clear signals for $B \to D_{sJ}D^{(*)}$ are observed in all channels.

In these plots, the ΔE resolution and offset in the data is fitted using the sum of a gaussian function for the signal and a polynomial background. The fit results are summarized in Table 3.6.

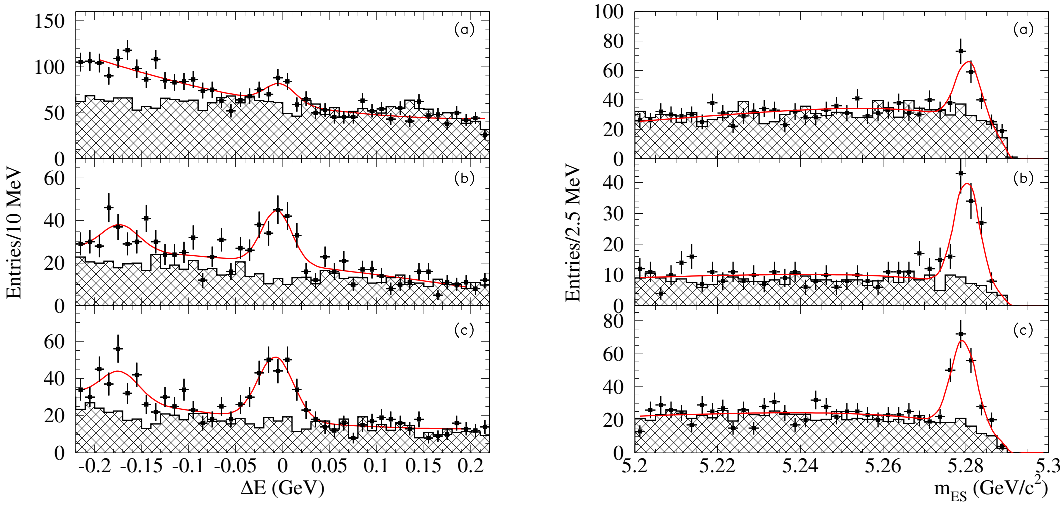

Figure 3.15: ΔE (left), $m_{\rm ES}$ (right) spectra for the $B \to \bar{D}^{(*)} D_{sJ}^{(*)+}$ candidates: (a) $D_{sJ}^*(2317) \to D_s^+\pi^0$, (b) $D_{sJ}(2460) \to D_s^+\pi^0$ and (c) $D_{sJ}(2460) \to D_s^+\gamma$. Data points are from events within 2.5 σ of the reconstructed $D_{sJ}^{(*)+}$ masses and the cross-hatched histograms are from the $m(D_{sJ}^{(*)+})$ sidebands. Curves are the results of the fits. The requirement of one single B candidate per mode is not applied.

From the simulation (see Section 3.4.1), we expect that the resolution for $D_s\pi^0$ and $D_s^*\pi^0$ modes should be the same. Because of the large background in the $D_s\pi^0$ mode we fix in the corresponding fit the $\sigma_{\Delta E}$ to the value obtained in the fit to the $D_s^*\pi^0$ mode. We also fit the $m_{\rm ES}$ spectra using the sum of a Gaussian signal and Argus background function. The yields extracted from the $m_{\rm ES}$ and ΔE spectra are in agreement (Table 3.6).

Table 3.6: Number of events and ΔE resolutions for data, from a single gaussian fit to the ΔE spectra of the $\overline{D}^{(*)}D_s^+\pi^0)$,$\overline{D}^{(*)}D_s^+\pi^0)$ and $\overline{D}^{(*)}D_s^+\gamma)$ final states (Figure3.15). Because of large backgrounds in the $D_s\pi^0$ channel, $\sigma_{\Delta E}$ had to be fixed to the same value of the channel $D_s^*\pi^0$, as expected from simulation. The yields obtained from a fit to the $m_{\rm ES}$ spectra (gaussian signal + argus background function) are also indicated.

mode	$m_{\rm ES}$ yield	ΔE yield	ΔE_0 (MeV)	$\sigma_{\Delta E}$
$B \to D_{s0}^+D^{(*)}$ $(D_{s0}^+ \to D_s^+\pi^0)$ (sum)	116 ± 17	85 ± 24	-2.7 ± 4.8	16 (fixed)
$B \to D_{s1}^+D^{(*)}$ $(D_{s1} \to D_s^{*+}\pi^0)$ (sum)	98 ± 12	99 ± 18	-6.2 ± 3.1	15.9 ± 2.6
$B \to D_{s1}^+D^{(*)}$ $(D_{s1} \to D_s^+\gamma$ (sum)	150 ± 16	161 ± 21	-7.6 ± 2.5	18.9 ± 2.3

Finally, to define the signal region we use an offset $\Delta E_0 = -5\,\mathrm{MeV}$ and a resolution $\sigma_{\Delta E} = 16\,\mathrm{MeV}$ (π^0 final states) and $\sigma_{\Delta E} = 20\,\mathrm{MeV}$ (γ final states). The width of the signal box is approximately $\pm 3\ \sigma$ in $m_{\rm ES}$ and $\pm 2\ \sigma$ in ΔE.

Figure 3.16 shows the reconstructed $D_s\pi^0$, $D_s^*\pi^0$ and $D_s\gamma$ mass spectra in the data (summed over the different B modes), without the requirement of one single B candidate per mode. The data points show the $D_s^{(*)}\pi^0,\gamma$ masses from events with $|\Delta E - \Delta E_0| < 2\sigma_{\Delta E}$ (signal region) and the histograms are from events with $4\sigma_{\Delta E} < |\Delta E - \Delta E_0| < 6\sigma_{\Delta E}$ (sideband region). A clear D_{sJ} signal is visible on each of the $D_s^{(*)}\pi^0,\gamma$ mass spectra from the ΔE signal region, while this signal is

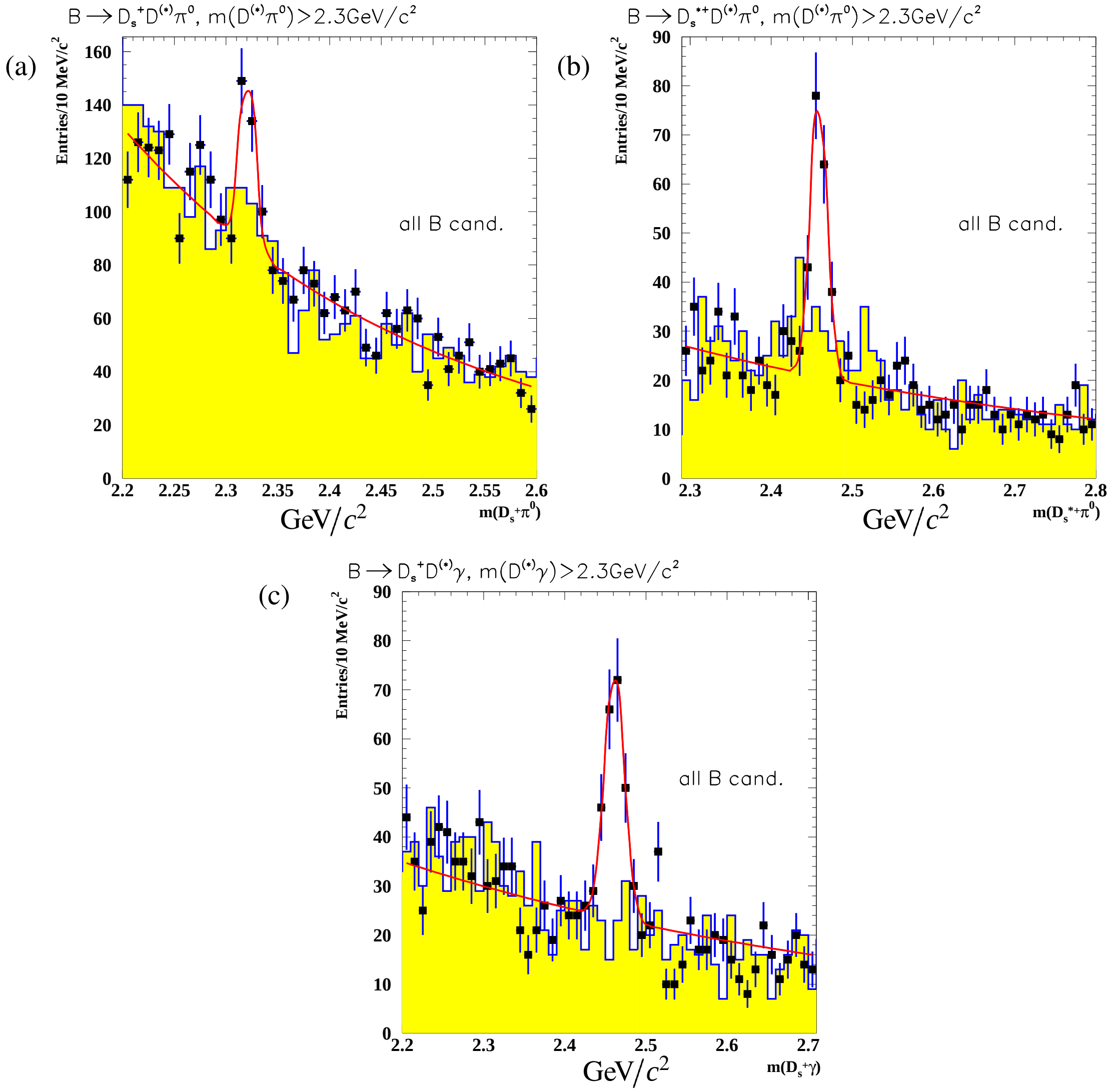

Figure 3.16: $D_s^{(*)}\pi^0$, $D_s\gamma$ invariant mass distributions for data events without the requirement of one single B candidate/mode. Data points: events with $|\Delta E - \Delta E_0| < 2\sigma_{\Delta E}$. Histogram: events with $4\sigma_{\Delta E} < |\Delta E - \Delta E_0| < 6\sigma_{\Delta E}$. (a) sum of $B \to D_{s0}^{+}\overline{D}^{(*)}$, $D_{s0}^{+} \to D_s\pi^0$ decays; (b) sum of $B \to D_{s1}^{+}\overline{D}^{(*)}$, $D_{s1}^{*+} \to D_s\pi^0$ decays;(c) sum of $B \to D_{s1}^{+}\overline{D}^{(*)}$, $D_{s1}^{*+} \to D_s\gamma$ decays.

not present for the events from the ΔE sideband. The spectra of Figure3.16 have been fitted by the sum of a gaussian decribing the signal function and an exponential function for the combinatorial background. The fitted numbers of events and D_{sJ} parameters are given in Table 3.7.

Finally we require only one candidate per B mode in each event using the best ΔE criteria (Section 3.4.4). The D_{sJ} mass spectra (Figure3.17) are from events in the ΔE signal region, defined above. These spectra have been fitted by the sum of a gaussian signal and exponential background function. The resulting parameters are summarized in table 3.8. The number of events found are in good agreement with the numbers resulting from the ΔE and m_{ES} fits. The resolutions on the D_{sJ} masses are in agreement with the expectations from the simulation.

Table 3.7: Number of events and average reconstructed D_{sJ} masses and resolutions in the data, from a single gaussian fit to the $m(D_{sJ})$ spectra of the $\overline{D}^{(*)}D_s^+\pi^0$,$\overline{D}^{(*)}D_s^+\pi^0$ and $\overline{D}^{(*)}D_s^+\gamma$ final states of Figure3.16.

mode	N events	$m(D_{sJ})$ (MeV/c^2)	σ_m
$B \to D_{s0}^+D^{(*)}$ $(D_{s0}^+ \to D_s^+\pi^0)$ (sum)	123 ± 23	2320.6 ± 1.8	7.2 ± 1.6
$B \to D_{s1}^+D^{(*)}$ $(D_{s1} \to D_s^{*+}\pi^0)$ (sum)	147 ± 17	2458.5 ± 1.3	10.3 ± 1.3
$B \to D_{s1}^+D^{(*)}$ $(D_{s1} \to D_s^+\gamma$ (sum)	154 ± 18	2461.2 ± 1.6	12.2 ± 1.4

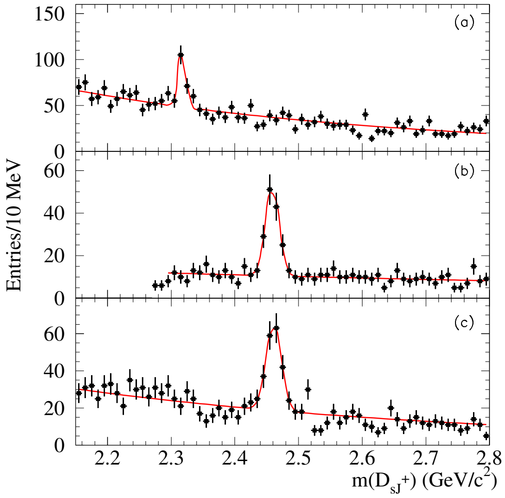

Figure 3.17: $D_s^{(*)}\pi^0$, $D_s\gamma$ invariant mass distributions for data events with the requirement of one single B candidate per mode. Events are in the m_{ES}, ΔE signal region. (a) sum of $B \to D_{s0}^+\overline{D}^{(*)}$, $D_{s0}^+ \to D_s\pi^0$ decays; (b) sum of $B \to D_{s1}^+\overline{D}^{(*)}$, $D_{s1}^{*+} \to D_s\pi^0$ decays;(c) sum of $B \to D_{s1}^+\overline{D}^{(*)}$, $D_{s1}^{*+} \to D_s\gamma$ decays.

3.5 Background and efficiency

This section describes some background studies and details the procedure used for estimating the efficiency with which we reconstruct the signal. Three types of background are studied; $B \to D_s^{(*)}D^{(*)}$ decays, generic B decays, and signal cross–feed. Contributions from the $B \to D_s^{(*)}D^{(*)}$ and generic B samples are accounted for by a separate part of the fitting function, assumed to be an exponential. The $B \to D_s^{(*)}D^{(*)}$ modes are expected to present the largest component of any background to the data set, and are studied here to check for a possible effect on the results. The

Table 3.8: Number of events and average reconstructed D_{sJ} masses and resolutions in the data, from a single gaussian fit to the $m(D_{sJ})$ spectra of the $\overline{D}^{(*)}D_s^+\pi^0$,$\overline{D}^{(*)}D_s^+\pi^0$ and $\overline{D}^{(*)}D_s^+\gamma$ final states of Figure3.15. (One single B candidate per mode, from best ΔE criteria)

mode	N events	$m(D_{sJ})$ (MeV/c^2)	σ_m
$B \to D_{s0}^+D^{(*)}$ $(D_{s0}^+ \to D_s^+\pi^0)$ (sum)	88 ± 17	2317.2 ± 1.3	5.9 ± 1.4
$B \to D_{s1}^+D^{(*)}$ $(D_{s1} \to D_s^{*+}\pi^0)$ (sum)	112 ± 13	2458.9 ± 1.4	10.8 ± 1.3
$B \to D_{s1}^+D^{(*)}$ $(D_{s1} \to D_s^+\gamma$ (sum)	139 ± 17	2461.1 ± 1.6	12.1 ± 1.6

generic sample is used to further demonstrate that background peaking in the signal region, other than the cross–feed, are not important in our final event sample. Finally, the signal sample is used to determine both the efficiencies and the cross–feed probabilities. The cross–feed is defined as signal events reconstructed in the wrong mode, but giving $D_s^{(*)}\pi^0$ or $D_s\gamma$ masses peaking in the D_{sJ} signal region. For most channels, the cross–feed contribution is small but non–negligible and will, therefore, be accounted for in the branching ratio calculation, using an iterative procedure described in the next section.

3.5.1 Background from generic events

To look for other sources of peaking background that may be present in the final event sample, we use a simulated generic B sample, that do not contain the modes $B \to D_{sJ}D^{(*)}$, corresponding approximately to twice the luminosity contained in data. The generic events are required to satisfy the full set of cuts as described in section 3.3 and 3.4, and to be in m_{ES} signal region (eq. 3.9). As in Section 3.4.1, we show in Figure 3.18(left) the ΔE distributions for events in $m(D_{sJ}^{(*)+})$ signal region (eq. 3.11) and in Figure 3.18(right) the $m(D_{sJ}^{(*)+})$ mass spectra of events in ΔE signal region (eq. 3.10). We observe no peak in both the distributions. We conclude that in our final event sample there is no background lying in the (m_{ES}, ΔE) B signal region from decay chains present in the generic simulation.

3.5.2 Background from $B \to D_s^{(*)}D^{(*)}$

In Section 3.6 we will select $B \to D_s^{(*)}D^{(*)}$ events as a control sample to validate the analysis procedure and the detector model, exploiting the close relation between these final states and the signal. For the same reason, these modes should also be considered as a potential source of peaking background.

The simulation set is processed in a manner identical to that of the data as detailed in Section 3.3 and 3.4, so including the rejection in Section 3.4.2. As before, in Figure 3.19(left) we show the ΔE distributions for events in m_{ES} and $m(D_{sJ}^{(*)+})$ signal region (eq. 3.9 and eq. 3.11) and in Figure 3.19(right) the $m(D_{sJ}^{(*)+})$ mass spectra of events in m_{ES} and ΔE signal region (eq. 3.9 and eq. 3.10). No evidence for background peaking in the ΔE or the $m(D_{sJ})$ signal regions is observed.

3.5.3 Efficiency and cross–feed

The estimation of efficiency and cross–feed and the computation of the final branching ratios, including cross–feed corrections, is made in several steps. First, we reconstruct each of the sixty modes, running the analysis on the sixty thousand simulated signal events of each of the sixty modes separately.

As an example, let's consider the reconstruction of $B^+ \to \bar{D}^{*0}D_{sJ}(2460)^+$, with $\bar{D}^{*0} \to \bar{D}^0\pi^0$, $\bar{D}^0 \to K^+\pi^-$ and $D_{sJ}(2460)^+ \to D_s^+\gamma$, $D_s^+ \to \phi\pi^+$. Selecting the ΔE and m_{ES} signal regions, we obtain sixty distributions of $D_s^+\gamma$ invariant mass, one for each generated signal decay. In the ideal case, only the reconstructed spectrum that corresponds to the generated $B^+ \to \bar{D}^{*0}D_{s1}^+$, $\bar{D}^{*0} \to \bar{D}^0\pi^0$, $\bar{D}^0 \to K^+\pi^-$, $D_{s1}^+ \to D_s^+\gamma$, $D_s^+ \to \phi\pi^+$ should appear.

We use a sum of two Gaussian functions to estimate the number of reconstructed events in the distribution corresponding to the same generated signal. The first Gaussian is used to describe the signal peak, the second gaussian is used to describe signal events that appear as underlying combinatorial. The efficiency is given by the number of reconstructed events divided by the number of generated events.

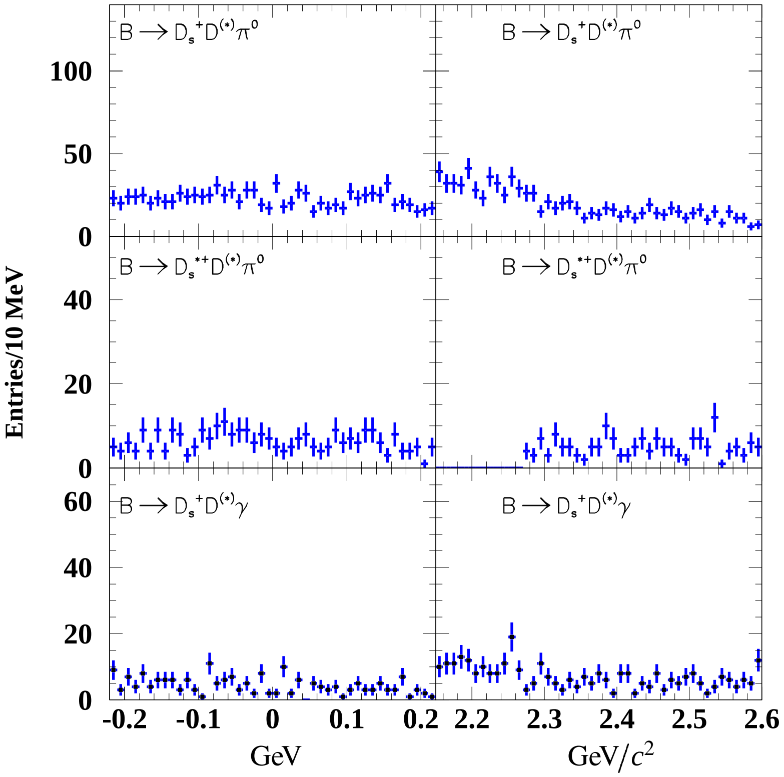

Figure 3.18: ΔE (left) and $m(D_{sJ})$ (right) distributions for simulation of B decays that do not contain the modes $B \to D_{sJ} D^{(*)}$. Events are in the $m_{\rm ES}$ signal region and in the signal region of the other variable. The reconstructed signal submodes with the same $D_{sJ}^{(*)+}$ decay are summed. This plot should be compared with the corresponding on generated signal in Figure 3.9 and 3.10.

All the remaining fifty-nine spectra should be empty, because the events are not a signal for the current mode under consideration. Some other generated signal decay mode (as an example $B^0 \to D^{*-} D_{s1}^+$, $D^{*-} \to \bar{D}^0 \pi^0$, $\bar{D}^0 \to K^+ \pi^-$, $D_{s1}^+ \to D_s^+ \gamma$, $D_s^+ \to \phi \pi^+$) could be reconstructed in the previous mode instead, as an example loosing the π^+ from D^{*+} and taking a fake π^0 that made a $\bar{D}^{*0}$. In fact we observe $D_s^+ \gamma$ invariant mass distributions not empty, and for some of the remaining modes we observe a peak in the $D_s^+ \gamma$ mass spectra.

The cross–feed $\varepsilon_{i,j}$ is defined as the ratio of the number of events fitted in the Gaussian for the reconstructed final state j to the total number of simulated events in the state i, when analyzing the simulated signal sample corresponding to this state. i and j run on all the submodes $(i, j = 1, 60)$. The case $i = j$ correspond to the value of the efficiency for the submode i considered. In fact $\varepsilon_{i,j}$ are the elements of a matrix 60×60 where efficiencies are in the diagonal.

To estimate this cross–feed, the spectra with more than twenty events (out of sixty thousand generated per each mode) are fitted with the sum of a Gaussian for the signal and a first order polynomial for the background. This requirement allows to have enough statistics to do a fit. The initial mean value of the Gaussian is chosen using the bin with the highest number of entries. The fit is made, allowing the mean and sigma of the Gaussian to float, in order to find the position and the width of any peak.

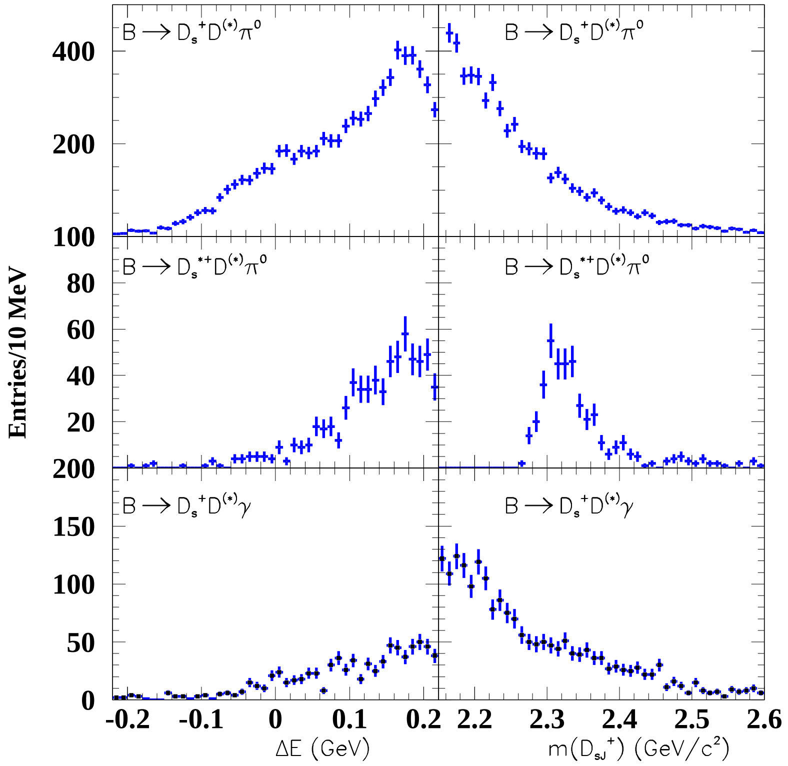

Figure 3.19: ΔE (left) and $m(D_{sJ})$ (right) distributions for $B \to D_s^{(*)}D^{(*)}$ simulated events. Events are in the m_{ES} signal region and in the signal region of the other variable. The reconstructed signal submodes with the same $D_{sJ}^{(*)+}$ decay are summed. Each of this plot should be compared with the corresponding one on generated signal in Figure 3.9 and 3.10.

The cross–feed is considered if the Gaussian peak have $\sigma < 50\,\mathrm{MeV}/c^2$, with a mean within $\pm 50\,\mathrm{MeV}/c^2$ of the expected D_{sJ} signal, i.e. 2317 MeV/c^2 for the D_{s0} and 2460 MeV/c^2 for the D_{s1}. If $\sigma > 50\,\mathrm{MeV}/c^2$ or the mean is more than $\pm 50\,\mathrm{MeV}/c^2$ far from the $m(D_{sJ}^{(*)+})$ signal region, the cross–feed can be handled with a background function or neglected because not peaking in the signal region.

The cross–feed contributions are separated into *narrow* (from D_{s0} to D_{s0} or from D_{s1} to D_{s1}) and *wide* (from D_{s0} to D_{s1} or from D_{s1} to D_{s0}) contributions which are processed differently.

To obtain an accurate estimate of the cross–feed matrix elements, the fits are then redone, fixing for the non–diagonal terms the mean and width of the gaussian. For “narrow” cross–feed we fix the σ of the gaussian to $8\,\mathrm{MeV}/c^2$, for final states with $D_s^+\pi^0$ and $D_s^*\pi^0$ and to $12.6\,\mathrm{MeV}/c^2$, for final states with $D_s^+\gamma$; for “wide” cross–feed the σ is set to $18\,\mathrm{MeV}/c^2$ for final states with $D_s^+\pi^0$ and to $20\,\mathrm{MeV}/c^2$ for final states with $D_s^*\pi^0$. No “wide” cross–feed is observed in final states with $D_s^+\gamma$.

For the fits of the diagonal terms (efficiencies) the mean and width of the signal gaussian are left floating and a wide gaussian background (instead of a first order polynomial) is used. As before, when we find a very wide spectrum ($\sigma > 50\,\mathrm{MeV}/c^2$) we do not keep it as a cross–feed because this will be modeled by the overall background fitting function, but a visual ispection is necessary because a random fluctuation can fit it as a narrow peak instead.

In tables A.11, A.12 and A.13 the estimated efficiency and cross–feed values $\varepsilon_{i,j}$ are reported. The masses and widths reported correspond to the identified contributions. From the diagonal terms $i = j$, one should note that the fitted D_{sJ} mass resolution is close to 8 MeV$/c^2$ for all the final states $D_s^+\pi^0$ and $D_s^{*+}\pi^0$, while it is close to 12 MeV$/c^2$ for all the $D_s^+\gamma$ final states.

The main sources of identified cross–feed, classified by decreasing order of magnitude, are the following:

1. D^{*+} reconstructed as D^{*0} (Figure 3.20a): the soft π^+ from $D^{*+} \to D^0\pi^+$ is not reconstructed and the D^0 from D^{*+} is associated with a π^0 or a γ from combinatorial background to form a fake D^{*0}. This results in a significant cross–feed from the modes $B^0 \to D_{sJ}^+D^{*-}$ to the modes $B^+ \to D_{sJ}^+\overline{D}^{*0}$. The cross–feed efficiency between those two final states is, on average, 20% of the efficiency for $B^0 \to D_{sJ}^+D^{*-}$. The masses and widths of this cross–feed are of course the same as those from D_{sJ} in correctly reconstructed B decays.

2. Decays $B^0 \to D_{s0}^+D^{*-}$ or $B^+ \to D_{s0}^+\overline{D}^{*0}$ ($D_{s0}^+ \to D_s^+\pi^0$) reconstructed as $B^+ \to D_{s1}^+\overline{D}^0$ ($D_{s1}^+ \to D_s^{*+}\pi^0$) (Figure 3.20b): the soft π or γ from the D^* is not reconstructed and, at the same time, a fake D_s^{*+} is built from the D_s^+ from the D_{s0}^+ combined with a γ from the combinatorial background. Because the $D_{s1}^+ - D_{s0}^+$ mass difference is approximately the same as the $D_s^{*+} - D_{s0}^+$ mass difference, the cross–feed background peaks approximately at the D_{s1}^+ mass but its mass resolution is about 20 to 25 MeV$/c^2$ while the resolution expected for a true D_{s1} signal is about 8 MeV$/c^2$. The cross–feed efficiency for each of the transitions $B^0 \to D_{s0}^+D^{*-}$ and $B^+ \to D_{s0}^+\overline{D}^{*0}$, ($D_{s0}^+ \to D_s^+\pi^0$) to the $D_s^{*+}\overline{D}^0\pi^0$ final states is approximately 10% of the efficiency for $B^+ \to D_{s1}^+\overline{D}^0$, ($D_{s1}^+ \to D_s^{*+}\pi^0$) which is of course the only final state affected by this cross–feed.

3. Decays $B^+ \to D_{s1}^+\overline{D}^0$, ($D_{s1}^+ \to D_s^{*+}\pi^0$) reconstructed as $B^+ \to D_{s0}^+\overline{D}^{*0}$, ($D_{s0}^+ \to D_s^+\pi^0$). This cross–feed is of the same type as the previous one; the γ from the D_s^{*+} is not reconstructed and a fake D^{*0} is built from a true D^0 and a γ or π^0 from the combinatorial background. This cross–feed peaks at the D_{s0} mass but its width is a factor two wider than the resolution for the true D_{s0} signal. The cross–feed efficiency for the transitions $B^+ \to D_{s1}^+\overline{D}^0$, ($D_{s1}^+ \to D_s^{*+}\pi^0$) to the $D_s^+\overline{D}^{*0}\pi^0$ final states is about 10% to 15% of the efficiency for $B^+ \to D_{s0}^+\overline{D}^{*0}$, ($D_{s0}^+ \to D_s^+\pi^0$)

4. Finally, a small cross–feed is observed between the final states $B^+ \to D_{sJ}^+\overline{D}^0$ ($\overline{D}^0 \to K^+\pi^-\pi^0$) and the final states $B^0 \to D_{sJ}^+D^-$ ($D^- \to K^+\pi^-\pi^-$) due to the mis-identification of one π in the D^0 or D^+. This cross–feed is much smaller than the other types, *i.e.* the amplitude of the non-diagonal term is about 1% of the amplitude of the corresponding diagonal term.

From the results of tables A.11, A.12 and A.13, it can be concluded that the following modes have zero or negligible ($\approx$ 1%) cross–feed contributions:

- $B^0 \to D_{s0}^+D^-$, $B^0 \to D_{s0}^+D^{*-}$, $B^+ \to D_{s0}^+\overline{D}^0$
- $B^0 \to D_{s1}^+D^-$, $B^0 \to D_{s1}^+D^{*-}$ ($D_{s1}^+ \to D_s^{*+}\pi^0$)
- $B^0 \to D_{s1}^+D^-$, $B^0 \to D_{s1}^+D^{*-}$ ($D_{s1}^+ \to D_s^+\gamma$)

In contrast, the modes $B^+ \to D_{s0}^+\overline{D}^{*0}$, $B^+ \to D_{s1}^+\overline{D}^0$, $B^+ \to D_{s1}^+\overline{D}^{*0}$ ($D_{s1}^+ \to D_s^{*+}\pi^0$ and $D_{s1}^+ \to D_s^+\gamma$) have a significant ($\approx$ 10%) cross–feed from the other modes. For the modes $B^+ \to D_{s1}^+\overline{D}^0$ $D_{s1}^+ \to D_s^+\gamma$) and $B^+ \to D_{s1}^+\overline{D}^{*0}$ ($D_{s1}^+ \to D_s^{*+}\pi^0$ and $D_{s1}^+ \to D_s^+\gamma$) the cross–feed is internal to the $B \to D_{s1}^+X$ modes and has therefore the same reconstructed mass and resolution as the D_{s1}^+ signal

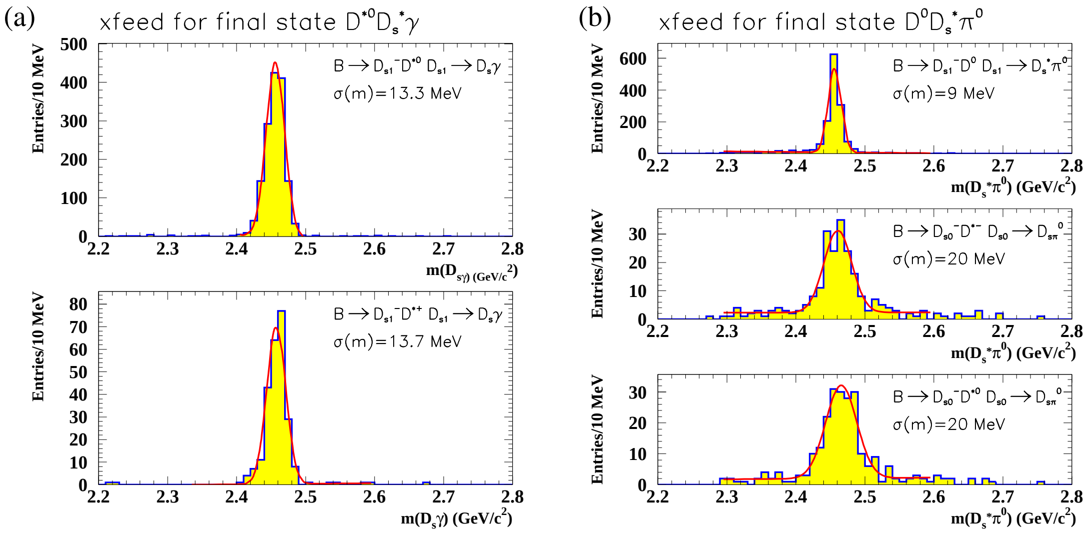

Figure 3.20: Examples for cross–feed between signal modes: (a) $D^{*0}D_s^*\gamma$ and (b) $D^0D_s^*\pi^0$ final states selected from simulated signal. The top plots show the actual D_{sJ} mass signals, in the bottom plots cross–feed contributions are shown.

($\approx$ 8 MeV for $D_{s1}^+ \to D_s^{*+}\pi^0$ and $\approx$ 12 MeV for $D_{s1}^+ \to D_s^+\gamma$). The mode $B^+ \to D_{s0}^+\overline{D}^{*0}$ receives a contribution from $B^+ \to D_{s1}^+\overline{D}^0$ and the decay $B^+ \to D_{s1}^+\overline{D}^0$ ($D_{s1}^+ \to D_s^{*+}\pi^0$) receives contributions from both $B^0 \to D_{s0}^+D^{*-}$ and $B^+ \to D_{s0}^+\overline{D}^{*0}$; these contributions have wider widths ($\approx \times 2$) than the resolutions on the true D_{s0}^+ and D_{s1}^+ signals.

As described in the next chapter, the “narrow” contribution is subtracted directly from the number of final fitted events while the wide contribution is fitted together with the yield in data, adding a gaussian with a normalization, mean and width fixed to the values obtained here. We observe that the mean of this contribution is displaced with respect to the signal by a few MeV.

3.6 $B \to D_S^{(*)} D^{(*)}$ Control sample

One of the cross-checks for our analysis is the measurement of branching fractions for $B \to D_S^{(*)}D^{(*)}$. The analysis method required almost duplicates that of $B \to D^{(*)}D_{sJ}$; as an example, the final states for $D^{(*)}D_s^*$ have the same final particles content as for $D^{(*)}D_{sJ}$ where the D_{sJ} decays to $D_s\gamma$. Comparing efficiencies and resolutions between these states gives us confidence that our analysis procedure is correct.

The selection criteria for these modes are the same as for the D_{sJ} modes. Since the cuts are rather tight, this method is not optimal for measuring the branching fractions, but it is good enough as a cross-check. The method used is the same for the D_{sJ} modes with the exception, of course, of the $D^{(*)}D_S^{(*)}$ mode rejection. The simulated sample $B \to D_S^{(*)}D^{(*)}$ is described in Section 3.5.2.

Distributions of ΔE and m_{ES} can be seen in Figg. 3.21- 3.24 for data and simulation summed over the $D^{(*)}$ and $D_S^{(*)}$ submodes. Since we do not have invariant mass $m(D_{SJ}^{(*)+})$ distributions to estimate efficiencies and extract the number of signal events, we use the simulation of each $D_S^{(*)}D^{(*)}$ and fit the ΔE distributions. Efficiencies and event yields are tabulated in Table 3.9. Data event yields are also found fitting ΔE histograms.The event yields are tabulated by submode in Table 3.10.

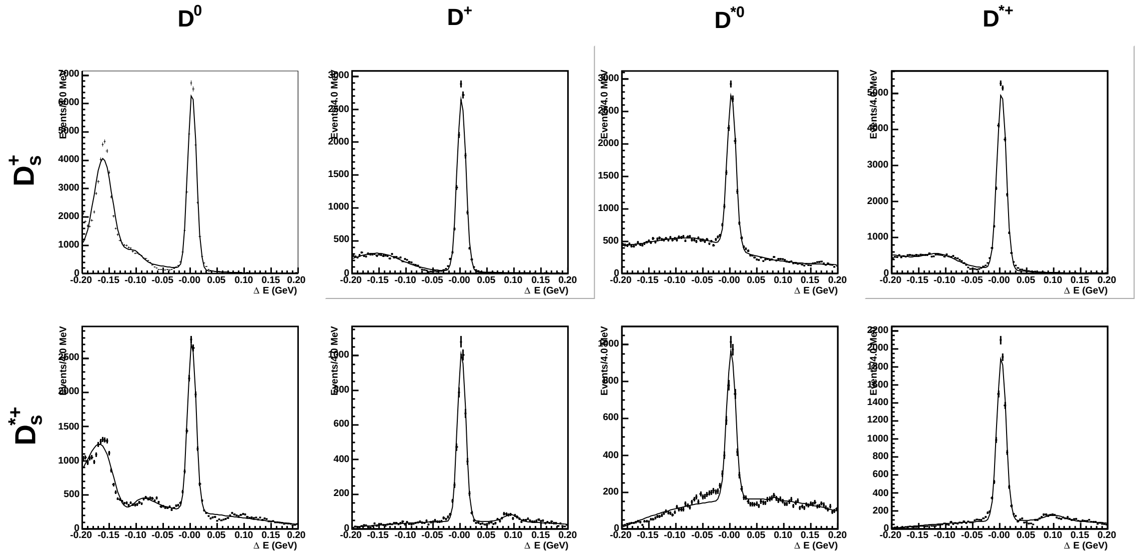

Figure 3.21: ΔE distributions for simulated $B \to D^{(*)}D_s^{(*)}$.

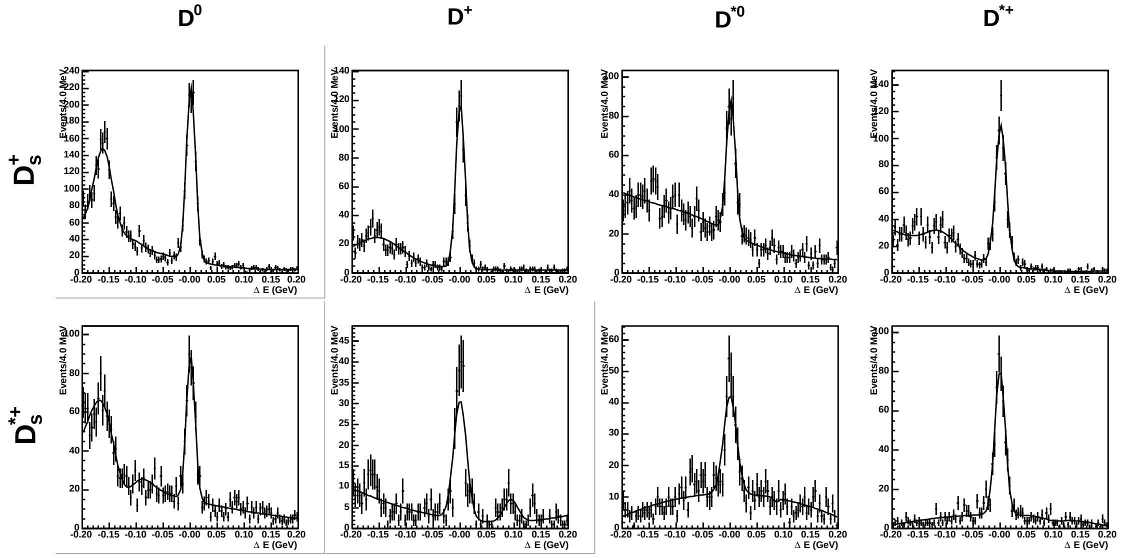

Figure 3.22: ΔE distributions for $B \to D^{(*)}D_s^{(*)}$ in data.

Branching fractions are calculated for each submode by taking the event yield and dividing by the number of $B\bar{B}$ pairs and the daughter branching fractions. The same tracking and kaon identification corrections used for the D_{SJ} modes have been applied. The branching fractions are listed in Table 3.11. The branching fractions between submodes are in agreement.

The branching fractions for the $D_s^{(*)}D^{(*)}$ modes are in good agreement with the known values [24]. The uncertainty on the D_s daughter branching fractions of about 30% dominate the systematic uncertainty in our measurement. This error should be added to the statistical error

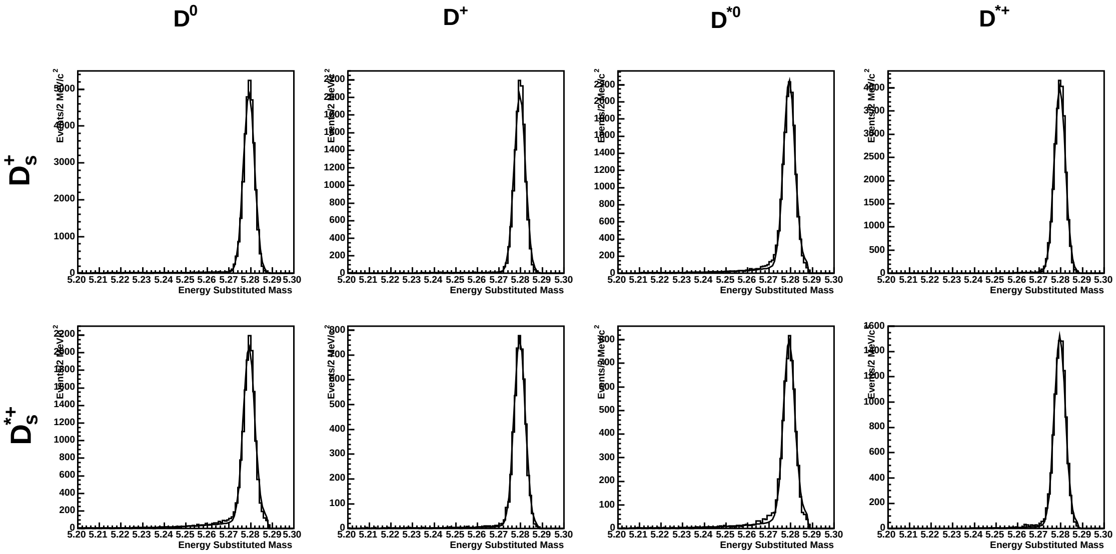

Figure 3.23: m_{ES} distributions for simulated $B \to D^{(*)} D_s^{(*)}$.

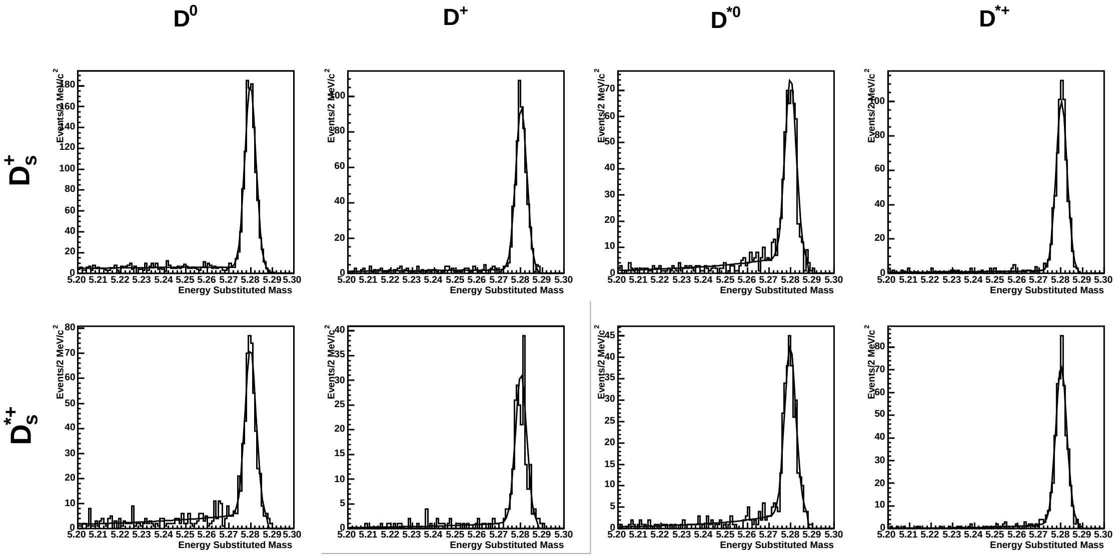

Figure 3.24: m_{ES} distributions for $B \to D^{(*)} D_s^{(*)}$ in data.

reported in table 3.11.

Table 3.9: Efficiency for simulated $D_s^{(*)}D^{(*)}$ *(%).*

Mode		D_s^+	D_s^{*+}
D^0	$K^+\pi^-$	18.9 ± 0.13	7.22 ± 0.09
	$K^+\pi^-\pi^0$	3.16 ± 0.06	1.33 ± 0.04
	$K^+\pi^-\pi^+\pi^-$	6.48 ± 0.08	2.27 ± 0.05
D^+	$K^+\pi^-\pi^+$	11.0 ± 0.10	4.10 ± 0.06
D^{*0}	$K^+\pi^-$	6.53 ± 0.09	2.41 ± 0.05
	$K^+\pi^-\pi^0$	1.45 ± 0.05	0.53 ± 0.02
	$K^+\pi^-\pi^+\pi^-$	2.43 ± 0.05	0.82 ± 0.03
D^{*+}	$K^+\pi^-$	12.4 ± 0.11	4.59 ± 0.07
	$K^+\pi^-\pi^0$	4.41 ± 0.07	1.72 ± 0.04
	$K^+\pi^-\pi^+\pi^-$	6.83 ± 0.08	2.50 ± 0.05

Table 3.10: Event Yield for $D_s^{(*)}D^{(*)}$ *Data.*

Mode		D_s^+	D_s^{*+}
D^0	$K^+\pi^-$	$236\pm11.$	83.7 ± 7.6
	$K^+\pi^-\pi^0$	$158\pm10.$	52.5 ± 6.8
	$K^+\pi^-\pi^+\pi^-$	$176\pm10.$	59.7 ± 6.6
D^+	$K^+\pi^-\pi^+$	$293\pm12.$	107 ± 8.0
D^{*0}	$K^+\pi^-$	34.7 ± 3.5	19.4 ± 2.8
	$K^+\pi^-\pi^0$	25.3 ± 3.9	16.5 ± 2.9
	$K^+\pi^-\pi^+\pi^-$	32.4 ± 3.5	16.2 ± 2.6
D^{*+}	$K^+\pi^-$	88.8 ± 6.5	63.8 ± 4.7
	$K^+\pi^-\pi^0$	132 ± 6.4	81.3 ± 7.9
	$K^+\pi^-\pi^+\pi^-$	105 ± 7.7	77.2 ± 6.8

Table 3.11: Branching Fractions for $B \to D_s^{(*)}D^{(*)}$ *(10^{-3}).*

Mode		D_s^+	D_s^+ [24]	D_s^{*+}	D_s^{*+} [24]
D^0	$K^+\pi^-$	13.4 ± 0.6	13.0 ± 4.0	13.4 ± 1.2	9.0 ± 4.0
	$K^+\pi^-\pi^0$	14.9 ± 0.9		12.7 ± 1.6	
	$K^+\pi^-\pi^+\pi^-$	14.4 ± 0.8		13.9 ± 1.5	
D^-	$K^-\pi^-\pi^+$	11.6 ± 0.5	8.0 ± 3.0	12.0 ± 0.8	10.0 ± 5.0
D^{*0}	$K^+\pi^-$	11.5 ± 1.1	12.0 ± 5.0	17.6 ± 2.5	27 ± 10
	$K^+\pi^-\pi^0$	10.4 ± 1.5		20.7 ± 3.3	
	$K^+\pi^-\pi^+\pi^-$	14.5 ± 1.5		23.3 ± 3.4	
D^{*-}	$K^+\pi^-$	11.2 ± 0.8	10.7 ± 2.9	22.9 ± 1.7	19.0 ± 5.0
	$K^+\pi^-\pi^0$	13.5 ± 0.6		22.7 ± 2.1	
	$K^+\pi^-\pi^+\pi^-$	12.3 ± 0.8		26.6 ± 2.3	

Chapter 4

Results

After discussing the method used to estimate the branching fractions, in this chapter the main results are summarized, including event yields, branching fractions, branching fraction ratios and angular analysis. Systematic uncertainties are also discussed in some detail.

4.1 Method

The method used to extract the branching fractions is the following:

1. First, we extract the observed number of events (N_{obs}) in the data for each of the twelve B decay modes. Using the sum of a Gaussian for the signal and of an exponential for the background, we fit the corresponding $D_s^{(*)+}\pi^0$ or $D_s^+\gamma$ mass spectra. N_{obs} is the integral of the Gaussian function. We do not split the different $D_s^+ \times \overline{D}$ decay sub-modes for lack of statistics.

2. From the efficiencies computed in section 3.5.3, the number of $B\overline{B}$ events, and the intermediate D, D_s and D^* branching fractions (shown in tables 3.1 and 3.2, and assuming D_s^{*+} going only to $D_s^+\gamma$), we compute the branching fractions, explicitly ignoring cross–feed:

$$\mathcal{B}(B \to D_{sJ}D^{(*)}) \times \mathcal{B}(D_{sJ} \to D_s^{(*)}\pi^0(\gamma)) = \frac{N_{obs}}{n_{B\bar{B}} \times \sum_{j,k} \mathcal{B}(D^{(*)} \to j)\mathcal{B}(D_s^{(*)} \to k)\varepsilon_{j,k}}, \quad (4.1)$$

   where N_{obs} is the observed number of events, $\mathcal{B}(D^{(*)} \to j)$ is the $D^{(*)}$ branching fraction to submode j, $\mathcal{B}(D_s^{(*)} \to k)$ is the D_s branching fraction to submode k, $\varepsilon_{j,k}$ is the efficiency for the $B \to D_{sJ}D^{(*)}$, $D_{sJ} \to D_s^{(*)}\pi^0(\gamma)$ submodes with $D^{(*)} \to j$, $D_s^{(*)} \to k$ and the sum is performed over all the submodes considered in the analysis. The sum $\sum_{j,k} \mathcal{B}(D^{(*)} \to j)\mathcal{B}(D_s^{(*)} \to k)\varepsilon_{j,k}$ is provided in the second-last column of table 4.2.

3. From this estimate of the branching fractions and the cross–feed matrix computed in Section 3.5.3, we extract the number of cross–feed events (narrow and wide) expected in each channel.

4. To refit the number of events in the data including the contribution of cross–feed, we use a second Gaussian. From simulation studies, the mean of this Gaussian is fixed at $5\,\mathrm{MeV}/c^2$ below the $D_{sJ}(2317)$ mass, for cross–feed from D_{s1} to the D_{s0}, and $8\,\mathrm{MeV}/c^2$ above the $D_{sJ}(2460)$ mass, for cross–feed from D_{s0} to the D_{s1}. The widths are $18(20)\,\mathrm{MeV}/c^2$ for

cross–feed from D_{s1} to the D_{s0} (D_{s0} to the D_{s1}). The normalization is fixed to the number of "wide" cross–feed events estimated from previous step.

5. We subtract the "narrow" cross–feed from N_{obs} and recompute the branching fractions, and iterate steps 2–5 until the result converges (three iterations were sufficient for our analysis).

4.2 Event yield after background subtraction

The $D_s^+\pi^0$, $D_s^{*+}\pi^0$ and $D_s^+\gamma$ mass spectra for each of the possible $D_s^{(*)+}\overline{D}^{(*)}\pi^0,\gamma$ final states are shown in Fig.4.1 ($\overline{D}^{(*)}D_s^+\pi^0$), Fig.4.2 ($\overline{D}^{(*)}D_s^+\pi^0$) and Fig.4.3 ($\overline{D}^{(*)}D_s^+\gamma$) for the events satisfying the final selection described in Section 3.4. In the first step of the iteration, these spectra are fitted by the sum of a Gaussian function describing the signal and an exponential background function. In the following steps, a second Gaussian describing the cross-feeds is added in the fits as described previously. Because of the low statistics, the average and width of the signal Gaussian are kept fixed to 2318 MeV/c^2 and 8 MeV/c^2 respectively for the D_{s0}, and 2460 MeV/c^2 and 12 MeV/c^2

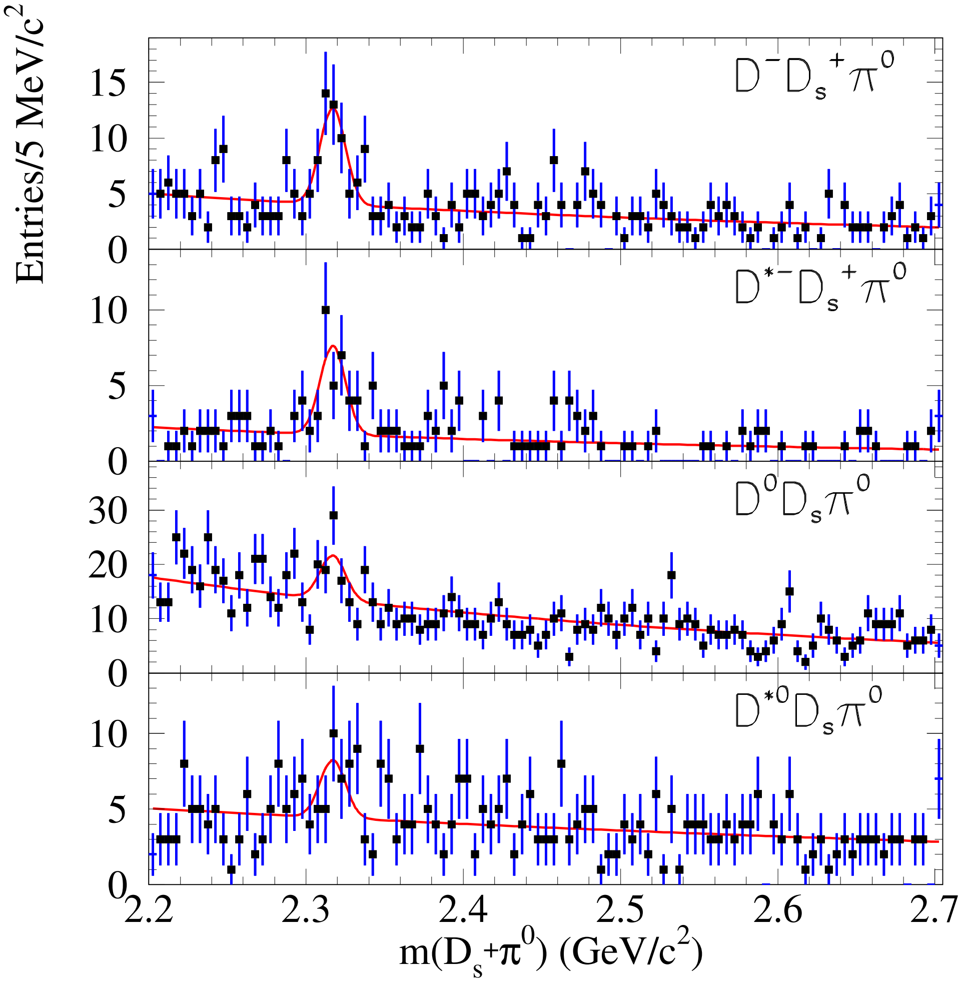

Figure 4.1: $m(D_{sJ})$ spectra in the data, for the $B\to D_{s0}^+\overline{D}^{(*)}$ modes

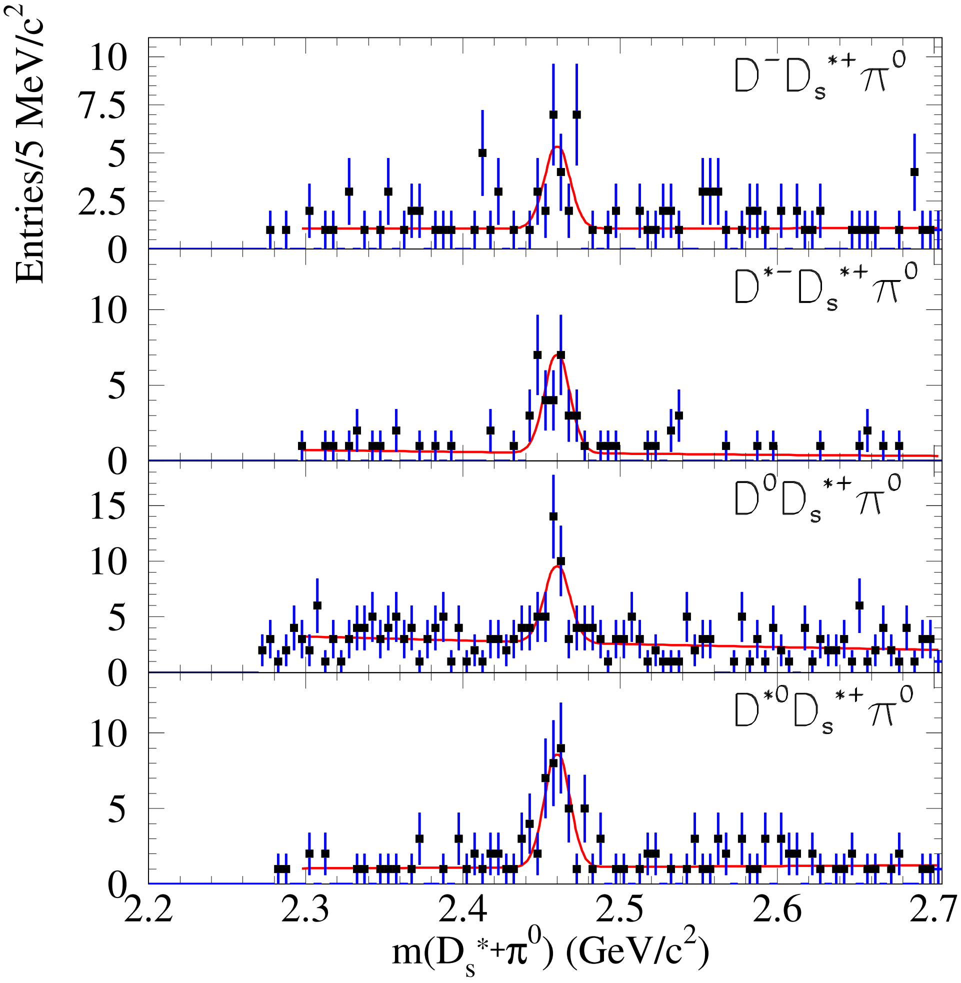

Figure 4.2: $m(D_{sJ})$ spectra in the data, for the $B \to D_{s1}^+\overline{D}^{(*)}$ ($D_{s1}^+ \to D_s^{*+}\pi^0$) modes

respectively for the D_{s1}, when performing the fits. The $D_{sJ}^{(*)+}$ event yields at first iteration (single Gaussian fit, no cross-feed) and the statistical significance of the signal are listed in Table 4.1. The significance is defined as $\sqrt{-2\ln(\mathcal{L}_0/\mathcal{L}_{max})}$, where $\mathcal{L}_{max}$ and $\mathcal{L}_0$ are the likelihood values with the nominal and with zero signal yield, respectively. A significance larger than 4 is observed for 10 out of the 12 modes. The number of fitted events after the last iteration, including the cross–feed (wide+narrow), are given in Table 4.2, together with the number of cross–feed events.

4.3 Efficiency corrections and Branching Fractions

From the number of events fitted for each mode, we extract the branching fractions using the method described in Section 4.1. The resulting branching fractions are given in Table 4.2, together with the signal yield and the estimated number of internal cross-feed events predicted for each of the different decay modes.

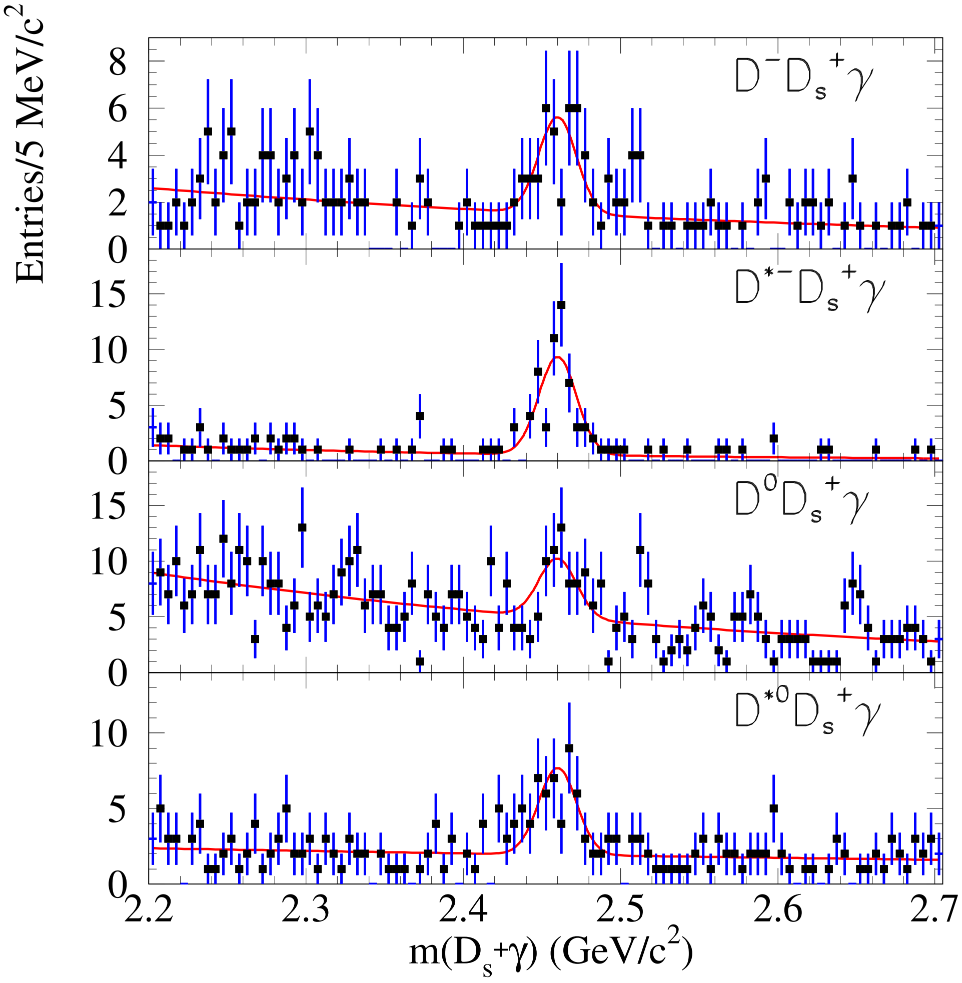

Figure 4.3: $m(D_{sJ})$ spectra in the data, for the $B \to D_{s1}^+ \overline{D}^{(*)}$ ($D_{s1}^+ \to D_s^+ \gamma$) modes

4.4 Systematic uncertainties

Systematic uncertainties are summarized in table 4.3. The relative variation of the branching fraction corresponding to each systematic error is given for each of the twelve B modes. The different components are added quadratically to provide the final systematic error (excluding the errors on the intermediate branching fractions).

4.4.1 Tracking

The simulation does not reproduce exactly the real data but needs a small correction on the efficiency, that can be dependent on the track selection. Usually a larger correction is required for a tighter selection.

The efficiencies for “very loose” selected tracks (GTVL), are corrected in the simulation by -0.5% per track, with a systematic error of 1.4% per track (see Section 2.4.4). The efficiencies for “loose” selected tracks (GTL), used only for kaons from D^0 and D^+, are corrected in the simulation by -0.8% per track, with a systematic error of 1.3% per track [55]. The resulting fractional errors

Table 4.1: Number of events for each B mode in the data, from a single Gaussian fit with fixed D_{sJ} masses and widths to the $m(D_{sJ})$ spectra of the $\overline{D}^{(*)}D_s^+\pi^0$ (Fig.4.1), $\overline{D}^{(*)}D_s^+\pi^0$ (Fig.4.2) and $\overline{D}^{(*)}D_s^+\gamma$ (Fig.4.3) final states. The results of the fits for the sum of these modes, when fitting with fixed D_{sJ} masses and widths, are also given (Fig.4.4).

mode	N events	$m(D_{sJ})$ (MeV/c^2)	σ_m (MeV/c^2)	significance
$B\to D_{s0}^+D^{(*)}$ ($D_{s0}^+\to D_s^+\pi^0$) (sum)	100.2 ± 16.0	2318.0 (fixed)	8.0 (fixed)	
$B^0\to D_{s0}^+D^-$ ($D_{s0}^+\to D_s^+\pi^0$)	34.8 ± 7.9	2318.0 (fixed)	8.0 (fixed)	5.5
$B^0\to D_{s0}^+D^{*-}$ ($D_{s0}^+\to D_s^+\pi^0$)	23.6 ± 6.1	2318.0 (fixed)	8.0 (fixed)	5.2
$B^+\to D_{s0}^+\overline{D}^0$ ($D_{s0}^+\to D_s^+\pi^0$)	32.7 ± 10.8	2318.0 (fixed)	8.0 (fixed)	3.1
$B^+\to D_{s0}^+\overline{D}^{*0}$ ($D_{s0}^+\to D_s^+\pi^0$)	15.3 ± 6.8	2318.0 (fixed)	8.0 (fixed)	2.5
$B\to D_{s1}^+D^{(*)}$ ($D_{s1}\to D_s^{*+}\pi^0$) (sum)	115.0 ± 14.2	2460.0 (fixed)	8.0 (fixed)	
$B^0\to D_{s1}^+D^-$ ($D_{s1}^+\to D_s^{*+}\pi^0$)	17.4 ± 5.1	2460.0 (fixed)	8.0 (fixed)	4.2
$B^0\to D_{s1}^+D^{*-}$ ($D_{s1}^+\to D_s^{*+}\pi^0$)	26.5 ± 5.6	2460.0 (fixed)	8.0 (fixed)	7.4
$B^+\to D_{s1}^+\overline{D}^0$ ($D_{s1}^+\to D_s^{*+}\pi^0$)	28.0 ± 5.8	2460.0 (fixed)	8.0 (fixed)	5.1
$B^+\to D_{s1}^+\overline{D}^{*0}$ ($D_{s1}^+\to D_s^{*+}\pi^0$)	30.5 ± 6.4	2460.0 (fixed)	8.0 (fixed)	7.7
$B\to D_{s1}^+D^{(*)}$ ($D_{s1}\to D_s^+\gamma$ (sum)	138.6 ± 15.3	2460.0 (fixed)	12.0 (fixed)	
$B^0\to D_{s1}^+D^-$ ($D_{s1}^+\to D_s^+\gamma$)	24.8 ± 6.5	2460.0 (fixed)	12.0 (fixed)	5.0
$B^0\to D_{s1}^+D^{*-}$ ($D_{s1}^+\to D_s^+\gamma$)	53.0 ± 7.7	2460.0 (fixed)	12.0 (fixed)	11.7
$B^+\to D_{s1}^+\overline{D}^0$ ($D_{s1}^+\to D_s^+\gamma$)	32.0 ± 8.9	2460.0 (fixed)	12.0 (fixed)	4.3
$B^+\to D_{s1}^+\overline{D}^{*0}$ ($D_{s1}^+\to D_s^+\gamma$)	34.6 ± 7.5	2460.0 (fixed)	12.0 (fixed)	6.0

on the branching fractions are given in Table 4.3.

4.4.2 π^0/γ selection

Possible differences between data and simulation on the neutral (γ and π^0) selection efficiencies are studied in detail using the hadronic τ decays $\tau^\pm\to h^\pm\nu$ where $h^\pm$ is $\pi^\pm$ or $\rho^\pm$ [56]. Roughly, the $\tau\to\rho$ yields will be proportional to the efficiency in reconstructing the $\pi^\pm$ and the π^0, while the $\tau\to\pi$ yield will be proportional to just the $\pi^\pm$ efficiency, leaving the relative π^0 efficiency. The measurement of the double ratio:

$$r=\frac{\frac{N(\tau\to\rho)(data)}{N(\tau\to\rho)(sim)}(p_{\pi^0})}{\frac{N(\tau\to\pi)(data)}{N(\tau\to\pi)(sim)}} \tag{4.2}$$

gives an absolute normalization, as well as testing the acceptance of the simulation. The conclusion is that the hadronic interaction in the EMC and the photon background are not perfectly modeled in the simulation. Since these effects are not completely understood, we decide not to apply corrections but to use a 2.5% systematic error per photon on the selection efficiencies.

4.4.3 Particle Identification

Using the inclusive samples of D^{*+} and of $D^0\to K\pi$ selected, we have determined the efficiency of our requirements on the charged K. The “KTight” efficiency is found to be 81.5±0.8% in the data and 83.1±0.2% in the simulated signal. From this study, a correction factor of -1.9% per KTight is applied to the selection efficiencies. To be conservative and account for possible differences in the “KNotAPion” selections, a 100% systematic error on this correction is assumed when computing the related systematic error.

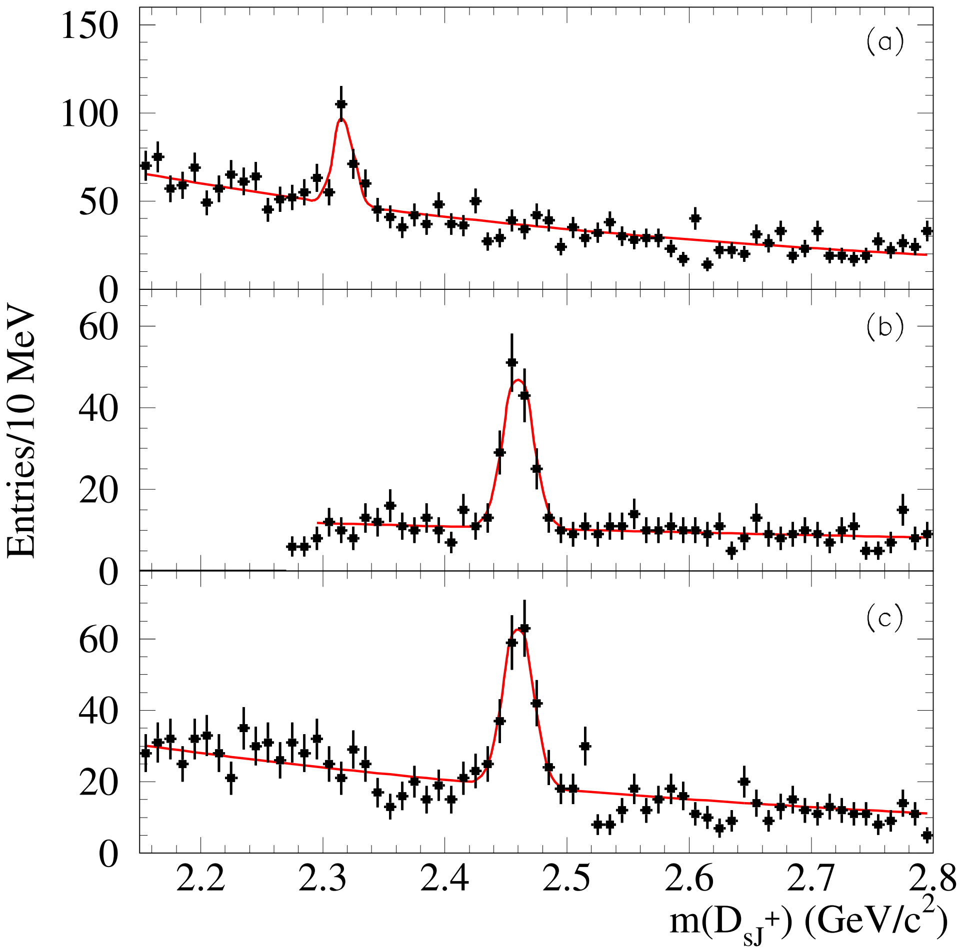

Figure 4.4: $m(D_{sJ})$ spectra in the events with $m(\overline{D}^{(*)}\pi^0,\gamma) > 2.3(2.4)\,\mathrm{GeV}/c^2$, for (a) the sum of $B \to D_{s0}^+\overline{D}^{(*)}$, $D_{s0}^+ \to D_s\pi^0$ decays; (b) the sum of $B \to D_{s1}^+\overline{D}^{(*)}$, $D_{s1}^{*+} \to D_s\pi^0$ decays;(c) the sum of $B \to D_{s1}^+\overline{D}^{(*)}$, $D_{s1}^{*+} \to D_s\gamma$ decays. In this plot, the mean and the resolution of the Gaussian used to fit the $m(D_{sJ})$ spectra of the signal have been fixed to the values used in the analysis, to the contrary of Fig.3.15.

4.4.4 D_{sJ} width

When fitting the number of events, the D_{sJ} mass resolution was fixed at $8\,\mathrm{MeV}/c^2$ for the π^0 final states and at $12\,\mathrm{MeV}/c^2$ for the γ final states. The resolution fitted on the data for the sum of the submodes is $8.3 \pm 1\,\mathrm{MeV}/c^2$ (average of $D_s^+\pi^0$ and $D_s^{*+}\pi^0$ final states) and $12.1 \pm 1.6\,\mathrm{MeV}/c^2$ ($D_s^+\gamma$ final states). To study the associated systematic, we repeated the fits by changing the D_{sJ} mass resolution by its statistical error, i.e. $\pm 1\,\mathrm{MeV}/c^2$ for the π^0 final states and $\pm 1.6\,\mathrm{MeV}/c^2$ for the γ final states.

Table 4.2: Number of events, internal cross-feed contributions, efficiencies and final branching fractions. The values in parenthesis in the cross–feed column are the wide cross–feed contributions, were present. The values in the efficiency column are defined as the sum over the different submodes of the submodes efficiencies times the intermediate $D^{(*)}$ and $D_s^{(*)}$ branching fractions. They are corrected from differences between simulation and data for tracking and PID, as described in the Section4.4

mode #	B mode	N events	cross- -feed	efficiency (10^{-4})	BR (10^{-3})
I	$D_{s0}^{+}D^{-}$ $(D_{s0}^{+} \to D_s^{+}\pi^0)$	34.7 ± 8.0	0.3	1.57	$1.80 \pm 0.42 \pm 0.26^{+0.63}_{-0.39}$
II	$D_{s0}^{+}D^{*-}$ $(D_{s0}^{+} \to D_s^{+}\pi^0)$	23.5 ± 6.1	0.0	1.29	$1.50 \pm 0.39 \pm 0.22^{+0.51}_{-0.31}$
III	$D_{s0}^{+}\overline{D}^{0}$ $(D_{s0}^{+} \to D_s^{+}\pi^0)$	32.7 ± 10.8	0.3	2.55	$1.04 \pm 0.35 \pm 0.13^{+0.36}_{-0.22}$
IV	$D_{s0}^{+}\overline{D}^{*0}$ $(D_{s0}^{+} \to D_s^{+}\pi^0)$	17.6 ± 6.8	7.1 (5.3)	0.99	$0.86 \pm 0.56 \pm 0.21^{+0.30}_{-0.18}$
V	$D_{s1}^{+}D^{-}$ $(D_{s1}^{+} \to D_s^{*+}\pi^0)$	17.4 ± 5.1	0.1	0.50	$2.80 \pm 0.83 \pm 0.46^{+0.96}_{-0.61}$
VI	$D_{s1}^{+}D^{*-}$ $(D_{s1}^{+} \to D_s^{*+}\pi^0)$	26.5 ± 5.7	0.0	0.39	$5.50 \pm 1.18 \pm 0.96^{+1.87}_{-1.15}$
VII	$D_{s1}^{+}\overline{D}^{0}$ $(D_{s1}^{+} \to D_s^{*+}\pi^0)$	29.0 ± 6.8	2.2 (2.2)	0.80	$2.73 \pm 0.70 \pm 0.46^{+0.93}_{-0.57}$
VIII	$D_{s1}^{+}\overline{D}^{*0}$ $(D_{s1}^{+} \to D_s^{*+}\pi^0)$	30.5 ± 6.4	2.5	0.30	$7.59 \pm 1.73 \pm 1.82^{+2.57}_{-1.59}$
IX	$D_{s1}^{+}D^{-}$ $(D_{s1}^{+} \to D_s^{+}\gamma)$	24.8 ± 6.5	0.5	2.62	$0.76 \pm 0.20 \pm 0.10^{+0.27}_{-0.16}$
X	$D_{s1}^{+}D^{*-}$ $(D_{s1}^{+} \to D_s^{+}\gamma)$	53.0 ± 7.8	0.1	1.92	$2.25 \pm 0.33 \pm 0.30^{+0.78}_{-0.47}$
XI	$D_{s1}^{+}\overline{D}^{0}$ $(D_{s1}^{+} \to D_s^{+}\gamma)$	31.9 ± 9.0	1.4	4.12	$0.61 \pm 0.18 \pm 0.08^{+0.21}_{-0.12}$
XII	$D_{s1}^{+}\overline{D}^{*0}$ $(D_{s1}^{+} \to D_s^{+}\gamma)$	34.6 ± 7.6	6.5	1.68	$1.37 \pm 0.37 \pm 0.29^{+0.46}_{-0.29}$

Table 4.3: Relative systematic errors, in % of the branching fraction, for each of the 12 B modes.

B mode	I	II	III	IV	V	VI	VII	VIII	IX	X	XI	XII
$N_{B\overline{B}}$	1	1	1	1	1	1	1	1	1	1	1	1
Tracking eff.	8	9	7	8	8	9	8	8	8	9	8	8
γ/π^0 eff.	5	7	7	12	8	10	9	14	2	5	4	9
PID eff.	0	0	1	1	0	0	1	1	0	0	1	1
D masses cuts	3	2	3	3	3	3	4	4	4	2	3	3
Δm D^{*0}/D_s^*	0	0	0	9	3	4	5	13	0	0	0	9
D_{sJ} width	7	6	4	10	8	6	6	5	6	3	4	10
bkg. fitting model	5	5	5	5	5	5	5	5	5	5	5	5
ΔE width	4	5	5	10	5	6	6	9	4	5	5	9
ΔE offset	1	1	1	1	1	1	1	1	1	1	1	1
combined	14	15	13	23	16	17	17	24	13	13	13	21

4.4.5 Background fitting model

The fits of the D_{sJ} mass spectra were repeated using a threshold function or a second order polynomial instead of an exponential background function. The maximum difference found in the rates was 5% and this value is therefore taken as an estimate of the systematic error linked to the background description.

4.4.6 Kinematic variables

We estimate the systematic error checking the effect of varying the resolutions on daughter particle masses and Δm, and on ΔE:

- the D and D_s^+ mass cuts are changed varying by ±10% (corresponding to the error on the resolution) the mass resolution assumed. The net effect is a change of $2-4\%$ in the final result.

- to account for possible differences between data and simulation in the Δm resolutions for $D^{*0} \to D^0\gamma, D^0\pi^0$ and $D_s^* \to D_s\gamma$, the efficiencies were recomputed by moving by ±20% the Δm cut for $D\gamma$ final states and by ±10% for $D\pi^0$.

- to account for the statistical uncertainty on the resolution $\sigma(\Delta E)$ in the data and for possible differences between data and simulation, the efficiencies were recomputed by moving by $\pm 3\,\mathrm{MeV}$ the resolutions $\sigma(\Delta E\ )$ used to define the signal region.

4.5 Isospin averaged branching fractions

One of the test proposed by theoretical papers is a measurement of the ratio of the electromagnetic decay with respect to the isospin violating one. We measured both decay types for the $D_{sJ}(2460)$. In order to have a relative estimate of the two branching fractions we combine the branching fractions for B^0 and B^+. To do so, we assume isospin invariance, expecting the same rate for decays that differ only for the charge. As an example $B^0 \to D_{sJ}(2460)^+D^-$ and $B^+ \to D_{sJ}(2460)^+D^0$. To give more weight to the better measured branching fraction, we average the results according to their statistical weight $w_i = 1/\sigma_i^2$:

$$\overline{\mathcal{B}} = \frac{1}{w}\sum_{i=1}^{n} w_i x_i \tag{4.3}$$

where $w = \sum_i w_i$. The standard deviation is $\sigma = 1/\sqrt{w}$. The averaged results are given in Table 4.4.

A recent measurement of $B \to D_{sJ}D^{(*)}$ decays from Belle is available in [57] for isospin averaged branching ratios. A comparison between *BABAR* and these results is also reported in Table 4.4. To check the agreement, we use the quantity [58]:

$$z = \frac{x_1 - x_2}{\sqrt{\sigma_1^2 + \sigma_2^2}} \tag{4.4}$$

where x_1 (σ_1) and x_2 (σ_2) are the mean value (total variance) of *BABAR* and Belle measurements. The variable z follow a gaussian distribution with mean value $x_z = 0$ and variance $\sigma_z = 1$. The decays with $D_{sJ}^+(2460) \to D_s^{*+}\pi^0$ show a z between one and two, so not a perfect agreement. Note also that Belle results are sistematically lower than *BABAR* results.

Table 4.4: Comparison of the Isospin averaged B branching fractions ($\times 10^{-4}$) between BABAR and Belle for the modes $B \to D_{sJ}D^{(*)}$.

Decay channel	*BABAR* [59] $\mathcal{B}(10^{-4})$	Belle [57] $\mathcal{B}(10^{-4})$	z
$B \to D_{sJ}^{*+}(2317)\overline{D}\ [D_s^+\pi^0]$	$13.5 \pm 2.7 \pm 1.8^{+4.7}_{-2.9}$	$10.1 \pm 1.5 \pm 3.0$	0.6
$B \to D_{sJ}^{*+}(2317)\overline{D}^*\ [D_s^+\pi^0]$	$12.9 \pm 3.2 \pm 2.2^{+4.4}_{-2.7}$	$3.1^{+2.1}_{-1.7}(< 8.5)$	-
$B \to D_{sJ}^{+}(2460)\overline{D}\ [D_s^{*+}\pi^0]$	$27.6 \pm 5.3 \pm 4.6^{+9.4}_{-5.8}$	$14.8^{+2.8}_{-2.5} \pm 4.4$	1.2
$B \to D_{sJ}^{+}(2460)\overline{D}^*\ [D_s^{*+}\pi^0]$	$61.7 \pm 9.8 \pm 12.3^{+20.9}_{-12.9}$	$28.7^{+7.4}_{-6.4} \pm 8.6$	2.0
$B \to D_{sJ}^{+}(2460)\overline{D}\ [D_s^+\gamma]$	$6.7 \pm 1.3 \pm 0.9^{+2.4}_{-1.4}$	$6.4 \pm 0.8 \pm 1.9$	0.1
$B \to D_{sJ}^{+}(2460)\overline{D}^*\ [D_s^+\gamma]$	$18.6 \pm 2.5 \pm 2.9^{+6.4}_{-3.9}$	$12.7^{+2.2}_{-2.0} \pm 3.8$	0.8

4.6 Measurement of ratios of branching fractions

From the measured branching fractions for $B \to D_{sJ}^{+}(2460)\overline{D}^{(*)}$ in the $D_s^{*+}\pi^0$ and in the $D_s^+\gamma$ final states, we measure $\mathcal{B}(D_{sJ}^{+}(2460) \to D_s^+\gamma)/\mathcal{B}(D_{sJ}^{+}(2460) \to D_s^{*+}\pi^0) = 0.244 \pm 0.066 \pm 0.016$ from $\bar{D}$ final states and $\mathcal{B}(D_{sJ}^{+}(2460) \to D_s^+\gamma)/\mathcal{B}(D_{sJ}^{+}(2460) \to D_s^{*+}\pi^0) = 0.302 \pm 0.062 \pm 0.025$ from $\bar{D}^*$ final states. The average of these two measurements gives:

$$\frac{\mathcal{B}(D_{sJ}^{+}(2460) \to D_s^+\gamma)}{\mathcal{B}(D_{sJ}^{+}(2460) \to D_s^{*+}\pi^0)} = 0.274 \pm 0.045 \pm 0.020. \tag{4.5}$$

in agreement with expectations in [12]. When combining the systematic errors together, we consider the correlation between them. Since some cancel in the ratio, only the different number of neutral particles and the variation of the width for ΔE, D_{sJ} and $\Delta m(D^*)$ contribute to the final systematic error.

With the isospin averaged measurements, is possible to compute the ratios introduced in Section 1.3. Taking the average of *BABAR* and Belle results, from the first line of table 4.4, we have approximately:

$$\mathcal{B}[B \to DD_{sJ}^{*}(2317)]\mathcal{B}[D_{sJ}^{*}(2317) \to D_s\pi^0] \approx 12 \times 10^{-4} \tag{4.6}$$

with the assumption that the dominant decay of the $D_{sJ}^{*}(2317)$ is expected to be through the $D_s\pi^0$ mode [32] we have

$$\mathcal{B}[B \to DD_{sJ}^{*}(2317)] \approx 1.2 \times 10^{-3} \tag{4.7}$$

Using the measured branching ratio [24]

$$\begin{aligned} \mathcal{B}(B^+ \to \bar{D}^0 D_s^+) &= (1.3 \pm 0.4) \times 10^{-2} \\ \mathcal{B}(B^0 \to D^- D_s^+) &= (8.0 \pm 3.0) \times 10^{-3} \end{aligned} \tag{4.8}$$

one obtains a combined branching ratio

$$\mathcal{B}[B \to DD_s^+] \approx 10^{-2} \tag{4.9}$$

Combining eq. 4.7 and eq. 4.9, the ratio obtained $R_{D0} \approx \frac{1}{10}$ is a factor 10 smaller than expectations in eq. 1.12. Similarly, averaging *BABAR* and Belle measurement of $B \to DD_{sJ}(2460)$ ($D_{sJ}(2460)^+ \to D_s^{*+}\pi^0$ and $D_{sJ}(2460)^+ \to D_s^+\gamma$), we obtain $\mathcal{B}[B \to DD_{sJ}(2460)] \approx 3 \times 10^{-3}$. Combining this value with $\mathcal{B}(B \to DD_s)$, a discrepancy with eq. 1.12 is found also in the ratio $R_{D1} \approx \frac{1}{3}$.

Our measurement of $B \to D_{sJ}D^*$ decays could allow to compute the R_{D^*0} and R_{D^*1} ratios. We could expect results similar to R_{D0} and R_{D1}. Computing the ratios as before, using only our measurements (table 4.4):

$$\begin{aligned} \mathcal{B}[B \to D^* D_{sJ}^{*}(2317)] &\approx 1.3 \times 10^{-3} \\ \mathcal{B}[B \to D^* D_{sJ}(2460)] &\approx 8.0 \times 10^{-3} \end{aligned} \tag{4.10}$$

and the combined branching ratios [24]:

$$\begin{aligned} \mathcal{B}[B \to D^* D_s^+] &\approx 2.3\% \\ \mathcal{B}[B \to D^* D_s^*] &\approx 4.6\% \end{aligned} \tag{4.11}$$

we obtain $R_{D^*0} \approx 0.06$ and $R_{D^*1} \approx 0.17$, a factor two far from R_{D0} and R_{D1} respectively.

It is possible that discrepancies between experiments and theory may arise from a combination of incorrect model prediction of p-wave state properties and nonfactorizable effects without requiring an exotic explanation.. More statistic is needed to conclude since the error on branching ratio measurements are still big (see sec. 4.5).

4.7 Angular analysis

An angular analysis of the $D_{sJ}(2460)$ decay was performed, using the channels $B^+ \to \bar{D}^0 D_{sJ}^+(2460)$ $[D_{sJ}^+ \to D_s^+\gamma]$ and $B^0 \to D^- D_{sJ}^+(2460)$ $[D_{sJ}^+ \to D_s^+\gamma]$. Since the decay $B \to DD_{sJ}$ is a $0^- \to 0^- J^P$ transition, the resulting D_{sJ} is polarized. We tested the hypotheses $J = 1$ and $J = 2$ for the $D_{sJ}(2460)$ spin. The spin $J = 0$ is ruled out by parity and angular momentum conservation in the decay $D_{sJ}(2460) \to D_s^+\gamma$. Information on the D_{sJ} spin J can be obtained from the distribution of a suitably defined helicity angle. The helicity angle θ_h is defined as the angle between the D_{sJ} momentum in the B meson rest frame and the D_s momentum in the D_{sJ} rest frame, see Figure 4.5.

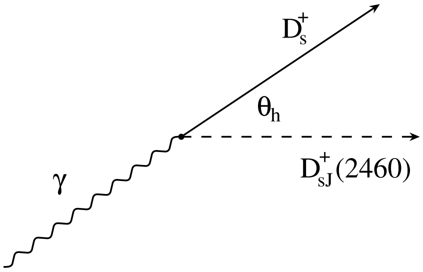

Figure 4.5: Helicity angle θ_h definition.

The $m(D_s\gamma)$ signal for data events with a reconstructed $DD_s\gamma$ final state, based on the selection described in section 3.4, is shown in Figure 4.6(a). Fitting with a single Gaussian, yields

$$m(D_{sJ}) = (2465 \pm 3)\ \text{MeV/c}^2, \quad \sigma_m = (11.5 \pm 2.3)\ \text{MeV/c}^2 \tag{4.12}$$

and (90 ± 18) signal events in the peak. Figure 4.6(b) shows the signal after dropping the requirement of a minimum $D\gamma$ mass of 2.3 GeV/c^2. Here, the number of signal events is determined to be $N_{sig} = (66 \pm 14)$ with negligible changes in the results for $m(D_{sJ})$ and σ_m. While a comparison

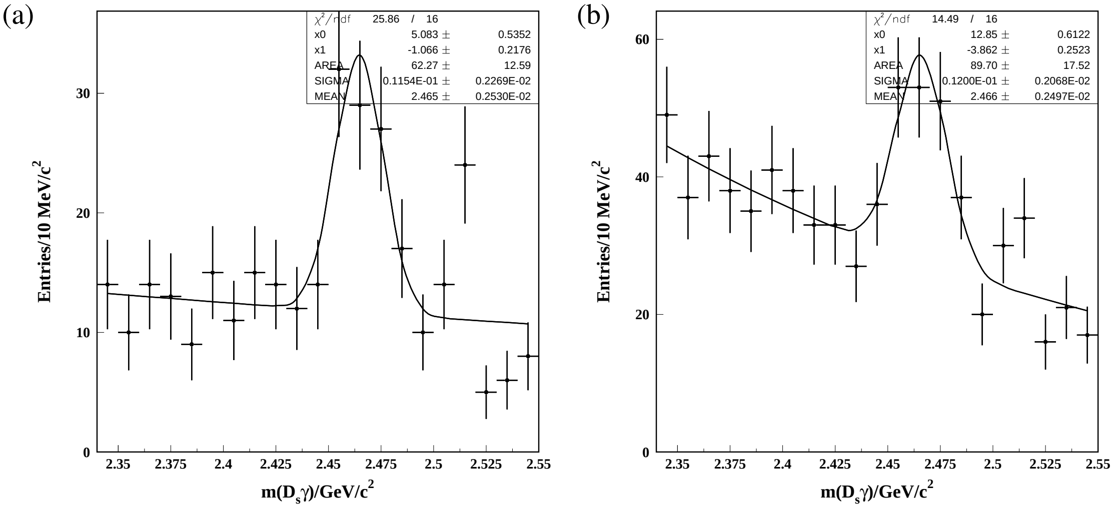

Figure 4.6: Fits to the $m(D_s\gamma)$ signal for reconstructed $DD_s\gamma$ data events: (a) with the default analysis cut and (b) after dropping the requirement of a minimum $D\gamma$ mass of 2.3 GeV/c^2.

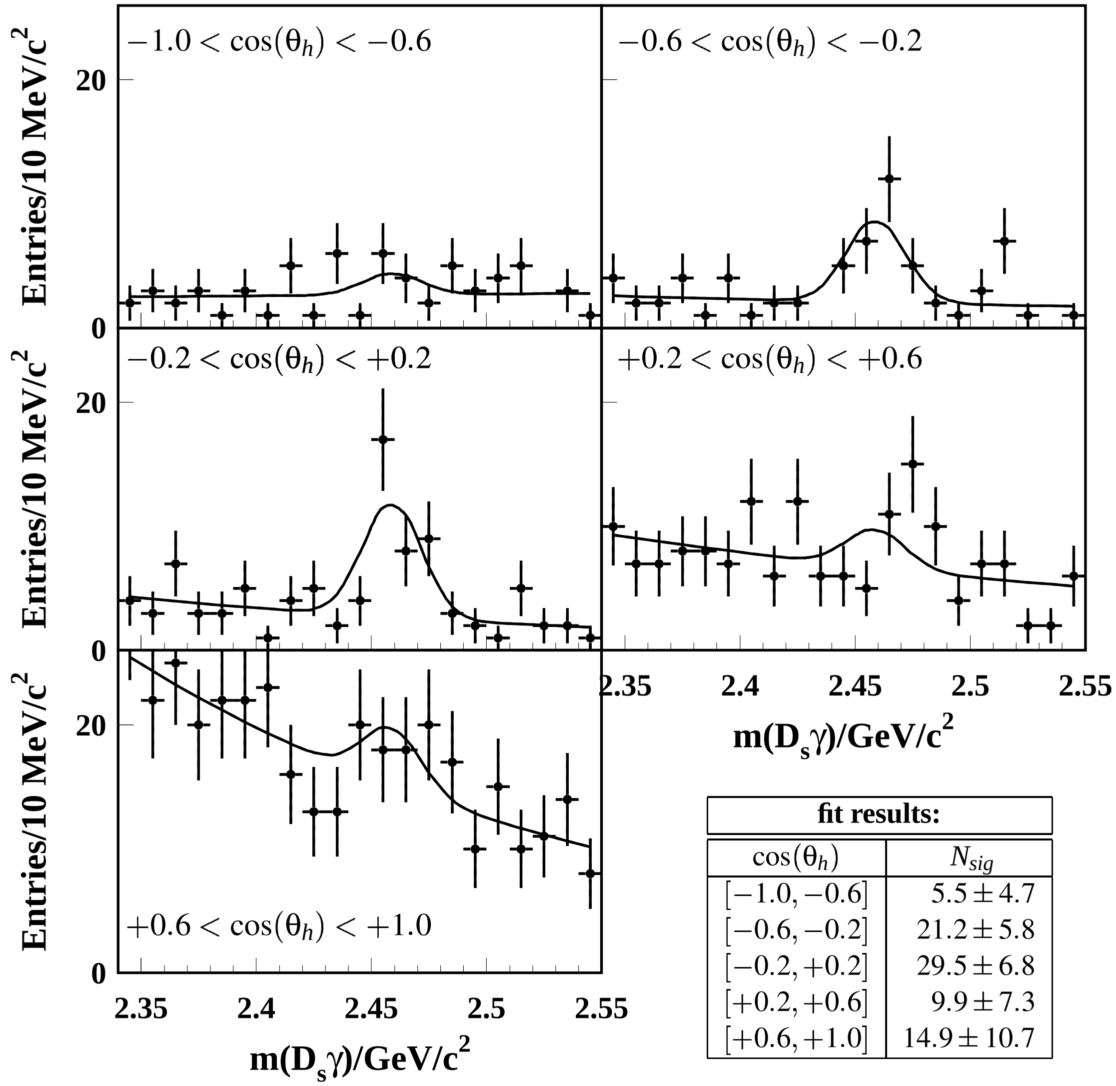

fit results:	
$\cos(\theta_h)$	N_{sig}
$[-1.0,-0.6]$	5.5 ± 4.7
$[-0.6,-0.2]$	21.2 ± 5.8
$[-0.2,+0.2]$	29.5 ± 6.8
$[+0.2,+0.6]$	9.9 ± 7.3
$[+0.6,+1.0]$	14.9 ± 10.7

Figure 4.7: Fits to the $m(D_s\gamma)$ data distribution for different $\cos(\theta_h)$ regions for the selected BABAR data sample. The mean and width of the Gaussian have been fixed according to Equation (4.12).

of Figures 4.6(a) and (b) demonstrates again the positive effect of the $m(D\gamma)$ cut on the signal–to–noise ratio, this cut is slightly problematic for the helicity analysis. The $D\gamma$ mass is correlated with the helicity angle, with a minimum $m(D\gamma)$ requirement suppressing events in the high $\cos(\theta_h)$ region. For this reason, in the following this cut is not applied.

In order to extract the angular information, fits to the $m(D_s\gamma)$ distribution from the data are performed for five different $\cos(\theta_h)$ regions, see Figure 4.7. Here, the mean and width of the Gaussian have been fixed according to Eq. (4.12). The same procedure is repeated for the simulated signal sample, which was produced assuming $J = 1$ for the spin of the $D_{sJ}(2460)$ state.

The resulting $\cos(\theta_h)$ distributions for the *BABAR* data and simulated signal are compared in Figure 4.8(a), where the simulation has been normalized to the data, and good agreement is found within the errors obtained from the fits. The reconstructed helicity angle distribution in simulation still follows very well the generated $(1-\cos^2(\theta_h))$ shape, cfr Figure 4.8(b). From the small differences between the two distributions, corrections for detector acceptance and selection efficiency are derived. After applying these corrections to the data, the analytical expectations for different spin hypotheses can be overlaid directly. The results for $J=1$ and $J=2$ are shown in Figure 4.8(c) and (d) respectively, where the prediction has been normalized to the data. While we find good agreement for the $J=1$ hypothesis (χ^2/n.d.f.=3.9/4), the $J=2$ hypothesis is excluded (χ^2/n.d.f.=34.5/4).

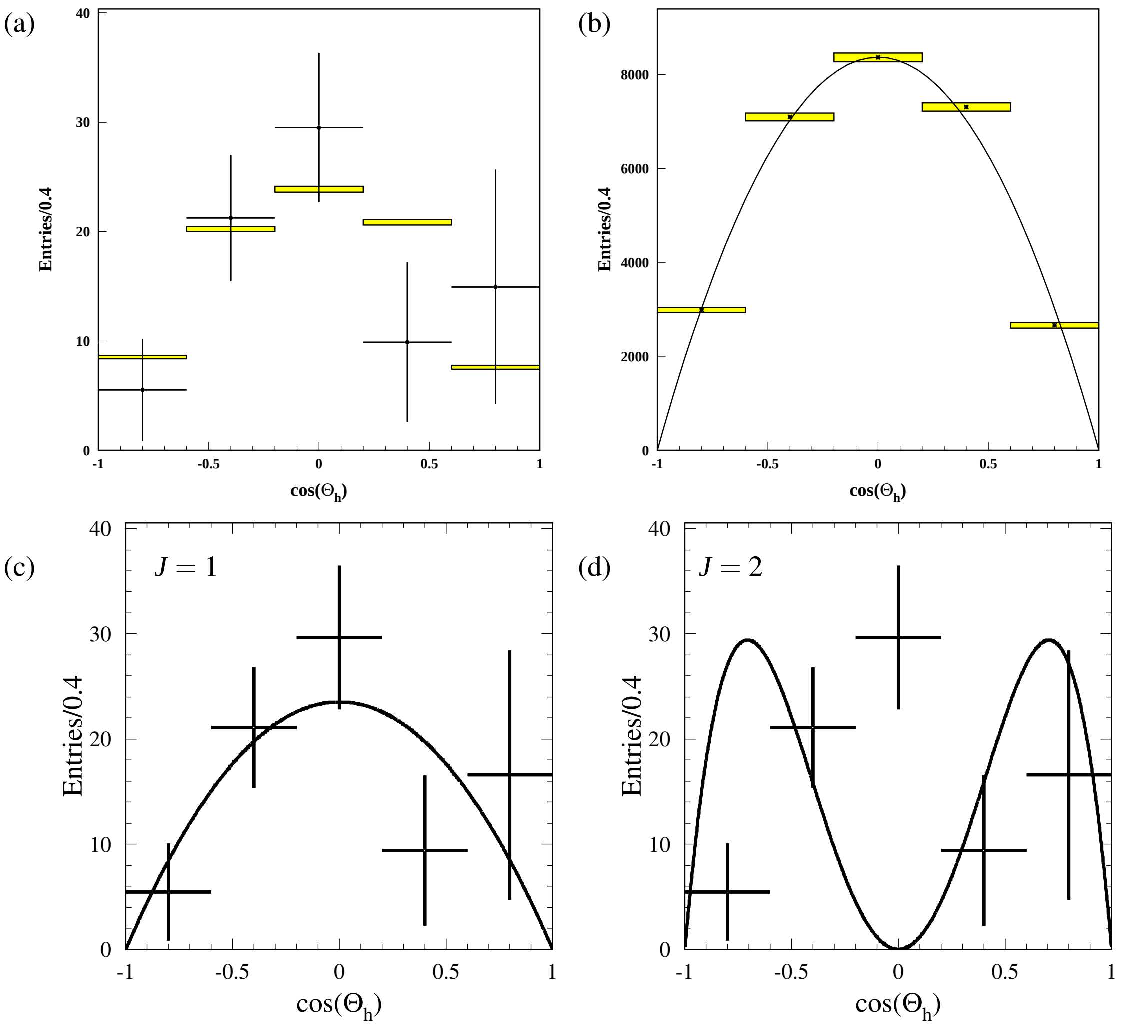

Figure 4.8: Helicity distributions obtained from $m(D_s\gamma)$ *fits in the corresponding* $\cos(\theta_h)$ *region for selected BABAR data (points) and fully reconstructed simulated signal events (shaded), where the simulation sample was produced assuming* $J=1$ *for the spin of the* $D_{sJ}(2460)$ *state. The shown errors correspond to the fit errors and do not include any further systematic error contributions. In Figures (c) and (d), the data is shown after applying corrections for detector acceptance and selection efficiency obtained from* $J=1$ *simulated signal. The solid curves are the analytical expectations for two different* $D_{sJ}(2460)$ *spin hypotheses, which have been normalized to the data: (c)* $J=1$ *and (d)* $J=2$*.*

Conclusions

In this thesis we have shown that a B-factory is a good environment for a detailed study of charm spectroscopy. The new D_{sJ} resonances observed by *BABAR* in continuum $c\bar{c}$ production are confirmed also in B decays. The clean environment offered by $B\bar{B}$ events allows to study the sources of backgrounds and the cross–feed between different modes very carefully.

We considered sixty different final states. We combined them toghether to obtain twelve combined branching ratio measurements of $B \to D_{sJ}D^{(*)}$, with $D_{sJ}^*(2317)^+ \to D_s^+\pi^0$, $D_{sJ}(2460)^+ \to D_s^{*+}\pi^0$, and $D_{sJ}(2460)^+ \to D_s^+\gamma$. The six with the emission of a D^* or a D^{*0} are seen for the first time. The other six $B \to D_{sJ}D$ are compatible within errors with results from Belle [40]. A comparison for isospin averaged branching fractions is also done but is not perfect for $B \to D_{sJ}D^*$ modes. This work has been published in Physics Review Letters [59]. The angular analysis performed for the modes with $D_{sJ}(2460) \to D_s\gamma$ leads to the measurement of J^P, supporting the hypothesis that $D_{sJ}(2460)$ is a 1^+ state.

Further information on the nature of the $D_{sJ}(2460)$ is also obtained measuring the radiative contribution to the ratio of branching fractions for $D_{sJ}(2460)^+ \to D_s^+\gamma$ and $D_s^{*+}\pi^0$.

We computed ratios of branching ratios for $B \to DD_s^+$ and $B \to DD_{sJ}^*(2317)$ (R_{D0}) and $B \to DD_{sJ}(2460)$ (R_{D1}). In the factorization assumption, if $D_{sJ}^{(*)+}$ are the D_{s0}^* and the D_{s1}, we expect $R_{D0} \approx R_{D1} \approx 1$ [21]. We found $R_{D0} \approx \frac{1}{10}$ and $R_{D1} \approx \frac{1}{3}$ not supporting these hypothesis.

As argued in [60], the $D_{sJ}^*(2317)$ and $D_{sJ}(2460)$ should have large electromagnetic branching ratios and very small widths, $O(10\,\mathrm{keV})$, if they are conventional $c\bar{s}$ states. Instead, $D^{(*)}K$ molecules should have large widths $O(\mathrm{MeV})$ and absence of electromagnetic decay. We have no answers on the widths yet, because the predictions are below the experimental resolution, but we do observe an electromagnetic decay for the $D_{sJ}(2460)$ supporting the conventional $c\bar{s}$ hypothesis; but no such electromagnetic decay is observed for $D_{sJ}^*(2317)$ state [35].

The $B \to D_{sJ}D^{(*)}$ results are substantially in agreement with the meson interpretation of these states. The fact that we do not observe other candidates for these states suggests that they could be just ordinary mesons.

On the contrary, if the D_{sJ} states were exotic, we would expect them to belong to a family of exotic states, and we might expect to find evidence of the existence of other members of this family. No such evidence has been found [35].

In conclusion, we measure $B \to D_{sJ}D^{(*)}$ branching fractions and $D_{sJ}(2460)$ quantum numbers; we compute isospin averaged branching fractions and relate them to $B \to D_s^{(*)}D^{(*)}$ decays computing ratios of branching fractions. Most of the D_{sJ} theoretical pictures are not ruled out by these measurements. To understand better the nature of $D_{sJ}^*(2317)$ and $D_{sJ}(2460)$, more experimental and theoretical work is needed.

Bibliography

[1] J. H. Christenson, J. W. Cronin, V. L. Fitch and R. Turlay, Phys. Rev. Lett. **13**, 138 (1964).

[2] M. Kobayashi and T. Maskawa, Prog. Theor. Phys. **49**, 652 (1973).

[3] M. J. Leitch *et al.* [E772 and E789 Collaboration], Nucl. Phys. A **544**, 197C (1992).

[4] D. Andrews *et al.* [CLEO Collaboration], Nucl. Instrum. Meth. **211**, 47 (1983).

[5] B. Aubert *et al.* [BABAR Collaboration], Phys. Rev. Lett. **86**, 2515 (2001) [arXiv:hep-ex/0102030].

[6] B. Aubert *et al.* [BABAR Collaboration], Phys. Rev. Lett. **90**, 242001 (2003) [arXiv:hep-ex/0304021].

[7] D. Besson *et al.* [CLEO Collaboration], Phys. Rev. D **68**, 032002 (2003) [arXiv:hep-ex/0305100].

[8] T. Barnes, F. E. Close and H. J. Lipkin, Phys. Rev. D **68**, 054006 (2003).

[9] H. Y. Cheng and W. S. Hou, Phys. Lett. B **566**, 193 (2003) [arXiv:hep-ph/0305038].

[10] A. P. Szczepaniak, Phys. Lett. B **567**, 23 (2003).

[11] T. E. Browder, S. Pakvasa and A. A. Petrov, Phys. Lett. B **578**, 365 (2004).

[12] W. A. Bardeen, E. J. Eichten and C. T. Hill, Phys. Rev. D **68**, 054024 (2003) [arXiv:hep-ph/0305049].

[13] R. N. Cahn and J. D. Jackson, Phys. Rev. D **68**, 037502 (2003) [arXiv:hep-ph/0305012].

[14] W. Lucha and F. F. Schoberl, Mod. Phys. Lett. A **18**, 2837 (2003) [arXiv:hep-ph/0309341].

[15] Y. B. Dai, C. S. Huang, C. Liu and S. L. Zhu, arXiv:hep-ph/0401142.

[16] A. Deandrea, G. Nardulli and A. D. Polosa, Phys. Rev. D **68**, 097501 (2003).

[17] "PEP-II: An Asymmetric B Factory. Conceptual Design Report. June 1993," SLAC-R-418

[18] L. Piilonen [BELLE Collaboration], Nucl. Phys. Proc. Suppl. **66**, 545 (1998).

[19] G. Buchalla, arXiv:hep-ph/0202092.

[20] B. Aubert *et al.* [BABAR Collaboration], Phys. Rev. Lett. **91**, 131801 (2003) [arXiv:hep-ex/0306052].

[21] A. Datta and P. J. O'donnell, Phys. Lett. B **572**, 164 (2003) [arXiv:hep-ph/0307106].

[22] "The *BABAR* Physics Book. October 1998," SLAC-R-504

[23] G. Buchalla, A. J. Buras and M. E. Lautenbacher, Rev. Mod. Phys. **68**, 1125 (1996) [arXiv:hep-ph/9512380].

[24] S. Eidelman *et al.* [Particle Data Group Collaboration], Phys. Lett. B **592**, 1 (2004).

[25] S. Godfrey and N. Isgur, Phys. Rev. D **32**, 189 (1985).

[26] S. Godfrey and R. Kokoski, Phys. Rev. D **43**, 1679 (1991).

[27] M. Di Pierro and E. Eichten, Phys. Rev. D **64**, 114004 (2001) [arXiv:hep-ph/0104208].

[28] P. L. Cho and M. B. Wise, Phys. Rev. D **49**, 6228 (1994) [arXiv:hep-ph/9401301].

[29] B. Aubert *et al.* [BABAR Collaboration], Phys. Rev. D **69**, 031101 (2004)

[30] K. Abe *et al.*, Phys. Rev. Lett. **92**, 012002 (2004) [arXiv:hep-ex/0307052].

[31] Y. B. Dai, C. S. Huang, C. Liu and S. L. Zhu, Phys. Rev. D **68**, 114011 (2003).

[32] P. Colangelo and F. De Fazio, Phys. Lett. B **570**, 180 (2003) [arXiv:hep-ph/0305140].

[33] E. van Beveren and G. Rupp, Phys. Rev. Lett. **91**, 012003 (2003).

[34] G. S. Bali, Phys. Rev. D **68**, 071501 (2003) [arXiv:hep-ph/0305209].

[35] B. Aubert *et al.* [BABAR Collaboration], arXiv:hep-ex/0408067.

[36] K. Terasaki, Phys. Rev. D **68**, 011501 (2003) [arXiv:hep-ph/0305213].

[37] P. Colangelo, F. De Fazio and R. Ferrandes, Mod. Phys. Lett. A **19**, 2083 (2004) [arXiv:hep-ph/0407137].

[38] A. Le Yaouanc, L. Oliver, O. Pene, J. C. Raynal and V. Morenas, Phys. Lett. B **520**, 59 (2001) [arXiv:hep-ph/0107047].

[39] P. Colangelo and F. De Fazio, Phys. Lett. B **532**, 193 (2002) [arXiv:hep-ph/0201305].

[40] P. Krokovny *et al.* [Belle Collaboration], Phys. Rev. Lett. **91**, 262002 (2003) [arXiv:hep-ex/0308019].

[41] G. Moneti [CLEO Collaboration], HEPSY 1-82 *Presented at Europhysics Study Conf:The Search for Charm, Beauty and Truth at High Energies, Erice, Italy, Nov 15-22, 1981*

[42] D. Boutigny *et al.* [BABAR Collaboration], SLAC-R-0457

[43] B. Aubert *et al.* [BABAR Collaboration], Nucl. Instrum. Meth. A **479**, 1 (2002) [arXiv:hep-ex/0105044].

[44] L. R. Dalesio *et al.*, Nucl. Instrum. Meth. A **352**, 179 (1994).

[45] V. Re *et al.*, Nucl. Instrum. Meth. A **518**, 290 (2004).

[46] The *BABAR* Collaboration, Letter of Intent for the Study of *CP* Violation and Heavy Flavor Physics at PEP-II, SLAC-443 (1994)

[47] P. Billoir, Nucl. Instrum. Meth. A **225**, 352 (1984).

[48] "Report of the Tracking Efficiency Task Force for 2001", *BABAR* Analysis Document #324, v2

[49] Scott Menary (CLEO collaboration), Measuring the Relative Slow Pion Efficiency in the Data and Monte Carlo, CBX 92-103

[50] G. Brandenburg *et al.* [CLEO Collaboration], Phys. Rev. D **58**, 052003 (1998) [arXiv:hep-ex/9802022].

[51] L. Gibbons *et al.* [CLEO Collaboration], Phys. Rev. D **56**, 3783 (1997) [arXiv:hep-ex/9703006].

[52] "Measurement of the Number of Upsilon(4S) Mesons Produced in Run 1 (B Counting)", *BABAR* Analysis Document #134, v1

[53] H. Albrecht *et al.* [ARGUS Collaboration], Phys. Lett. B **241**, 278 (1990).

[54] J. C. Anjos *et al.* [E691 Collaboration], Phys. Rev. D **48**, 56 (1993).

[55] "Tracking Efficiency Task Force in 2004" http://www.slac.stanford.edu/BFROOT/www/Physics/TrackEfficTaskForce/TrackingTaskForce-2004.html#Recipes

[56] "A Study of π^0 Efficiency", *BABAR* Analysis Document #870, v3

[57] A. Drutskoy, arXiv:hep-ex/0412070.

[58] M. Maltoni and T. Schwetz, Phys. Rev. D **68**, 033020 (2003) [arXiv:hep-ph/0304176].

[59] B. Aubert *et al.* [BABAR Collaboration], Phys. Rev. Lett. **93**, 181801 (2004) [arXiv:hep-ex/0408041].

[60] S. Godfrey, Phys. Lett. B **568**, 254 (2003) [arXiv:hep-ph/0305122].

[61] G. C. Fox and S. Wolfram, Nucl. Phys. B **149**, 413 (1979) [Erratum-ibid. B **157**, 543 (1979)].

[62] A. Drescher *et al.*, Nucl. Instrum. Meth. A **237**, 464 (1985).

Appendix A

Summary tables

A.1 Simulated data sample

Signal simulated data samples are reported in tables A.1 and A.2.

Table A.1: $B \to D_{sJ}D^{(*)}$ signal events. The twenty modes here are produced for the three D_{sJ} decays: $D^*_{sJ}(2317) \to D_s\pi^0$, $D_{sJ}(2460) \to D^*_s\pi^0$ and $D_{sJ}(2460) \to D_s\gamma$ for a total of sixty signal decay modes.

B mode	D_s mode × D mode(s)	events generated
$B^+ \to D^+_{sJ}\overline{D}^0$	$K^{*0}K^+ \times K\pi\pi\pi, K\pi, K\pi\pi^0$	180000
$B^+ \to D^+_{sJ}\overline{D}^0$	$\phi\pi^+ \times K\pi\pi\pi, K\pi, K\pi\pi^0$	180000
$B^+ \to D^+_{sJ}\overline{D}^{*0}$	$K^{*0}K^+ \times K\pi\pi\pi, K\pi, K\pi\pi^0$	180000
$B^+ \to D^+_{sJ}\overline{D}^{*0}$	$\phi\pi^+ \times K\pi\pi\pi, K\pi, K\pi\pi^0$	180000
$B^0 \to D^+_{sJ}D^-$	$\phi\pi^+, K^{*0}K^+ \times K\pi\pi$	120000
$B^0 \to D^+_{sJ}D^{*-}$	$K^{*0}K^+ \times K\pi\pi\pi, K\pi, K\pi\pi^0$	180000
$B^0 \to D^+_{sJ}D^{*-}$	$\phi\pi^+ \times K\pi\pi\pi, K\pi, K\pi\pi^0$	180000

A.2 Pre–selection summary

Pre–selection applied to D^0, $D^\pm$, D_s^+, D^{*0}, $D^{*\pm}$ and D_s^* is summarized in tables A.3- A.5.

Table A.3: D selection criteria at pre–selection level

D mode:	$D^0 \to K\pi$	$D^0 \to K\pi\pi^0$	$D^0 \to K3\pi$	$D^+ \to K\pi\pi$
π^+ tracks	GTVL	GTVL	GTVL	GTVL
K^- tracks	GTVL	GTVL	GTVL	GTVL
K^- PID	KMicroNotPion	KMicroNotPion	KMicroNotPion	KMicroNotPion
γ from π^0 mom.	-	$p(\gamma) > 30\,\mathrm{MeV}/c$	-	-
γ from π^0 LAT	-	LAT<0.8	-	-
π^0 mass window	-	$115 < m(\gamma\gamma) < 150\,\mathrm{MeV}/c^2$	-	-
D mass cut (MeV/c^2)	± 30	± 50	± 30	± 30

Table A.2: The forty two–body $B \to D_s^{(*)} D^{(*)}$ simulated decay modes. They are background events in this analysis.

B mode	D_s mode × D mode(s)	events generated
$B^+ \to D_s^+ \overline{D}^0$	$K^{*0}K^+ \times K\pi\pi\pi, K\pi, K\pi\pi^0$	173000
$B^+ \to D_s^+ \overline{D}^0$	$\phi\pi^+ \times K\pi\pi\pi, K\pi, K\pi\pi^0$	173000
$B^+ \to D_s^+ \overline{D}^{*0}$	$K^{*0}K^+ \times K\pi\pi\pi, K\pi, K\pi\pi^0$	173000
$B^+ \to D_s^+ \overline{D}^{*0}$	$\phi\pi^+ \times K\pi\pi\pi, K\pi, K\pi\pi^0$	180000
$B^+ \to D_s^{*+} \overline{D}^0$	$K^{*0}K^+ \times K\pi\pi\pi, K\pi, K\pi\pi^0$	180000
$B^+ \to D_s^{*+} \overline{D}^0$	$\phi\pi^+ \times K\pi\pi\pi, K\pi, K\pi\pi^0$	173000
$B^+ \to D_s^{*+} \overline{D}^{*0}$	$K^{*0}K^+ \times K\pi\pi\pi, K\pi, K\pi\pi^0$	177000
$B^+ \to D_s^{*+} \overline{D}^{*0}$	$\phi\pi^+ \times K\pi\pi\pi, K\pi, K\pi\pi^0$	179000
$B^0 \to D_s^+ D^-$	$\phi\pi^+, K^{*0}K^+ \times K\pi\pi$	117000
$B^0 \to D_s^+ D^{*-}$	$K^{*0}K^+ \times K\pi\pi\pi, K\pi, K\pi\pi^0$	174000
$B^0 \to D_s^+ D^{*-}$	$\phi\pi^+ \times K\pi\pi\pi, K\pi, K\pi\pi^0$	179000
$B^0 \to D_s^{*+} D^-$	$\phi\pi^+, K^{*0}K^+ \times K\pi\pi$	115000
$B^0 \to D_s^{*+} D^{*-}$	$K^{*0}K^+ \times K\pi\pi\pi, K\pi, K\pi\pi^0$	171000
$B^0 \to D_s^{*+} D^{*-}$	$\phi\pi^+ \times K\pi\pi\pi, K\pi, K\pi\pi^0$	171000

Table A.4: D_s selection criteria at pre–selection level

D_s mode:	$D_s^+ \to \phi\pi^+$	$D_s^+ \to K^{*0}K^+$
π^+ tracks	GTVL	GTVL
K^+ tracks	GTVL	GTVL
K^- tracks	GTVL	GTVL
K^- PID	KMicroNotPion	KMicroNotPion
K^+ PID	KMicroNotPion	KMicroNotPion
ϕ or K^{*0} mass cut	(1005 < m < 1030) MeV/c^2	(821 < m < 971) MeV/c^2
D_s mass cut (MeV/c^2)	± 30	± 30

A.3 Optimization summary

In Tables A.6- A.7 are summarized the invariant mass resolutions for D^{*+} and D_s^{*+}, and in Tables A.8- A.10 the selection after the optimization procedure.

The effect on the invariant mass distributions of the vertexing requirement $prob(\chi^2) > 10^{-3}$ for $D^0 \to K^- \pi^+ \pi^- \pi^+$ and $D^+ \to K^- \pi^+ \pi^+$ is shown in Figure A.1.

The optimization of the selection based on the $D^+\gamma$, $D^{(*)}\pi^0$ invariant mass values is shown in Figure A.2.

Table A.5: $D^{*(0)}_{(s)}$ selection criteria at pre–selection level

$D^{*(0)}_{(s)}$ mode:	$D^{*+} \to D^0\pi^+$	$D^{*0} \to D^0\pi^0$	$D^{*0} \to D^0\gamma$	$D_s^{*+} \to D_s^+\gamma$
π_s^+ track	GTVL	-	-	-
γ/π_s momentum cut (MeV/c)	$p^*(\pi^+) < 450$	$p^*(\pi^0) < 450$	$p(\gamma) > 100$	$p(\gamma) > 100$
π^0 veto on γ from $D^*_{(s)}$	-	-	yes	yes
LAT cut (γ from $D^*_{(s)}$)	-	-	LAT<0.8	LAT<0.8
Δm cut (MeV/c^2)	± 4.1	[138,146]	[112,172]	[114,174]
$D^0 \to K^- \pi^+ \pi^0$	± 5.1	-	-	-

Table A.6: D^0, D^+ and D_s^+ masses and resolutions (MeV/c^2) in data, simulation and nominal [24], from the fit of a single gaussian to the reconstructed mass spectra. In the last column the optimized mass cut in terms of number of standard deviations n_σ.

decay	m (data) MeV/c^2	σ (data) MeV/c^2	m (sim) MeV/c^2	σ (sim) MeV/c^2	m [24] MeV/c^2	n_σ cut
$D^0 \to K^- \pi^+$	1863.1±0.1	6.3±0.1	1863.7±0.1	6.3±0.1	1864.5	3.0
$D^0 \to K^- \pi^+ \pi^0$	1861.8±0.5	11.8±0.8	1862.4±0.2	9.4±0.3	1864.5	2.5
$D^0 \to K^- \pi^+ \pi^- \pi^+$	1862.6±0.3	5.4±0.3	1863.7±0.1	4.9±0.1	1864.5	2.5
$D^+ \to K^- \pi^+ \pi^+$	1867.8±0.2	5.3±0.2	1868.7±0.1	5.1±0.1	1869.3	3.0
$D_s^+ \to \phi\pi^+$	1966.1±0.1	5.3±0.1	1967.1±0.1	5.1±0.1	1968.5	3.0
$D_s^+ \to \bar{K}^{*0} K^+$	1965.6±0.1	5.9±0.1	1966.6±0.1	5.5±0.1	1968.5	2.5

Table A.7: $D^* - D$ mass differences and resolutions in the data and in simulation, from the fit of a single gaussian to the reconstructed mass spectra.

Decay	Δm (data) MeV/c^2	$\sigma_{\Delta m}(data)$ MeV/c^2	Δm(sim) MeV/c^2	$\sigma\Delta m$ (sim) MeV/c^2	Δm [24] MeV/c^2
$D^{*0} \to D^0 \pi^0$	141.99±0.05	1.00±0.06	142.11±0.01	0.82±0.02	142.12
$D^{*0} \to D^0 \gamma$	143.19±0.61	4.36±0.72	142.33±0.17	4.42±0.20	142.12
$D^{*+} \to D^0 \pi^+$	145.45±0.01	0.40±0.01	145.40±0.01	0.42±0.01	145.42
$D_s^* \to D_s^+ \gamma$	146.33±0.21	4.25±0.25	144.25±0.07	4.78±0.09	143.8

A.4 Efficiency and cross–feed tables

Tables A.11- A.13 summarize the efficiency and the cross–feed extracted from simulation.

Table A.8: Final D selection criteria.

D mode:	$D^0 \to K^- \pi^+$	$D^0 \to K^- \pi^+ \pi^0$	$D^0 \to K^- \pi^+ \pi^- \pi^+$	$D^+ \to K^- \pi^+ \pi^+$
π^+ tracks	GTVL	GTVL	GTVL	GTVL
K^- tracks	GTVL	GTVL	GTVL	GTVL
K^- PID	KMicroNotPion	KMicroTight (KMicroNotPion)	KMicroTight (KMicroNotPion)	KMicroNotPion
γ from π^0 mom.	-	$p(\gamma) > 30\,\mathrm{MeV}/c$	-	-
γ from π^0 LAT	-	LAT<0.8	-	-
π^0 energy	-	$E(\pi^0) > 200\,\mathrm{MeV}/c$	-	-
D mass window	3σ	2.5σ	2.5σ	3σ
Dalitz weight	-	> 10	-	-
vertex χ^2 prob.	none	none	$> 10^{-3}$	none

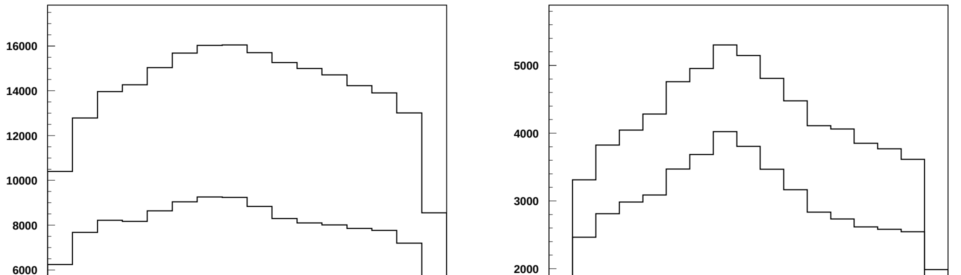

Figure A.1: Effect of the vertex requirement prob(χ^2) $> 10^{-3}$ on the invariant mass distributions for $D^0 \to K^- \pi^+ \pi^- \pi^+$ (left) and $D^+ \to K^- \pi^+ \pi^+$ (right) candidates.

*Table A.9: Final D_s selection criteria. When different, the cuts for D_s from decays with a $\bar{D}^0 \to K^+\pi^-$ are indicated by a * and the cuts for D_s from decays with a $D^- \to K^+\pi^-\pi^-$ are indicated by a **.*

D_s mode:	$D_s^+ \to \phi\pi^+$	$D_s^+ \to K^{*0}K^+$
π^+ tracks	GTVL	GTVL
$K^\pm$ tracks	GTVL	GTVL
$K^\pm$ PID	≥1 KTight 2 KMicroNotPion (*,**)	≥1 KTight
ϕ or K^{*0} mass cut	$m_{PDG} \pm 15\,\mathrm{MeV}/c^2$	$m_{PDG} \pm 75\,\mathrm{MeV}/c^2$
helicity cut	$\lvert cos(\theta_h)\rvert > 0.3$ none if D^{*-} with $\bar{D}^0 \to K^+\ \pi^-$	$\lvert cos(\theta_h)\rvert > 0.3$
vertex χ^2 prob.		$> 10^{-3}$ none(*)
D_s mass window	$3\ \sigma$	$2.5\ \sigma$

Table A.10: Final D^* selection criteria

D^* mode:	$D^{*+} \to D^0\ \pi^+$	$D^{*0} \to D^0\ \pi^0$	$D^{*0} \to D^0\ \gamma$	$D_s^* \to D_s^+\ \gamma$
π^+_{soft} track	GTVL	-	-	-
γ/π_{soft} momentum cut (MeV/c)	$p^*(\pi^+) < 450$	$p^*(\pi^0) < 450$	$p(\gamma) > 100$	$p(\gamma) > 100$
π^0 veto on γ from D^*	-	-	yes	yes
LAT cut (γ from D^*)	-	-	LAT<0.8	LAT<0.8
Δm cut(MeV/c^2)	[143.4, 145.4]	[140.0, 144.0]	[132.0, 152.0]	[133.8, 153.8]

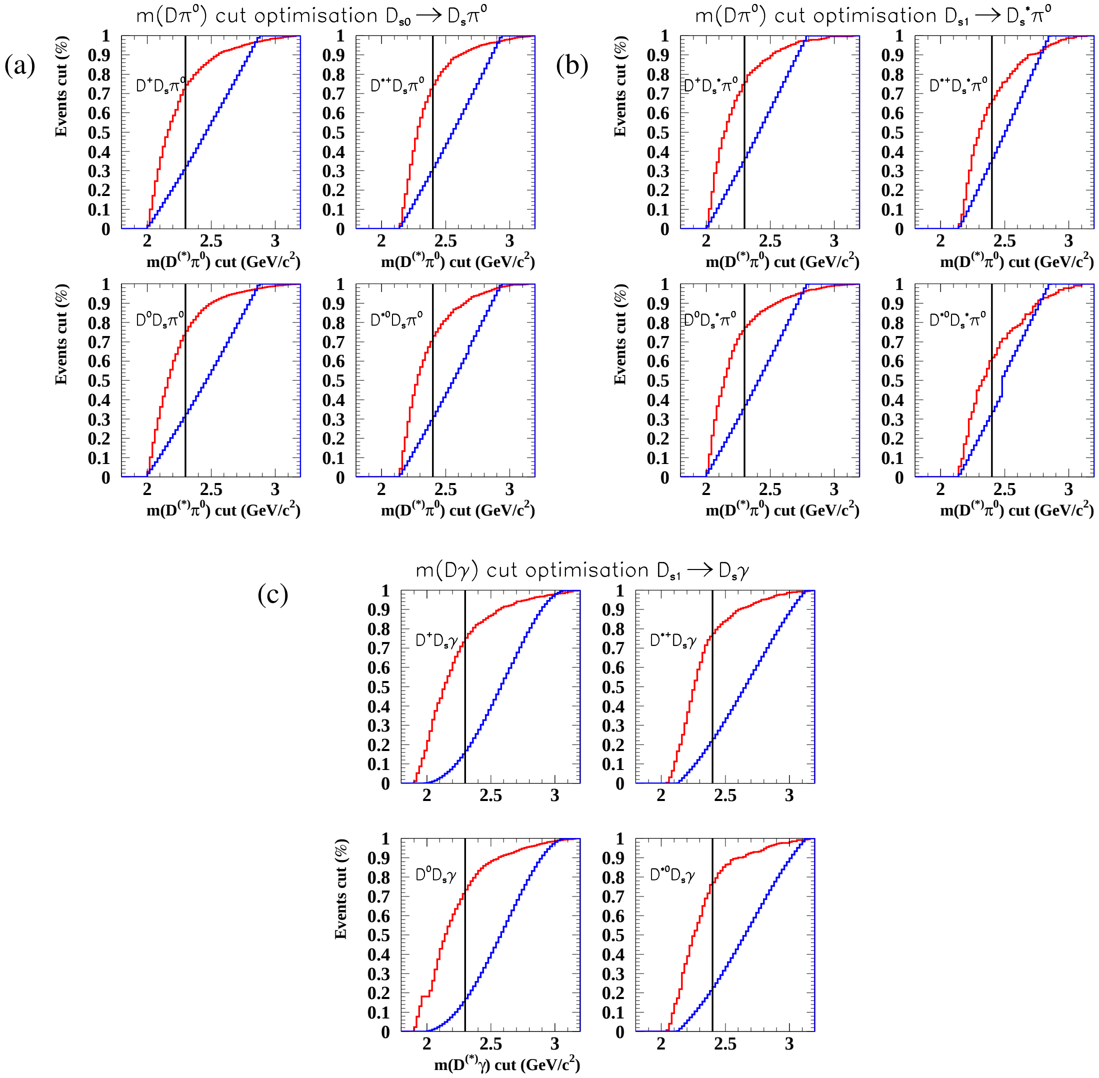

Figure A.2: Fraction of discarded events as a function of the value of the cut on the $D^{(*)}\gamma$ *or* $D^{(*)}\pi^0$ *masses both for the signal (blue) and for the background (red) (a)* $B \to D_{s0}^{+}\overline{D}^{(*)}$, $D_{s0}^{+} \to D_s\pi^0$ *decays; (b)* $B \to D_{s1}^{+}\overline{D}^{(*)}$, $D_{s1}^{*+} \to D_s\pi^0$ *decays;(c)* $B \to D_{s1}^{+}\overline{D}^{(*)}$, $D_{s1}^{*+} \to D_s\gamma$ *decays; the solid lines indicate the final value of the cuts used in this analysis.*

Table A.11: Efficiency and cross–feed matrix for the modes $B \to D_{s0}^{+}\overline{D}^{(*)}$, $D_{s0}^{+} \to D_s\pi^0$ *(final states* $\overline{D}^{(*)}D_s\pi^0$*).*

generated B mode	reconstructed final state	reconstructed mass (MeV/c^2)	fitted width (MeV/c^2)	$\varepsilon_{i,j}$ (%) $= Nreco/Ngen.$
$D_{s0}^{+}D^{-}$ $(\phi\pi \times K\pi\pi)$	$D_s^{+}D^{-}\pi^0$ $(\phi\pi \times K\pi\pi)$	2314.4	7.4±0.1	5.11±0.1
$D_{s0}^{+}D^{0}$ $(\phi\pi \times K\pi\pi^0)$		2315.0	8.0±0	0.05±0.01
$D_{s0}^{+}D^{-}$ $(K^{*0}K \times K\pi\pi)$	$D_s^{+}D^{-}\pi^0$ $(K^{*0}K \times K\pi\pi)$	2314.2	7.1±0.1	3.99±0.08
$D_{s0}^{+}D^{*-}$ $(\phi\pi \times K\pi)$	$D_s^{+}D^{*-}\pi^0$ $(\phi\pi \times K\pi)$	2314.6	7.6±0.1	4.16±0.09
$D_{s0}^{+}D^{*-}$ $(\phi\pi \times K\pi\pi^0)$	$D_s^{+}D^{*-}\pi^0$ $(\phi\pi \times K\pi\pi^0)$	2314.9	7.5±0.2	1.71±0.06
$D_{s0}^{+}D^{*-}$ $(\phi\pi \times K3\pi)$	$D_s^{+}D^{*-}\pi^0$ $(\phi\pi \times K3\pi)$	2314.7	7.3±0.2	2.11±0.06
$D_{s0}^{+}D^{*-}$ $(K^{*0}K \times K\pi)$	$D_s^{+}D^{*-}\pi^0$ $(K^{*0}K \times K\pi)$	2314.2	7.5±0.1	3.57±0.08
$D_{s0}^{+}D^{*-}$ $(K^{*0}K \times K\pi\pi^0)$	$D_s^{+}D^{*-}\pi^0$ $(K^{*0}K \times K\pi\pi^0)$	2314.3	7.9±0.3	1.36±0.05
$D_{s0}^{+}D^{*-}$ $(K^{*0}K \times K3\pi)$	$D_s^{+}D^{*-}\pi^0$ $(K^{*0}K \times K3\pi)$	2314.5	7.2±0.2	1.6±0.05
$D_{s0}^{+}D^{0}$ $(\phi\pi \times K\pi)$	$D_s^{+}D^{0}\pi^0$ $(\phi\pi \times K\pi)$	2314.5	7.7±0.1	6.57±0.11
$D_{s0}^{+}D^{0}$ $(\phi\pi \times K\pi\pi^0)$	$D_s^{+}D^{0}\pi^0$ $(\phi\pi \times K\pi\pi^0)$	2315.0	7.9±0.2	1.93±0.06
$D_{s0}^{+}D^{-}$ $(\phi\pi \times K\pi\pi)$		2315.0	8.0±0	0.04±0.01
$D_{s0}^{+}D^{0}$ $(\phi\pi \times K3\pi)$	$D_s^{+}D^{0}\pi^0$ $(\phi\pi \times K3\pi)$	2314.5	7.1±0.2	2.55±0.07
$D_{s0}^{+}D^{0}$ $(K^{*0}K \times K\pi)$	$D_s^{+}D^{0}\pi^0$ $(K^{*0}K \times K\pi)$	2314.0	7.5±0.1	5.81±0.1
$D_{s0}^{+}D^{0}$ $(K^{*0}K \times K\pi\pi^0)$	$D_s^{+}D^{0}\pi^0$ $(K^{*0}K \times K\pi\pi^0)$	2314.4	7.7±0.2	1.68±0.05
$D_{s0}^{+}D^{-}$ $(K^{*0}K \times K\pi\pi)$		2315.0	8.0±0	0.03±0.01
$D_{s0}^{+}D^{0}$ $(K^{*0}K \times K3\pi)$	$D_s^{+}D^{0}\pi^0$ $(K^{*0}K \times K3\pi)$	2314.2	7.2±0.2	2.18±0.06
$D_{s0}^{+}D^{*0}$ $(\phi\pi \times K\pi)$	$D_s^{+}D^{*0}\pi^0$ $(\phi\pi \times K\pi)$	2315.0	7.3±0.2	2.73±0.07
$D_{s0}^{+}D^{*-}$ $(\phi\pi \times K\pi)$		2315.0	8.0±0	0.43±0.03
$D_{s1}^{+}D^{0}$ $(\phi\pi \times K\pi)$		2311.0	18.0±0	0.42±0.03
$D_{s0}^{+}D^{*0}$ $(\phi\pi \times K\pi\pi^0)$	$D_s^{+}D^{*0}\pi^0$ $(\phi\pi \times K\pi\pi^0)$	2315.2	7.7±0.4	0.76±0.04
$D_{s0}^{+}D^{*-}$ $(\phi\pi \times K\pi\pi^0)$		2315.0	8.0±0	0.13±0.02
$D_{s1}^{+}D^{0}$ $(\phi\pi \times K\pi\pi^0)$		2311.0	18.0±0	0.14±0.02
$D_{s0}^{+}D^{*0}$ $(\phi\pi \times K3\pi)$	$D_s^{+}D^{*0}\pi^0$ $(\phi\pi \times K3\pi)$	2315.0	8.1±0.3	1.05±0.04
$D_{s0}^{+}D^{*-}$ $(\phi\pi \times K3\pi)$		2315.0	8.0±0	0.14±0.02
$D_{s1}^{+}D^{0}$ $(\phi\pi \times K3\pi)$		2311.0	18.0±0	0.15±0.02
$D_{s0}^{+}D^{*0}$ $(K^{*0}K \times K\pi)$	$D_s^{+}D^{*0}\pi^0$ $(K^{*0}K \times K\pi)$	2314.3	7.8±0.2	2.13±0.06
$D_{s0}^{+}D^{*-}$ $(K^{*0}K \times K\pi)$		2315.0	8.0±0	0.33±0.02
$D_{s1}^{+}D^{0}$ $(K^{*0}K \times K\pi)$		2311.0	18.0±0	0.34±0.03
$D_{s0}^{+}D^{*0}$ $(K^{*0}K \times K\pi\pi^0)$	$D_s^{+}D^{*0}\pi^0$ $(K^{*0}K \times K\pi\pi^0)$	2314.5	7.5±0.4	0.61±0.03
$D_{s0}^{+}D^{*-}$ $(K^{*0}K \times K\pi\pi^0)$		2315.0	8.0±0	0.09±0.01
$D_{s1}^{+}D^{0}$ $(K^{*0}K \times K\pi\pi^0)$		2311.0	18.0±0	0.1±0.01
$D_{s0}^{+}D^{*0}$ $(K^{*0}K \times K3\pi)$	$D_s^{+}D^{*0}\pi^0$ $(K^{*0}K \times K3\pi)$	2314.5	7.1±0.3	0.86±0.04
$D_{s0}^{+}D^{*-}$ $(K^{*0}K \times K3\pi)$		2315.0	8.0±0	0.14±0.02
$D_{s1}^{+}D^{0}$ $(K^{*0}K \times K3\pi)$		2311.0	18.0±0	0.13±0.02

Table A.12: Efficiency and cross–feed matrix for the modes $B \to D_{s1}^{+}\overline{D}^{(*)}$, $D_{s1}^{+} \to D_{s}^{*+}\pi^{0}$ *(final states* $\overline{D}^{(*)}D_{s}^{*+}\pi^{0}$*).*

generated B mode	reconstructed final state	reconstructed mass (MeV/c^2)	fitted width (MeV/c^2)	$\varepsilon_{i,j}$ (%) $= Nreco/Ngen.$
$D_{s1}^{+}D^{-}$ $(\phi\pi \times K\pi\pi)$	$D_{s}^{*+}D^{-}\pi^{0}$ $(\phi\pi \times K\pi\pi)$	2455.6	7.9±0.3	1.64±0.06
$D_{s1}^{+}D^{0}$ $(\phi\pi \times K\pi\pi^{0})$		2456.0	8.0±0	0.02±0.01
$D_{s1}^{+}D^{-}$ $(K^{*0}K \times K\pi\pi)$	$D_{s}^{*+}D^{-}\pi^{0}$ $(K^{*0}K \times K\pi\pi)$	2455.7	7.3±0.3	1.28±0.05
$D_{s1}^{+}D^{*-}$ $(\phi\pi \times K\pi)$	$D_{s}^{*+}D^{*-}\pi^{0}$ $(\phi\pi \times K\pi)$	2456.1	7.9±0.3	1.33±0.05
$D_{s1}^{+}D^{*-}$ $(\phi\pi \times K\pi\pi^{0})$	$D_{s}^{*+}D^{*-}\pi^{0}$ $(\phi\pi \times K\pi\pi^{0})$	2454.9	7.9±0.5	0.47±0.03
$D_{s1}^{+}D^{*-}$ $(\phi\pi \times K3\pi)$	$D_{s}^{*+}D^{*-}\pi^{0}$ $(\phi\pi \times K3\pi)$	2455.4	9.2±0.5	0.62±0.03
$D_{s1}^{+}D^{*-}$ $(K^{*0}K \times K\pi)$	$D_{s}^{*+}D^{*-}\pi^{0}$ $(K^{*0}K \times K\pi)$	2455.5	8.0±0.3	1.15±0.05
$D_{s1}^{+}D^{*-}$ $(K^{*0}K \times K\pi\pi^{0})$	$D_{s}^{*+}D^{*-}\pi^{0}$ $(K^{*0}K \times K\pi\pi^{0})$	2455.8	8.8±0.7	0.43±0.03
$D_{s1}^{+}D^{*-}$ $(K^{*0}K \times K3\pi)$	$D_{s}^{*+}D^{*-}\pi^{0}$ $(K^{*0}K \times K3\pi)$	2455.8	7.2±0.4	0.51±0.03
$D_{s1}^{+}D^{0}$ $(\phi\pi \times K\pi)$	$D_{s}^{*+}D^{0}\pi^{0}$ $(\phi\pi \times K\pi)$	2456.1	8.2±0.2	2.25±0.07
$D_{s0}^{+}D^{*-}$ $(\phi\pi \times K\pi)$		2464.0	20.0±0	0.24±0.02
$D_{s0}^{+}D^{*0}$ $(\phi\pi \times K\pi)$		2464.0	20.0±0	0.27±0.02
$D_{s1}^{+}D^{0}$ $(\phi\pi \times K\pi\pi^{0})$	$D_{s}^{*+}D^{0}\pi^{0}$ $(\phi\pi \times K\pi\pi^{0})$	2457.0	8.4±0.5	0.56±0.03
$D_{s0}^{+}D^{*-}$ $(\phi\pi \times K\pi\pi^{0})$		2464.0	20.0±0	0.06±0.01
$D_{s0}^{+}D^{*0}$ $(\phi\pi \times K\pi\pi^{0})$		2464.0	20.0±0	0.1±0.01
$D_{s1}^{+}D^{0}$ $(\phi\pi \times K3\pi)$	$D_{s}^{*+}D^{0}\pi^{0}$ $(\phi\pi \times K3\pi)$	2455.6	7.5±0.3	0.79±0.04
$D_{s0}^{+}D^{*-}$ $(\phi\pi \times K3\pi)$		2464.0	20.0±0	0.09±0.01
$D_{s0}^{+}D^{*0}$ $(\phi\pi \times K3\pi)$		2464.0	20.0±0	0.12±0.02
$D_{s1}^{+}D^{0}$ $(K^{*0}K \times K\pi)$	$D_{s}^{*+}D^{0}\pi^{0}$ $(K^{*0}K \times K\pi)$	2455.2	8.0±0.2	1.94±0.06
$D_{s0}^{+}D^{*-}$ $(K^{*0}K \times K\pi)$		2464.0	20.0±0	0.19±0.02
$D_{s0}^{+}D^{*0}$ $(K^{*0}K \times K\pi)$		2464.0	20.0±0	0.23±0.02
$D_{s1}^{+}D^{0}$ $(K^{*0}K \times K\pi\pi^{0})$	$D_{s}^{*+}D^{0}\pi^{0}$ $(K^{*0}K \times K\pi\pi^{0})$	2456.6	7.1±0.4	0.52±0.03
$D_{s0}^{+}D^{*-}$ $(K^{*0}K \times K\pi\pi^{0})$		2464.0	20.0±0	0.06±0.01
$D_{s0}^{+}D^{*0}$ $(K^{*0}K \times K\pi\pi^{0})$		2464.0	20.0±0	0.05±0.01
$D_{s1}^{+}D^{0}$ $(K^{*0}K \times K3\pi)$	$D_{s}^{*+}D^{0}\pi^{0}$ $(K^{*0}K \times K3\pi)$	2455.4	7.1±0.3	0.67±0.03
$D_{s0}^{+}D^{*-}$ $(K^{*0}K \times K3\pi)$		2464.0	20.0±0	0.07±0.01
$D_{s0}^{+}D^{*0}$ $(K^{*0}K \times K3\pi)$		2464.0	20.0±0	0.1±0.01
$D_{s1}^{+}D^{*0}$ $(\phi\pi \times K\pi)$	$D_{s}^{*+}D^{*0}\pi^{0}$ $(\phi\pi \times K\pi)$	2455.7	9.3±0.5	0.84±0.04
$D_{s1}^{+}D^{*-}$ $(\phi\pi \times K\pi)$		2456.0	8.0±0	0.13±0.02
$D_{s1}^{+}D^{*0}$ $(\phi\pi \times K\pi\pi^{0})$	$D_{s}^{*+}D^{*0}\pi^{0}$ $(\phi\pi \times K\pi\pi^{0})$	2455.6	8.6±0.6	0.26±0.02
$D_{s1}^{+}D^{*-}$ $(\phi\pi \times K\pi\pi^{0})$		2456.0	8.0±0	0.05±0.01
$D_{s1}^{+}D^{*0}$ $(\phi\pi \times K3\pi)$	$D_{s}^{*+}D^{*0}\pi^{0}$ $(\phi\pi \times K3\pi)$	2456.7	7.8±0.6	0.32±0.02
$D_{s1}^{+}D^{*-}$ $(\phi\pi \times K3\pi)$		2456.0	8.0±0	0.05±0.01
$D_{s1}^{+}D^{*0}$ $(K^{*0}K \times K\pi)$	$D_{s}^{*+}D^{*0}\pi^{0}$ $(K^{*0}K \times K\pi)$	2455.7	7.4±0.4	0.76±0.04
$D_{s1}^{+}D^{*-}$ $(K^{*0}K \times K\pi)$		2456.0	8.0±0	0.13±0.02
$D_{s1}^{+}D^{*0}$ $(K^{*0}K \times K\pi\pi^{0})$	$D_{s}^{*+}D^{*0}\pi^{0}$ $(K^{*0}K \times K\pi\pi^{0})$	2455.6	7.1±0.7	0.19±0.02
$D_{s1}^{+}D^{*-}$ $(K^{*0}K \times K\pi\pi^{0})$		2456.0	8.0±0	0.03±0.01
$D_{s1}^{+}D^{*0}$ $(K^{*0}K \times K3\pi)$	$D_{s}^{*+}D^{*0}\pi^{0}$ $(K^{*0}K \times K3\pi)$	2455.7	7.6±0.8	0.17±0.02
$D_{s1}^{+}D^{*-}$ $(K^{*0}K \times K3\pi)$		2456.0	8.0±0	0.05±0.01

Table A.13: Efficiency and cross–feed matrix for the modes $B \to D_{s1}^{+}\overline{D}^{(*)}$, $D_{s1}^{+} \to D_s^{+}\gamma$ *(final states* $\overline{D}^{(*)}D_s^{+}\gamma$*).*

generated B mode	reconstructed final state	reconstructed mass (MeV/c^2)	fitted width (MeV/c^2)	$\varepsilon_{i,j}$ (%) $= Nreco/Ngen.$
$D_{s1}^{+}D^{-}$ ($\phi\pi \times K\pi\pi$)	$D_s^{+}D^{-}\gamma$ ($\phi\pi \times K\pi\pi$)	2455.5	12.6±0.1	8.58±0.12
$D_{s1}^{+}D^{0}$ ($\phi\pi \times K\pi\pi^0$)		2456.0	12.6±0	0.08±0.01
$D_{s1}^{+}D^{-}$ ($K^{*0}K \times K\pi\pi$)	$D_s^{+}D^{-}\gamma$ ($K^{*0}K \times K\pi\pi$)	2455.3	12.6±0.2	6.63±0.1
$D_{s1}^{+}D^{0}$ ($K^{*0}K \times K\pi\pi^0$)		2456.0	12.6±0	0.06±0.01
$D_{s1}^{+}D^{*-}$ ($\phi\pi \times K\pi$)	$D_s^{+}D^{*-}\gamma$ ($\phi\pi \times K\pi$)	2455.5	12.6±0.2	6.13±0.1
$D_{s1}^{+}D^{*-}$ ($\phi\pi \times K\pi\pi^0$)	$D_s^{+}D^{*-}\gamma$ ($\phi\pi \times K\pi\pi^0$)	2455.6	12.6±0.2	2.62±0.07
$D_{s1}^{+}D^{*-}$ ($\phi\pi \times K3\pi$)	$D_s^{+}D^{*-}\gamma$ ($\phi\pi \times K3\pi$)	2455.7	12.5±0.2	3.11±0.07
$D_{s1}^{+}D^{*-}$ ($K^{*0}K \times K\pi$)	$D_s^{+}D^{*-}\gamma$ ($K^{*0}K \times K\pi$)	2455.2	12.7±0.2	5.05±0.09
$D_{s1}^{+}D^{*-}$ ($K^{*0}K \times K\pi\pi^0$)	$D_s^{+}D^{*-}\gamma$ ($K^{*0}K \times K\pi\pi^0$)	2455.0	13.0±0.3	2.03±0.06
$D_{s1}^{+}D^{*-}$ ($K^{*0}K \times K3\pi$)	$D_s^{+}D^{*-}\gamma$ ($K^{*0}K \times K3\pi$)	2454.9	12.8±0.2	2.48±0.06
$D_{s1}^{+}D^{0}$ ($\phi\pi \times K\pi$)	$D_s^{+}D^{0}\gamma$ ($\phi\pi \times K\pi$)	2455.0	12.8±0.1	11.29±0.14
$D_{s1}^{+}D^{0}$ ($\phi\pi \times K\pi\pi^0$)	$D_s^{+}D^{0}\gamma$ ($\phi\pi \times K\pi\pi^0$)	2455.0	12.4±0.2	3.19±0.07
$D_{s1}^{+}D^{-}$ ($\phi\pi \times K\pi\pi$)		2456.0	12.6±0	0.1±0.01
$D_{s1}^{+}D^{*-}$ ($\phi\pi \times K\pi\pi^0$)		2456.0	12.6±0	0.03±0.01
$D_{s1}^{+}D^{*0}$ ($\phi\pi \times K\pi\pi^0$)		2456.0	12.6±0	0.06±0.01
$D_{s1}^{+}D^{0}$ ($\phi\pi \times K3\pi$)	$D_s^{+}D^{0}\gamma$ ($\phi\pi \times K3\pi$)	2455.4	12.6±0.2	4.13±0.08
$D_{s1}^{+}D^{*-}$ ($\phi\pi \times K3\pi$)		2456.0	12.6±0	0.04±0.01
$D_{s1}^{+}D^{*0}$ ($\phi\pi \times K3\pi$)		2456.0	12.6±0	0.04±0.01
$D_{s1}^{+}D^{0}$ ($K^{*0}K \times K\pi$)	$D_s^{+}D^{0}\gamma$ ($K^{*0}K \times K\pi$)	2454.9	12.6±0.1	9.65±0.13
$D_{s1}^{+}D^{0}$ ($K^{*0}K \times K\pi\pi^0$)	$D_s^{+}D^{0}\gamma$ ($K^{*0}K \times K\pi\pi^0$)	2455.3	12.2±0.2	2.5±0.06
$D_{s1}^{+}D^{-}$ ($K^{*0}K \times K\pi\pi$)		2456.0	12.6±0	0.08±0.01
$D_{s1}^{+}D^{*-}$ ($K^{*0}K \times K\pi\pi^0$)		2456.0	12.6±0	0.04±0.01
$D_{s1}^{+}D^{*0}$ ($K^{*0}K \times K\pi\pi^0$)		2456.0	12.6±0	0.04±0.01
$D_{s1}^{+}D^{0}$ ($K^{*0}K \times K3\pi$)	$D_s^{+}D^{0}\gamma$ ($K^{*0}K \times K3\pi$)	2456.0	12.3±0.2	3.37±0.07
$D_{s1}^{+}D^{*0}$ ($\phi\pi \times K\pi$)	$D_s^{+}D^{*0}\gamma$ ($\phi\pi \times K\pi$)	2455.1	12.9±0.2	4.63±0.08
$D_{s1}^{+}D^{*-}$ ($\phi\pi \times K\pi$)		2456.0	12.6±0	0.82±0.04
$D_{s1}^{+}D^{*0}$ ($\phi\pi \times K\pi\pi^0$)	$D_s^{+}D^{*0}\gamma$ ($\phi\pi \times K\pi\pi^0$)	2456.1	12.4±0.4	1.32±0.05
$D_{s1}^{+}D^{*-}$ ($\phi\pi \times K\pi\pi^0$)		2456.0	12.6±0	0.27±0.02
$D_{s1}^{+}D^{0}$ ($\phi\pi \times K\pi\pi^0$)		2456.0	12.6±0	0.04±0.01
$D_{s1}^{+}D^{*0}$ ($\phi\pi \times K3\pi$)	$D_s^{+}D^{*0}\gamma$ ($\phi\pi \times K3\pi$)	2455.3	13.1±0.3	1.66±0.05
$D_{s1}^{+}D^{*-}$ ($\phi\pi \times K3\pi$)		2456.0	12.6±0	0.32±0.02
$D_{s1}^{+}D^{*0}$ ($K^{*0}K \times K\pi$)	$D_s^{+}D^{*0}\gamma$ ($K^{*0}K \times K\pi$)	2454.5	13.3±0.2	3.98±0.08
$D_{s1}^{+}D^{*-}$ ($K^{*0}K \times K\pi$)		2456.0	12.6±0	0.8±0.04
$D_{s1}^{+}D^{*0}$ ($K^{*0}K \times K\pi\pi^0$)	$D_s^{+}D^{*0}\gamma$ ($K^{*0}K \times K\pi\pi^0$)	2455.6	13.2±0.4	1.04±0.04
$D_{s1}^{+}D^{*-}$ ($K^{*0}K \times K\pi\pi^0$)		2456.0	12.6±0	0.23±0.02
$D_{s1}^{+}D^{0}$ ($K^{*0}K \times K\pi\pi^0$)		2456.0	12.6±0	0.03±0.01
$D_{s1}^{+}D^{*0}$ ($K^{*0}K \times K3\pi$)	$D_s^{+}D^{*0}\gamma$ ($K^{*0}K \times K3\pi$)	2455.8	12.6±0.4	1.31±0.05
$D_{s1}^{+}D^{*-}$ ($K^{*0}K \times K3\pi$)		2456.0	12.6±0	0.28±0.02
$D_{s1}^{+}D^{0}$ ($K^{*0}K \times K3\pi$)		2456.0	12.6±0	0.02±0.01

Appendix B

Definitions

B.1 Fox-Wolfram moments

The Fox-Wolfram moments [61], H_l, are extensively used to characterize the event topology. The l-order Fox-Wolfram moment can be written as:

$$H_l \equiv \sum_{i,j} \frac{|p_i||p_j|}{E_{vis}^2} P_l(cos\Theta_{ij}) \tag{B.1}$$

where $p_{i,j}$ are the (charged and neutral) particle momenta, Θ_{ij} is the opening angle between particles i and j and E_{vis} the total visible energy of the event. The functions $P_l(cos\Theta)$, with $l = 0, 1, 2, \ldots$, are the Legendre Polynomials. In particular,

$$P_0(cos\Theta) = 1, P_1(cos\Theta) = cos\Theta, P_2(cos\Theta) = \frac{1}{2}(3cos^2\Theta - 1) \tag{B.2}$$

For jet-like events $|cos\Theta_i, j|$ is peaked at 1, while for spherical $B\bar{B}$ events $|cos\Theta_i, j|$ is more uniformly distributed, thus the normalized second Fox-Wolfram moment, $R_2 = \frac{H_2}{H_0}$, is shifted towards one in Bhabha, dimuons and $q\bar{q}$ events and towards zero in $B\bar{B}$ events.

B.2 Lateral energy distribution

To describe the lateral energy distribution of the showers in the calorimeter, one can define the variable [62]

$$LAT = \frac{\sum\limits_{i=3}^{N} E_i r_i^2}{\sum_{i=3}^{N} E_i r_i^2 + E_1 r_0^2 + E_2 r_0^2} \tag{B.3}$$

where N is the number of crystals associated with the shower, $E_1 > E_2 > ... > E_N$ are the energies deposited in the i-th crystal, $r_0 = 5$ cm is the average distance between two crystals and r_i is the distance between the crystal i and the center of the shower (see fig. B.1).

This variable is constructed to discriminate between electromagnetic and hadronic showers based on their average properties. The summation in the numerator omits the two crystals containing the highest amounts of energy. Electrons deposit most of their energy in two or three crystals, so that the value of LAT is small for electromagnetic showers.

Multiplying the energies by the squared distances enhances the effects for the hadronic showers, compared with electronic.

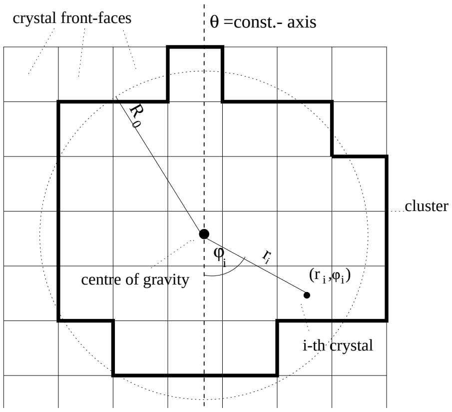

Figure B.1: Definition of r_i, ϕ_i and R_0.